SAMUEL NTIM

BEHAVIOUR OF ROOM TEMPERATURE IONIC LIQUIDS AT GOLD INTERFACES: FROM EQUILIBRIUM TO NON-EQUILIBRIUM AND ELECTRIFIED CONDITIONS

BEHAVIOUR OF ROOM TEMPERATURE IONIC LIQUIDS AT GOLD INTERFACES: FROM EQUILIBRIUM TO NON-EQUILIBRIUM AND ELECTRIFIED CONDITIONS

SAMUEL NTIM

Dissertation zur Erlangung des Grades
„Doktor der Naturwissenschaften"
am Fachbereich Physik, Mathematik und Informatik
der Johannes Gutenberg-Universität in Mainz

vorgelegt von Samuel Ntim, geboren in Accra
Mainz, November 2025

SAMUEL NTIM: *Behaviour of room temperature ionic liquids at gold interfaces: From equilibrium to non-equilibrium and electrified conditions*

SUPERVISOR:
Prof. Dr. Marialore Sulpizi

LOCATION:
KOMET 331, Johannes-Gutenberg-Universität, Mainz

ORAL EXAMINATION:
04. Feb. 2026

Dedicated to Yaa Boatemaa, Egya-Mbea, Enyimnyam and Nyametsease, and to Egya Kweku Mbiah and Eno Ekuwa Abaenuwa

ABSTRACT

This thesis investigates the behaviour of room temperature ionic liquids (RTILs), specifically 1-butyl-3-methylimidazolium tetrafluoroborate ([BMIM][BF_4]), at gold interfaces under varying conditions, including equilibrium, shear flow, and electrified interfaces. The study is motivated by the increasing relevance of RTILs in advanced applications such as energy storage, catalysis, and lubrication, where understanding the molecular interactions between the liquid and the metal at the interfaces is crucial for optimising performance. Through a series of molecular dynamics simulations, this thesis explores the structural, thermodynamic, and dynamical properties of [BMIM][BF_4] confined between gold surfaces, providing detailed insights into their behaviour under both equilibrium and non-equilibrium conditions.

The thesis begins by establishing the baseline behaviour of [BMIM][BF_4] at a gold interface under equilibrium conditions. It reveals the formation of distinct layered structures, where the ions organise themselves based on electrostatic and van der Waals interactions. These findings highlight the significant role of the interface in dictating the overall properties of the RTIL, including its diffusion coefficients and interfacial free energy.

Building on this, the study then investigates how external forces, specifically shear flow, alter the RTIL's behaviour. The application of shear flow leads to the formation of a solid-like, glassy layer at the interface, which extends over several nanometres from the gold surface. This non-equilibrium state is characterised by deviations from the ideal linear Couette flow and significant changes in viscosity and friction, which are critical for understanding the RTIL's performance in dynamic applications such as lubrication and energy storage.

The thesis proceeds with introducing a constant metal-surface charge approach to investigating the phenomena at the RTIL-gold interface, away from the potential of zero charge (PZC). In order to ensure the accuracy of these simulations, the thesis validates the use of a polarisable gold model for such off-PZC calculations through a simpler system involving NaCl solution at a gold interface. This study confirms the model's ability to capture the nuanced electrostatic interactions at the interface, particularly under varying charge conditions, which are essential for realistic simulations of more complex systems like RTILs.

The final phase of the research explores the behaviour of [BMIM][BF_4] at a charged gold interface, revealing significant changes in ion distribution, electric double layer formation, and dynamical properties. The study demonstrates how surface charge, coupled with image charge contribution, enhances ion ordering and the differential capacitance of the liquid, and the extent to which it influences the viscosity and mobility of the RTIL, providing critical insights for the design and optimisation of devices such as supercapacitors and batteries.

Overall, this thesis contributes to the fundamental understanding of RTIL-metal interactions, offering detailed insights that are vital for the development of next-generation materials and technologies. By systematically exploring the RTIL's behaviour under different interfacial conditions, the research lays the groundwork for future advancements in the application of RTILs in energy storage, catalysis, and beyond.

ZUSAMMENFASSUNG

Diese Arbeit untersucht das Verhalten von ionischen Flüssigkeiten bei Raumtemperatur (RTILs), insbesondere von 1-Butyl-3-methylimidazoliumtetrafluorborat ([BMIM][BF_4]), an Goldgrenzflächen unter verschiedenen Bedingungen, darunter Gleichgewicht, Scherströmung und elektrifizierte Grenzflächen. Die Studie wurde durch die zunehmende Bedeutung von RTILs in fortschrittlichen Anwendungen wie Energiespeicherung, Katalyse und Schmierung motiviert, bei denen das Verständnis der molekularen Wechselwirkungen zwischen der Flüssigkeit und dem Metall an den Grenzflächen für die Leistungsoptimierung von entscheidender Bedeutung ist. Anhand einer Reihe von Molekulardynamiksimulationen untersucht diese Arbeit die strukturellen, thermodynamischen und dynamischen Eigenschaften von [BMIM][BF_4], das zwischen Goldoberflächen eingeschlossen ist, und liefert detaillierte Einblicke in sein Verhalten sowohl unter Gleichgewichts- als auch unter Nichtgleichgewichtsbedingungen.

Die Arbeit beginnt mit der Ermittlung des Basisverhaltens von [BMIM][BF_4] an einer Goldgrenzfläche unter Gleichgewichtsbedingungen. Sie zeigt die Bildung ausgeprägter Schichtstrukturen, in denen sich die Ionen aufgrund elektrostatischer und Van-der-Waals-Wechselwirkungen selbst organisieren. Diese Ergebnisse unterstreichen die bedeutende Rolle der Grenzfläche für die Gesamteigenschaften des RTIL, einschließlich seiner Diffusionskoeffizienten und der Grenzflächen-Freien Energie.

Auf dieser Grundlage untersucht die Studie anschließend, wie externe Kräfte, insbesondere Scherkräfte, das Verhalten von RTIL verändern. Die Einwirkung von Scherkräften führt zur Bildung einer feststoffähnlichen, glasartigen Schicht an der Grenzfläche, die sich über mehrere Nanometer von der Goldoberfläche aus erstreckt. Dieser Nichtgleichgewichtszustand ist durch Abweichungen vom idealen linearen Couette-Fluss und signifikante Veränderungen der Viskosität und Reibung gekennzeichnet, die für das Verständnis der Leistung der RTIL in dynamischen Anwendungen wie Schmierung und Energiespeicherung von entscheidender Bedeutung sind.

Die Arbeit fährt fort mit der Einführung eines Ansatzes mit konstanter Metalloberflächenladung zur Untersuchung der Phänomene an der RTIL-Gold-Grenzfläche, abseits des Null-Ladungspotenzials (PZC). Um die Genauigkeit dieser Simulationen zu gewährleisten, validiert die Dissertation die Verwendung eines polarisierbaren Goldmodells für solche Off-PZC-Berechnungen durch ein einfacheres System mit einer NaCl-Lösung an einer Gold-Grenzfläche. Diese Studie bestätigt die Fähigkeit des Modells, die nuancierten elektrostatischen Wechselwirkungen an der Grenzfläche zu erfassen, insbesondere unter wechselnden Ladungsbedingungen, die für realistische Simulationen komplexerer Systeme wie RTILs unerlässlich sind.

Die letzte Phase der Forschung untersucht das Verhalten von [BMIM][BF_4] an einer geladenen Goldgrenzfläche und zeigt dabei signifikante Veränderungen in der Ionenverteilung, der Bildung einer elektrischen Doppelschicht und den dynamischen Eigenschaften. Die Studie zeigt, wie die Oberflächenladung in Verbindung mit dem Beitrag der Bildladung die Ionenordnung und die Differentialkapazität der Flüssigkeit verbessert und inwieweit sie die Viskosität und Mobilität des RTIL beeinflusst, und liefert damit wichtige Erkenntnisse für die Konstruktion und Optimierung von Geräten wie Superkondensatoren und Batterien.

Insgesamt trägt diese Arbeit zum grundlegenden Verständnis der Wechselwirkungen zwischen RTIL und Metallen bei und liefert detaillierte Erkenntnisse, die für die Entwicklung von Materialien und Technologien der nächsten Generation von entscheidender Bedeutung sind. Durch die systematische Untersuchung des Verhaltens von RTIL unter verschiedenen Grenzflächenbedingungen legt die Forschung den Grundstein für zukünftige Fortschritte bei der Anwendung von RTIL in der Energiespeicherung, Katalyse und darüber hinaus.

PUBLICATIONS

Parts of this thesis have been taken from the following publications:

- S. NTIM and M. Sulpizi. Role of image charges in ionic liquid confined between metallic interfaces. *Physical Chemistry Chemical Physics*, 22(19):10786–10791, May 2020. ISSN 1463-9084. doi: 10.1039/D0CP00409J. URL https://pubs.rsc.org/en/content/articlelanding/2020/cp/d0cp00409j. Publisher: The Royal Society of Chemistry.[1]

- S. NTIM and M. Sulpizi. Effects of shear flow on the structure and dynamics of ionic liquids in a metallic nanoconfinement. *Physical Chemistry Chemical Physics*, 23(42): 24357 – 24364, November 2021. ISSN 1463-9084. doi: 10.1039/D1CP01055G. URL https://pubs.rsc.org/en/content/articlelanding/2021/cp/d1cp01055g. Publisher: The Royal Society of Chemistry.[2]

- S. NTIM and M. Sulpizi. Molecular dynamics simulations of electrified interfaces including the metal polarisation. Physical Chemistry Chemical Physics, 25(34):22619 – 22625, August 2023. ISSN 1463-9084. doi: 10.1039/D3CP01472J. URL https://pubs.rsc.org/en/content/articlelanding/2023/cp/d3cp01472j. Publisher: The Royal Society of Chemistry.[3]

- S. NTIM and M. Sulpizi. Differential Capacitance of Ionic Liquid Confined between Metallic Interfaces. The Journal of Physical Chemistry B, February 2024. ISSN 1520-6106. doi: 10.1021/acs.jpcb.3c08042. URL https://doi.org/10.1021/acs.jpcb.3c08042. Publisher: American Chemical Society.[4]

Other publications during this period of studies.:

- R. Baez, L. A. Baptista, S. NTIM, P. Manidurai, S. Espinoza, C. Ramanan, R. Cortes-Huerto, and M. Sulpizi. Role of pH in the synthesis and growth of gold nanoparticles using L-Asparagine: A combined experimental and simulation study. *Journal of Physics: Condensed Matter*, 2021. ISSN 0953-8984. doi: 10.1088/1361-648X/abf6e3. URL http://iopscience.iop.org/article/10.1088/1361-648X/abf6e3.

- R. N. A. Akoto, H. Osei, E. N. Wiah, and S. NTIM. Dynamics of Silica Nanofluid Under Mixed Electric Field Effect. *Sustainable Education and Development – Sustainable Industrialization and Innovation*, 1088–1098, Cham, 2023. Springer International Publishing. ISBN 978-3-031-25998-2. doi: 10.1007/978-3-031-25998-2_84.

1 PERMISSION: This article, included in chapter 2, is "Reproduced with permission from the Royal Society of Chemistry"

2 PERMISSION: This article, included in chapter 3, is "Reproduced with permission from the Royal Society of Chemistry"

3 PERMISSION: This article, included in chapter 4, is "Reproduced with permission from the Royal Society of Chemistry"

4 PERMISSION: This article, included in chapter 5, is "Reprinted (adapted) with permission from S. Ntim and M. Sulpizi. Differential Capacitance of Ionic Liquid Confined between Metallic Interfaces. The Journal of Physical Chemistry B, February 2024. ISSN 1520-6106. https://doi.org/10.1021/acs.jpcb.3c08042". Copyright ©2024, American Chemical Society.

ACKNOWLEDGMENTS

I want to especially thank my advisor Marialore (Lore). I could not have asked for a better advisor. You always availed yourself, giving me direction and drawing out excellence in me. Beyond my studies, you were also genuinely interested in my well-being and even in that of my family—I am truly grateful to have worked with you.

Speaking about family, I would like to thank my dear Yaa Boatemaa and our little boys, for keeping me grounded and focused. To my Mama and Papa, thank you for your support and your prayers—the LORD heard them.

Finally, I would like to thank the NANOTRANS—a European Union's Horizon 2020 research grant, the Deutsche Forschungsgemeinschaft for financial support under the TRR146 project, and the Zentrum Für Datenverarbeitung of the Johannes Gutenberg Universität Mainz for resources for computation.

CONTENTS

LIST OF TABLES

ACRONYMS

RTIL Room-Temperature Ionic Liquid

IL Ionic Liquid

EDLC Electrochemical Double-Layer Capacitor

EDL Electric Double Layer

DLVO Derjaguin–Landau–Verwey–Overbeek

PZC Potential of Zero Charge

SFG Sum Frequency Generation

SEIRA Surface-Enhanced Infrared Absorption

MD Molecular Dynamics

PME Particle Mesh Ewald

AFM Atomic Force Microscopy

SFB Surface Force Balance

1

INTRODUCTION

The need for compact and portable sources of stored energy has drastically, in the past decades, placed a weight of importance on electrochemical energy storage devices, and given incentive to their research and development. These energy storage devices have been crucial in technological advances made in, for example, the smartphone industry as well in other industries developing mobile electronics. Nowadays, due the global attention on the shift to renewable energy sources, efficient storage of energy has all the more emphasised the need to advance research in renewable and sustainable energy storage devices. Not only are they expected to be instrumental in advancing heavily dependent industries like the automobile industry, offering high capacities, but also are expected to be highly efficient to serve, for example, as the intermediary link between renewable energy sources and the national grid [1]. Very important to the discussion are Electrochemical Double-Layer Capacitors (EDLCs), so called supercapacitors. Although they have comparatively (with respect to batteries) low energy capacity, their high-power density [2] lends them indispensable to complementing higher energy-capacity devices like the Li-ion battery [3]. The charge/discharge mechanism of these EDLCs, unlike batteries, are non-Faradaic and do not involve chemical phase changes. This gives them high recyclability and make them appealing for sustainable energy storage devices [4].

EDLCs are significantly different from other capacitors. Conventionally, a capacitor is a system of metal electrodes on opposite sides of a dielectric separation, where due to the difference in potential as a result of the charges on each electrode surface, an electric field **E** is created within the dielectric. Figure 1 shows such a conventional parallel-plate capacitor. In such a system, the potential difference between the plates is the amount of

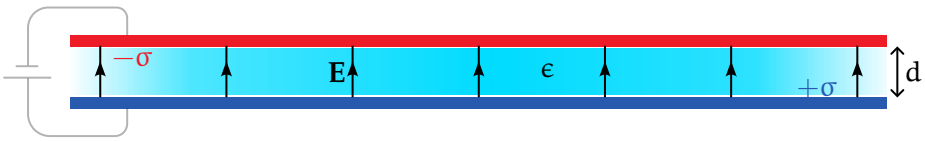

Figure 1: A conventional parallel-plate capacitor with surface charge density σ separated by d with a material of permittivity ϵ occupying the separation.

work per unit charge needed for a small charge to be moved between the two surfaces. For two plates with surface area A having surface charge density $\pm\sigma = \pm Q/A$ separated by a small distance d, where that separation is filled with a material of permittivity ϵ, the potential difference V may be given in terms of the field energy stored in the two-plate system $E = \sigma/\epsilon$ expended across d

$$\begin{aligned} V &= E \cdot d \\ &= \frac{d\sigma}{\epsilon} \\ &= \frac{Qd}{A\epsilon}. \end{aligned} \tag{1}$$

From Equation 1, the important quantity called the capacitance, related to the geometry of the plates and the intrinsic relative permittivity or dielectric constant $\epsilon_r = \epsilon/\epsilon_0$ of the material between the plates, is established to be

$$C = \frac{\epsilon A}{d} \tag{2}$$

The capacitance determines or quantifies the energy-storing performance of such two-plate capacitors. From Equation 2, it is obvious that for such capacitors, the ability to store energy hinges on three tunable parameters: the surface area of the plates, the distance between them, and the dielectric constant of the material in the plate separation. While this is generally the case, Equation 2 is no longer sufficient in describing EDLCs. In an EDLC, the material separating the electrodes is not a non-conducting uniform dielectric material as has been described so far, but rather an electrolyte with mobile charges. The introduction of mobile charges in the separation material significantly modifies the operating principles of the capacitor. When a potential is applied to the EDLC, just as for a typical capacitor, the mobile electrode charges accumulate on its interior surface. However, in the simplest description, the mobile charges in the separating medium respond to the accumulation of charges at the electrode, where there is also now an accumulation of counter electrolyte charges (and concomitant dissipation of like-charges) at the electrode-electrolyte interface, locally screening the electrode surface charges. This creates a stark variation in the charge density within the electrolyte where the region at the electrode-electrolyte interface no longer resembles the bulk. Thus, the introduction of mobile charges sets up what is traditionally referred to as the Electric Double Layer (EDL). This layer refers to the interfacial region where the charge density differs significantly from that of the bulk material farther away from the interface. The EDL is predominantly counter to the charge on the electrode to which it is formed as a response. This arrangement sets up a "capacitor" within the capacitor where now an electrode is paired with a layer of electrolyte ions.

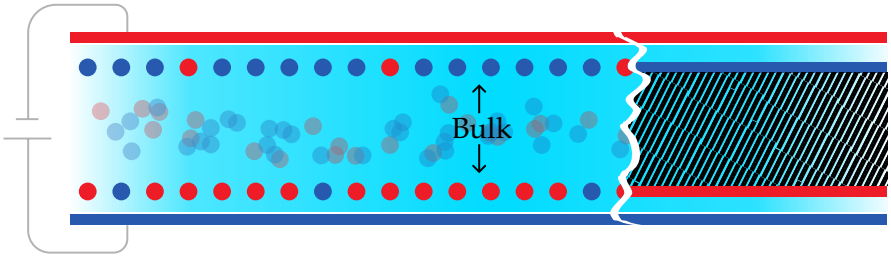

Figure 2: A parallel-plate supercapacitor resembling two conventional capacitors separated by bulk.

There are various progressive theoretical descriptions of the nature of the interfacial electrolyte charge distribution, the EDL, yet even in this simplified picture, Equation 2 breaks down since the parameters may no longer be as clearly defined or measurable as they are in a conventional capacitor [1]. In realistic EDLCs, for example, the electrodes used are highly disordered porous materials, in order to greatly increase the interfacial area in which case A is increased yet poorly defined.

1.1 THE PROGRESSIVE PICTURE OF THE ELECTRIC DOUBLE LAYER

Previously, we described a setup of an EDLC where counter charges accumulated at the interface and thereby forming internally a two-layer system of opposite charges there at the interface. This was Helmholtz's 1853 idea of the distribution of counter ions in the electrolyte. In this view, shown in Figure 3a, the counter-ions form a compact somewhat 2-dimensional layer referred to as the Helmholtz double layer. In this model, the potential in the electrolyte drops linearly across the double-layer region from the potential at the electrode surface to the electrolytic bulk potential. This description of the EDL seemed to be the most intuitive explanation but lacked accuracy. For example, the mobility of ions in the electrolyte arises not only from drift and current induced by an applied potential, but also from significant contributions due to thermal fluctuations within the system. When thermal fluctuations are significant, with respect to the electrostatic and specific ion-surface interactions, for example, the Helmholtz EDL no longer holds. Gouy's work on the formation of electric charge at the interface and Chapman's work on electrocapillarity, introduced thermal fluctuations in their representation of the EDL. In their theory, ions were represented as point charges as shown in Figure 3b, having their distribution governed by Boltzmann's theory and Poisson's equation relating the electric potential to the charge density. Consider a set of ion species in the electrolyte. The Poisson equation, given that the electrostatic potential field in the electrolyte is Φ and the charge density therein is ρ, states that

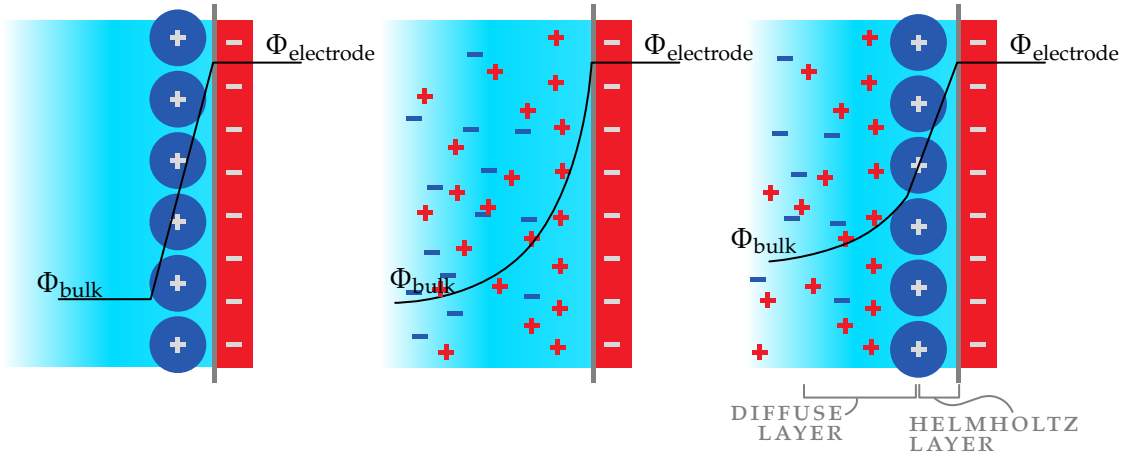

(a) Helmholtz model of compact two-dimensional array of counter-ions in electrolyte at interface

(b) Gouy model of point charges subject to diffusion by thermal agitation

(c) Stern model, a combination of both models

Figure 3: Electric Double Layer models, showing the transition from the Helmholtz picture through to the Stern picture. The figures show only the cathodic end of the capacitor.

$$\nabla^2\Phi = -\frac{\rho}{\epsilon} \tag{3}$$

If we limit ourselves to a flat interface geometry, then in one dimension, along the normal to the interface (taking it to be x), we have

$$\frac{d^2\Phi}{dx^2} = -\frac{\rho}{\epsilon} \tag{4}$$

The charge density ρ can be written as the sum of contributions from each ion species. Each ith species having a valency of z_i would carry a charge $q_i = z_i e$ where e is the elementary charge. The charge density associated with it would be $n_i z_i e$ where n_i is the number of species i per unit volume. Then the total charge density would be

$$\rho = \sum_i n_i z_i e \tag{5}$$

and each ion of type i in the field Φ would therefore have an associated electrostatic energy $U_i = q_i \Phi = z_i e \Phi$. According to Boltzmann's energy distribution, the probability of finding an ion with the energy U_i is $n_i \propto \exp(-\beta U_i)$. By introducing $n_{i,0}$ as the constant of proportionality (which can be shown to be the concentration of the ith species at zero potential i.e. bulk, far from interface), we have

$$n_i = n_{i,0} \exp(-\beta z_i e \Phi) \tag{6}$$

Using Equations 6 and 5 in Equation 4, we have a Poisson-Boltzmann equation

$$\frac{d^2\Phi}{dx^2} = -\frac{1}{\epsilon} \sum_i n_{i,0} z_i e \exp(-\beta z_i e \Phi) \tag{7}$$

It should be noted that this model, the Gouy-Chapman model, makes some crucial assumptions. First is that the electrolyte is of uniform dielectric properties independent of applied potential, distance from electrode or any other physical parameters which may be present. Second is that the Poisson potential in Equation 4 is identical to the Boltzmann potential in Equation 6. This is generally not the case. The Poisson potential is a local mean electrostatic potential field i.e., an ensemble average of electrostatic potentials while the Boltzmann potential is a potential of mean force experienced by an ion i.e., an effective potential energy per unit ion that determines the equilibrium ion distribution. By this assumption, all other contributions to the effective force potential like electrostatic correlations (ion-ion, ion-solvent) and excluded volume effects are neglected. Third is that the ions are point-ions. This particular assumption, putting no restriction or limit on the packing of ions, overestimates the rate at which counter-ions accumulate at the interface with respect to a change in potential drop due to the applied potential. This quantity, called the differential capacitance $C_d = d\sigma/d\Delta\Phi$ holds crucial information about physical and chemical processes at the interface. In spite of these, this Poisson-Boltzmann equation is quite accurate for dilute electrolytes with concentrations $\leqslant 1\,\text{M}$ at low surface potentials (close to Potential of Zero Charge (PZC)) [8, 9], where the aforementioned assumptions are nearly true and valid.

An interesting simplification arises when we have a symmetric electrolyte with equal valency on both cation and anion species. In this case, n_0 being the electrolyte bulk number density, we have

$$\begin{aligned}
\frac{d^2\Phi}{dx^2} &= -\frac{n_0 e}{\epsilon}(z_+ \exp(-\beta z_+ e\Phi) + z_- \exp(-\beta z_- e\Phi)) \\
&= -\frac{n_0 e z}{\epsilon}(\exp(-\beta z e\Phi) - \exp(\beta z e\Phi)) \\
&= \frac{2 n_0 e z}{\epsilon} \sinh(\beta z e\Phi)
\end{aligned} \tag{8}$$

For a very weak potential, $\beta z e \Phi \ll 1$ and $\sinh(\beta z e \Phi) \approx \beta z e \Phi$ so that we obtain a linearised differential equation

$$\begin{aligned} \frac{d^2\Phi}{dx^2} &\approx \frac{2\beta n_0 e^2 z^2}{\epsilon}\Phi \\ &= \kappa^2 \Phi \end{aligned} \tag{9}$$

where $\kappa^2 = 2\beta n_0 e^2 z^2 \epsilon^{-1}$. This is a differential equation, known as the Debye-Hückel approximation, whose general solution is $\Phi = A\exp(\kappa x) + B\exp(-\kappa x)$. For convenience, $\Phi(x =\!\!\rightarrow +\infty \equiv \text{bulk}) \rightarrow 0$ and $\Phi(x \rightarrow 0) \rightarrow \Phi_{el}$ where Φ_{el} is the potential at the electrode surface, so that the potential drop $\Delta\Phi = \Phi_{el} - \Phi(\text{bulk}) = \Phi_{el}$. Hence

$$\Phi = \Phi_{el}\exp(-\kappa x) \tag{10}$$

We have therefore a decaying exponential function for Φ with a decay constant

$$\begin{aligned} \lambda &\equiv \kappa^{-1} \\ &= \sqrt{\frac{\epsilon}{2\beta e^2 z^2 n_0}} \end{aligned} \tag{11}$$

known as the Debye screening length. This is a characteristic length over which the electrostatic potential and its associated space charge decay from electrode surface. Beyond a few λ, the electrolyte is effectively charge-neutral as the potential would have decayed and approached zero. Using Equation 10 and Gauss' law at the surface of the electrode

$$\left.\frac{d\Phi}{dx}\right|_{x=0} = \frac{\sigma}{\epsilon}, \tag{12}$$

we have the surface charge density to be

$$\sigma = \kappa\epsilon\Phi_{el}.$$

Hence the differential capacitance in the Debye-Hückel diffuse layer,

$$C_d^{diff} = \kappa\epsilon,$$

is independent of potential.

In general, the Poisson-Boltzmann equation, Equation 4, may be analytically solved exactly [10]. Using the relation

$$\frac{d}{dx}\left(\frac{d\Phi}{dx}\right)^2 = 2\frac{d\Phi}{dx}\frac{d^2\Phi}{dx^2}$$

the Poisson-Boltzmann can be transformed into a first order differential equation by multiplying first with $2d\Phi/dx$ and integrating once with respect to x.

$$2\frac{d\Phi}{dx}\frac{d^2\Phi}{dx^2} = -\frac{2}{\epsilon}\sum_i n_{i,0} e z_i \exp(-\beta z_i e\Phi)\cdot\frac{d\Phi}{dx} \tag{13}$$

$$\int_{x'}^{\infty}\frac{d}{dx}\left(\frac{d\Phi}{dx}\right)^2 dx = -\frac{2}{\epsilon}\int_{\Phi(x')}^{0}\sum_i n_{i,0} e z_i \exp(-\beta z_i e\Phi)\, d\Phi \tag{14}$$

$$\begin{aligned} \left(\frac{d\Phi}{dx}\right)^2_{x=x'} &= \frac{2}{\epsilon}\sum_i \frac{n_{i,0} e z_i}{\beta e z_i}\left(\exp(-\beta z_i e\Phi(x')) + \xi\right) \\ &= \frac{2}{\beta\epsilon}\sum_i n_{i,0}\left(\exp(-\beta z_i e\Phi(x')) - 1\right) \end{aligned} \tag{15}$$

where ξ is an integration constant whose value is obtained from the boundary condition that at $x \to +\infty$ (bulk) both Φ and its derivative with x approach 0. At the surface of the electrode, $x' = 0$ and $\Phi(0) = \Phi_{el}$. Then by Gauss' law (Equation 12),

$$\sigma = \pm\sqrt{\frac{2\epsilon}{\beta}\sum_i n_{i,0}\left(\exp(-\beta z_i e\Phi_{el}) - 1\right)}. \tag{16}$$

For a symmetric valency electrolyte, noting that

$$e^{\pm y} - 1 = \pm 2e^{\pm y/2}\sinh(y/2),$$

$$\begin{aligned}\sigma &= \pm\sqrt{\frac{2\epsilon n_0}{\beta}\left(4\sinh^2\left(\frac{\beta z_i e\Phi_{el}}{2}\right)\right)} \\ &= \pm\sqrt{\frac{8\epsilon n_0}{\beta}}\sinh\left(\frac{\beta z_i e\Phi_{el}}{2}\right)\end{aligned} \tag{17}$$

This gives us a relation between the surface charge density and the potential at the electrode by which we find that the differential capacitance in the diffuse double layer $C_d^{diff} = C_d^{diff}(\Delta\Phi)$ is

$$\begin{aligned}C_d^{diff} &= \sqrt{2\beta e^2 z^2 n_0 \epsilon}\cosh\left(\frac{\beta ez\Phi_{el}}{2}\right) \\ &= \kappa\epsilon\cosh\left(\frac{\beta ez\Phi_{el}}{2}\right).\end{aligned} \tag{18}$$

While this capacitance relation proved useful qualitatively aligning with measurements at small applied voltages, it could not reproduce experimental values. One of the more obvious issues is that the differential capacitance monotonically increases with the potential, in contrast with experimental observation. This discrepancy led Stern to treat the double layer as of two components (Figure 3c). The first is an inner region where the ion distribution is per adsorption processes. The ions in this layer were recognised to have a finite size and therefore a distance of nearest approach to the electrode, which allowed for a limit to the packing of adsorbed ions in this region. This corresponds well to the Helmholtz compact double layer (Figure 3a) with differential capacitance C_d^H. Beyond this region is the diffuse region, where ions freely move under thermal and electrical forces, corresponding to the Gouy-Chapman diffuse layer whose differential capacitance we have already established to be C_d^{diff}. It should be noted however, that because of this compartmentalisation, both σ (Equation 17) and C_d^{diff} (Equation 18) are now functions of the potential at the diffuse boundary and not the potential at the electrode interface. Stern's model expresses

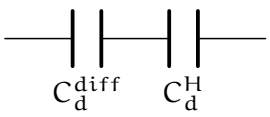

Figure 4: Schematic of the Stern model in Figure 3c, depicting the double layer as two capacitors in series.

the double layer capacitance as one from two capacitors in series (Figure 4) where now the total differential capacitance is

$$C_d = \frac{C_d^H \times C_d^{diff}}{C_d^H + C_d^{diff}}. \tag{19}$$

From Equation 19, the differential capacitance of the double layer is determined by the lesser of C_d^H and C_d^{diff} and Figure 5 shows an example Gouy-Chapman-Stern capacitance. Thus, by introducing a distance of nearest approach and placing a geometrical limit on the compact inner region, the extremely high capacitances from the Gouy-Chapman model is naturally avoided.

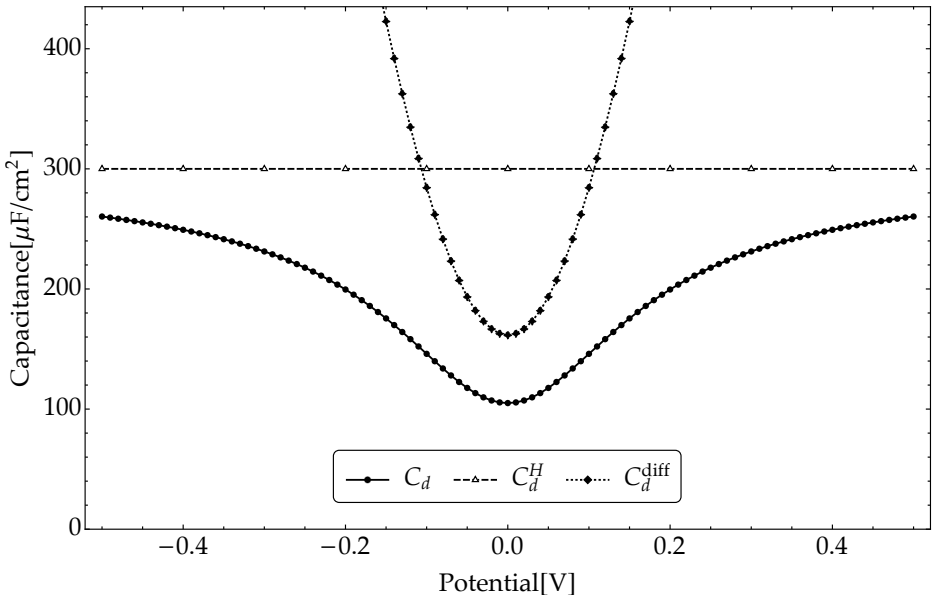

Figure 5: An example differential capacitance of the Gouy-Chapman-Stern model and its components at the Helmholtz and diffuse layers.

Stern's treatment, however, did not account for specifically adsorbed ions. According to Grahame, Stern's model works well for electrolytes like NaF where both Na^+ and F^- are strongly hydrated, but inaccurately for certain other ions like Cl^- and Br^- which strongly interact with the electrode. Grahame addressed this particular problem by refining the compact layer in Stern's model, making a distinction between the inner and outer Helmholtz planes. Grahame's work, recognising the different effective ionic radii and distance of nearest approach (which result from the specific chemical nature of the ion like polarisability and lone-pair donation), proved to be a crucial correction to resolving the discrepancy with experiment. While the Grahame treatment has improved our understanding of the nature of the EDL, the progressive development of the interfacial double layer theory is a testament to the sensitivity of the EDL to multiple variables. Others have also extended the Gouy-Chapman-Stern model to correct its simplified view of the inner compact layer, to include strong metal electrode-solvent interactions, solvent reduction, and other interactions [12, 13, 14]. In the past two decades, however, the attention has shifted to correcting the discrepancy between theory and experiment by improving the theoretical understanding of the diffuse layer [15, 16, 17, 18].

1.2 THE ELECTRIC DOUBLE LAYER NATURE IN CONCENTRATED ELECTROLYTES

The assumptions underlying the classical Gouy-Chapman model of the EDL render it (together with the refinements by Stern and Grahame) accurate only for electrolytes of low ionic concentration. When a high ion concentration is considered, where we can expect non-negligible correlation effects, those models break down and are highly inaccurate. Grahame's model, for example, focuses on the complexities in the EDL that arise from the solvation of ions. What if there is little to no solvent molecules to solvate the ions? What is the nature of the EDL in such a case? These questions are, in fact, necessary to raise while on the topic of supercapacitors where there is a need for higher operating voltage since the energy density is quadratically dependent on it ($U = 1/2CV^2$). Aqueous systems like those which the Grahame model describes, typically have a low decomposition voltage 1.23 V to 1.5 V [4] while nonaqueous, aprotic solvents operate at much higher voltages (e.g., 3.4 V to 4.0 V) [4].

In order to account for high concentration effects, several modified Poisson-Boltzmann equations have been developed [15, 16, 18]. A particularly elegant and widely cited approach is due to Kornyshev, who used a lattice-gas model to describe the occupancy of ions. The ion distributions that his method derive are rather Fermi-like, leading him to refer to the equations as Poisson-Fermi equations. The double layer capacitance in this model was found to be

$$C_d^{\mathtt{diff}} = C_0 \frac{\cosh(u_0/2)}{1 + 2\gamma \sinh^2(u_0/2)} \sqrt{\frac{2\gamma \sinh^2(u_0/2)}{\ln\left(1 + 2\gamma \sinh^2(u_0/2)\right)}} \tag{20}$$

where

C_d^{diff}	Differential (specific) capacitance of the double layer, $C_d^{\text{diff}} = d\sigma/dU$.
C_0	Linear Gouy-Chapman capacitance, $C_0 = \varepsilon/\lambda$.
λ	Debye length.
ε	Dielectric permittivity (intermediate-frequency constant) of the medium.
u_0	Dimensionless surface potential, $u_0 = e\Phi/(k_B T)$.
γ	Lattice saturation parameter, $\gamma = 2c_0/c_{max}$.
c_0	Bulk concentration of one ionic species.
c_{max}	Maximal possible local ionic concentration.

γ plays a key role in determining the transition between Boltzmann-like and Fermi-like ion distribution and ultimately governs the shape of the capacitance curve. In Figure 6a two capacitance curves at low and high γ values are shown, where the low γ curve takes on a double-hump camel shape while the high γ curve has a bell shape. In the limit as $\gamma \to 0$ the logarithmic function becomes approximately equal to the numerator under the square-root and the whole capacitance expression approaches the Gouy-Chapman diffuse layer capacitance. At large γ, however, the Fermi-like distribution does not allow the ions to densely pack close to the electrode to effectively screen the surface charge. Instead, the double layer thickness effectively grows with electrode potential. In an electrolyte, the size and steric properties of the anion and cation species generally differ. To account for this

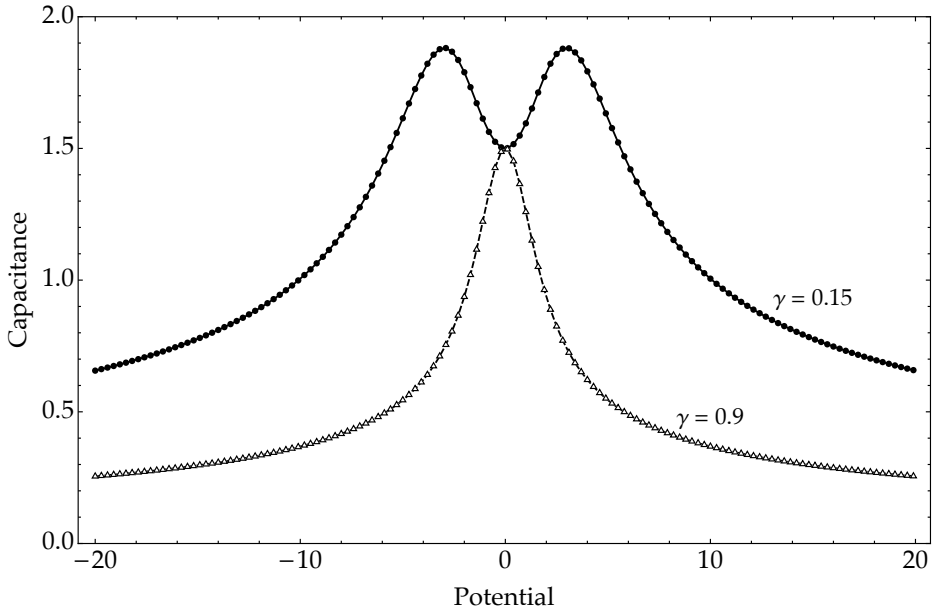

(a) Differential capacitance according to Kornyshev for symmetrically sized ions at two different lattice saturation.

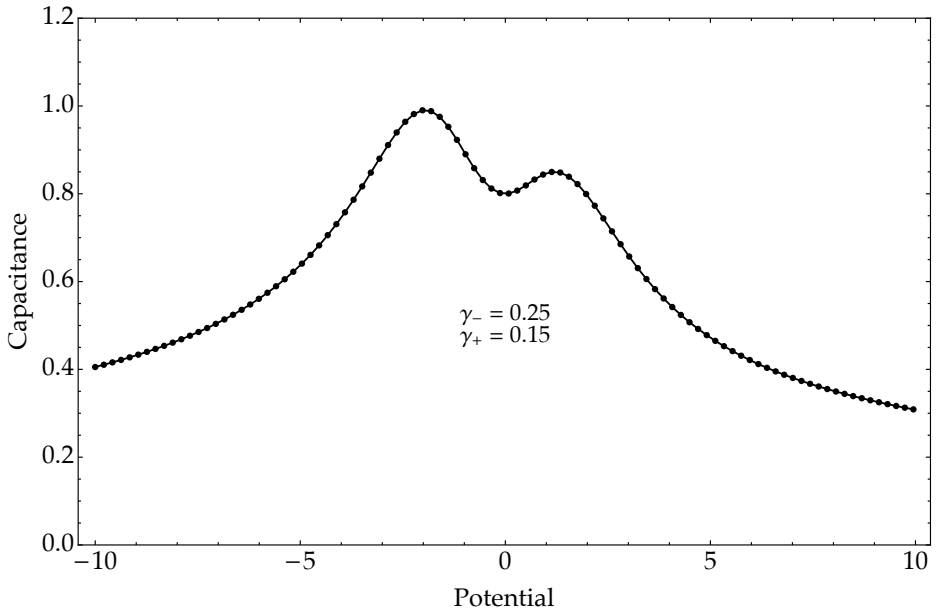

(b) Differential capacitance for asymmetric ion size, one at lattice saturation 0.25 and the other at 0.15

Figure 6: Kornyshev's differential capacitance curves as functions of electrode potential for symmetric and asymmetric ion sizes.

Kornyshev introduced a potential-dependent lattice-saturation parameter $\gamma = \gamma(u)$ as a sigmoidal function:

$$\gamma(u) = \gamma_- + \frac{\gamma_+ - \gamma_-}{1 + \exp(u)} \tag{21}$$

where γ_- and γ_+ correspond to the lattice saturation parameters for anions and cations respectively. Figure 6b shows a differential capacitance curve where $\gamma(u)$ has been used.

While this model is revelatory and captures key steric and crowding effects contributing to the differential capacitance, it is nonetheless a mean-field approximation, simplified to exclude ion-ion correlations. Extensions to include short-range correlations and overscreening have been developed to bridge the gap between the mean-field and atomistic descriptions [19]. These Landau-Ginzburg-type continuum approaches, that describe spatial dispersion, recover layering phenomena and explain why overscreening is dominant near the PZC. Further refinements introduce implicitly ion pairing by determining parameters through association equilibria, which reduce the concentration of free charge carriers and alter the shape of the capacitance [20]. The resulting changes in the degree of ion pairing dramatically alter the shape of the capacitance. Other generalisations have worked with Monte-Carlo simulations of ionic liquids as hard spheres to better capture finite ion size and anisotropy [21], while other refinements allow the local dielectric permittivity ϵ to vary with ion concentration or polarisability, capturing dielectric decrement effects near the electrode [22]. Dispersion forces and electrode-specific properties, such as roughness, have also been incorporated to explain observed capacitance camel shape and asymmetries [23, 24].

Although our understanding of the electrode-electrolyte interface has improved greatly in the last two decades, it is far from complete. A classic example of why we know the interface to be complex is the attempt at answering a seemingly simple question such as "Are room-temperature ionic liquids dense or dilute electrolytes?" The answer from intuition may not be justifiably correct. This has been a point of contention where arguments supporting one answer over another are not invalid. Gebbie et al. analysed the results of their surface force measurements on the $[C_4mim][NTf_2]$ Ionic Liquid (IL) using the Derjaguin–Landau–Verwey–Overbeek (DLVO) theory [25]. DLVO extends the electrostatic double layer (consisting of compact and diffuse layers) by accounting for van der Waals interactions. Gebbie et al. showed that DLVO can be used to quantitatively explain the screening behaviour of the IL, which exhibited a long-range exponentially decaying force (~10 nm to 13 nm) attributable to a diffuse electric double layer [25]. This implied the IL and possibly other aprotic ILs behave as dilute weak electrolyte solutions with effective dissociated ion concentrations of less than 0.1 % [25]. Following this was a back-and-forth between Perkin et al. and Gebbie et al. [26, 27]. Perkin et al. argued that the DLVO framework was inappropriate, contending that ILs are strongly dissociated ionic melts where the surface charge should be screened over much shorter distances, deeming the long-range force observation "surprising" [26]. Gebbie et al. countered by clarifying that ILs function as an "effectively neutral, coordinated cation-anion network" in equilibrium with a small fraction of dissociated ions, rather than simple exclusive ion pairs [27]. However, later experimental work by Smith et al. (of Perkin's group) confirmed the observation of long-range electrostatic screening, reporting effective decay lengths (λ_{exp}) that greatly exceed the theoretical Debye length by up to a factor of ~120 in concentrated 1 : 1 electrolytes, including ionic liquids, where λ_{exp} measured ~8.4 nm for 3.3 M $[C_4C_1Pyrr][NTf_2]$ [28]. This work further demonstrated that the screening length exhibits a complex nonmonotonic relationship with electrolyte concentration, initially decreasing as per Debye theory, reaching a minimum in the 0.1 M to 0.5 M range, and then increasing again with concentration in the highly concentrated regime [28]. This nonmonotonic trend was shown to be a general feature of concentrated electrolytes [28].

It should by now be abundantly clear that the complexity of the electrode-electrolyte interface, as we discover it to be, only grows with our supposed understanding of it. In

order to advance our knowledge and resolve some of these apparent conundrums, further work is required.

1.3 ROOM-TEMPERATURE IONIC LIQUIDS

An EDLC has two important components. The one component being the electrode and the other, the electrolyte. There is a wide variety of electrolytes to choose from to complete an EDLC. In general, the electrolyte is a liquid constituting ions and could either have a solvent or be solvent-free, ranging from aqueous electrolytes [29, 30, 31, 32, 33, 34] to organic electrolytes [33, 35], to solid-state polymer electrolytes [36, 37, 38, 39] and to ILs [40, 41, 42, 43, 44].

ILs have emerged as a unique class of materials with properties that are distinct from conventional electrolytes, making them suitable for a wide range of applications in energy storage, catalysis, and materials science. They are liquids comprising exclusively ions. Among these is a special class of ILs referred to as Room-Temperature Ionic Liquids (RTILs). An RTIL is a material that is comprised solely of ions and is liquid at and below room temperature, typically with a melting point between 100 °C and 150 °C [45, 46, 47, 48, 49]. In this sense the concept and discovery of RTILs have a long rich history [50]. Prior to the 1990s, research on RTILs was characterised by foundational discoveries, though it had not yet entered the phase of exponential growth driven by the "Green Chemistry" concept [50]. At the time, these low temperature molten salts were overwhelmingly alkylpyridinium chloroaluminates or, later, alkylimidazolium chloroaluminates (e.g., 1-methyl-3-ethylimidazolium chloride, MeEtImCl, combined with $AlCl_3$) [50, 51, 52]. The (MeEtImCl)$-AlCl_3$ system was chosen as a "baseline" melt primarily due to its favourable conductivity, viscosity, and wide liquid range [52]. Studies of the physical properties of dialkylimidazolium chloroaluminate binary melts, including phase transitions, densities, and conductivities, were also widely reported in 1984 [52]. However, the precise regulation of the Lewis acidity of these systems (a primary control parameter [53, 50]) was challenging due to their complex autosolvolytic equilibria and difficulty of accurate preparation [53, 54, 51]. Breakthroughs in the early 1990s with the discovery of organic anions (e.g., $[BF_4]^-$ and $[PF_6]^-$) for RTILs began yet another phase of interest in RTILs. Due to the unique properties and potential applications of RTILs, after BASF developed the BASIL process and made it public in 2002, the floodgates of interest and research in RTILs were wide open [47]. RTILs are desirable for their peculiar features. Table 1 presents a non-exhaustive list of the most important properties of RTILs and their applications.

The confinement of RTILs is particularly consequential, as it is considered essential for their peculiar properties and performance across various technological domains, including energy storage and transformation within supercapacitors [90, 91, 92, 93, 94, 95], batteries [96, 97, 98, 99], actuators [100, 101], and solar cells [69], as well as in catalysis and tribology [102]. The presence of an interface with a solid surface fundamentally modifies the bulk liquid properties [103], typically producing a layered structure whose extent is dependent on the liquid composition and the nature of the surface [103]. This layering has been widely confirmed through experiments, such as X-ray reflectivity [104], Atomic Force Microscopy (AFM) [105, 106], and Surface Force Balance (SFB) [57, 58, 107], in addition to simulations [49, 108, 109].

Beyond structural changes, confinement introduces peculiar mechanical and phase behaviour, demonstrating the capacity for tunability. For instance, an anomalous liquid–solid phase transition has been observed for 1-butyl-3-methylimidazolium tetrafluoroborate

PROPERTY	APPLICATIONS
Large, anisotropic organic ions with hydrophobic constituents leading to low melting points and liquid state at room temperature due to weakened Coulomb interactions and hindered crystallization [48, 55, 46].	Solvents for homogeneous and surface catalysis and synthesis [48, 45, 56]. Lubricants from macro- to nanoscale due to stability and layering [57, 58, 59].
Solvent-free electrolytes that remain liquid over a broad temperature range [60].	Electrolytes for power sources such as supercapacitors [61, 62, 63], batteries [64, 65, 66, 67], solar cells [68, 69], and prospective fuel cells [70].
Strong Coulombic binding resulting in low or ultralow volatility [71, 72, 73].	Lubricants in confined systems (minimal evaporation) [57, 58, 74, 75]. Liquids for electrowetting, variable lenses, and microfluidics [76, 77].
Electrochemically inert (less reactive ions) leading to high electrochemical and thermal stability. [60, 66, 64]	Media for electrochemical reactions, electrocatalysis, and electrodeposition [60, 78, 79, 80, 81, 82]. Electrolyte-gated transistors and superconductors [83, 84, 85, 86, 87].
Miscibility and tunability: RTILs can form "cocktails" or be diluted with dipolar solvents, yielding designer solvents [48, 45].	Designer solvents for selective reactions and extraction (metals, proteins, colloids, biomass conversion) [48, 56]. Chemical and electrochemical sensing [88, 89].
Practically unlimited number of RTILs are synthesisable [48, 45].	Custom-designed electrolytes with targeted functions across energy storage, catalysis, and sensing [67, 48, 45, 65, 68, 69, 74, 75].

Table 1: Key properties of RTILs and their derived applications.

([BMIM][BF_4]) confined between metallic surfaces [110], with the transition being more pronounced for materials of higher metallic nature [110, 111, 112]. It has been posited that this enhanced freezing is driven by image charges arising from the metallic nature of the confining surfaces [110]. This transition towards a solid-like phase is also crucial to the capability of RTILs to act as lubricants, showcasing lower friction than conventional oils [113, 114, 115, 116, 117, 118] and sometimes exhibiting quantised friction [119, 120, 121].

Confinement also influences the thermodynamic properties of RTILs, as shown through the Gibbs–Thomson equation [122]:

$$\Delta T = T_{confined} - T_{bulk} = \frac{2T_{bulk}\Delta\gamma}{\rho L_h \lambda_{width}} \tag{22}$$

where T_{bulk} is the freezing temperature of bulk RTIL, ρ its bulk density, L_h its latent heat of fusion and $\Delta\gamma = \gamma_{lw} - \gamma_{sw}$ is the difference in the liquid-wall and solid-wall interfacial free energies. The Gibbs-Thomson equation indicates that reducing the confinement width (λ_{width}) can significantly raise the freezing temperature [122].

When RTILs are confined between electrified interfaces, their properties become electrochemically tunable. A critical step in exploiting this tunability is understanding the structure of the EDL [123, 124, 125] and measuring the differential capacitance C_d as a function of the applied voltage [126], as we have discussed earlier in this chapter. Key features of the differential capacitance for RTIL, such as its ion size asymmetry, are well established [49, 17, 127], with models predicting higher capacitance values for the electrode containing smaller ions [128, 129, 130, 131]. Furthermore, the common camel shape of the capacitance has been attributed both to the nonspherical shape of the ions and the flexibility of their structure (charged heads and neutral tails) [21, 132, 133], which provides extra degrees of freedom for the field-induced charge rearrangements [49]. Changes in potential induce changes in the molecular orientation of ions; for instance, experimental studies using spectroscopic techniques such as Sum Frequency Generation (SFG) [134, 135] and Surface-Enhanced Infrared Absorption (SEIRA) [136] have suggested that imidazolium cations tend to lie flat at the electrode surface at negative potentials but tilt or are repelled at positive potentials [135, 134, 137]. This suggests the possibility to tune friction forces by surface charge density, suggesting the potential for electrotunable lubricants [138, 139], which further highlights the significance of RTIL tunability in confinement.

Additionally, under non-equilibrium conditions such as shear, the flow profile in nanoconfinement can deviate from the ideal linear Couette flow [140, 141], potentially leading to shear localisation [142, 143, 144] or even shear-induced crystallisation in a disordered, glassy state [145, 146].

Understanding the structural and dynamical properties of RTILs in confinement, particularly under variable potential and shear, remains critical for their successful application [123, 124].

1.4 MOTIVATION AND OBJECTIVES

The motivation for this thesis arises from the critical need to advance the fundamental understanding of RTILs, particularly 1-butyl-3-methylimidazolium tetrafluoroborate ([BMIM][BF_4]), when confined at solid interfaces, notably metallic surfaces such as gold, which is widely used in experimental studies and applications. In particular, the thesis seeks to address some persistent fundamental questions regarding the influence of the metallic nature of the confining surfaces on RTIL properties. Experimental observations have suggested that image charges may play a key role in phenomena like anomalous liquid-solid phase transition or "capillary freezing" observed in confined RTILs [110]. Moreover, when RTILs are subjected to motion, as in tribological systems, separating, in the laboratory, the fundamental electrostatic contribution from the viscous forces remains challenging [118]. This research therefore aims to provide a deeper, molecular-scale understanding of these complex interplays under diverse conditions, necessary to inform the design of more efficient and effective RTILs-based devices.

The specific objectives addressed by this research are multifaceted, focusing on characterising the confined RTIL system under equilibrium, non-equilibrium (shear flow), and electrified conditions:

1. CHARACTERISE EQUILIBRIUM INTERFACIAL PROPERTIES: The first objective is to characterise the equilibrium structure and dynamics of [BMIM][BF_4] at a neutral gold interface (Au(111)). This includes investigating the role of metal polarisation and image charges on the structure, dynamics, and thermodynamic properties of the confined RTIL. The results of this study are presented at length in chapter 2.

2. INVESTIGATE NON-EQUILIBRIUM BEHAVIOUR UNDER SHEAR: A crucial aim is to investigate the effects of shear flow on the RTIL-Gold interface, focusing on resultant changes in structure and dynamics. Key questions addressed within this objective include determining whether shear motion can induce a crystalline phase in [BMIM][BF_4] or lead to the development of a solid-like layer at the metallic surface, while assessing the tribological properties of the nanoconfined RTIL under shear. The work related to this objective is presented in chapter 3.

3. DEVELOP AND VALIDATE ELECTRIFIED POLARISABLE MODELS FOR METAL INTERFACES: This part of the research seeks to validate the use of electrified polarisable models that would consistently include the effects of image charges while still allowing the interface to be at potentials other than PZC. The validation uses a simpler electrolyte solution to set up the groundwork for the next objective. This validation work is presented in chapter 4.

4. EXAMINE RTIL AT ELECTRIFIED INTERFACE AND CHARGING MECHANISMS: The final objective is to examine the behaviour of [BMIM][BF_4] at a charged gold interface, with the goal of identifying differences from neutral conditions and elucidating the structure of the EDL. This includes calculating the differential capacitance, analysing the mechanisms by which the electrode charges (counterion adsorption versus co-ion desorption), and investigating how molecular orientation, interfacial crowding and dynamic properties evolve with applied electric potential. Detailed presentation is given in chapter 5.

1.5 METHODOLOGICAL APPROACHES

This research primarily employs atomistic Molecular Dynamics (MD) simulations as the core tool for investigating the molecular behaviour of ILs at metallic interfaces. MD simulations provide high-resolution insights into the molecular-level interactions, enabling the exploration of complex systems under various critical conditions, including changes in temperature, pressure, and externally applied shear flow or electric potential. The overall approach combines these detailed simulations with theoretical models to provide a comprehensive understanding of the phenomena governing the IL-metal interface.

The simulation system centres on the [BMIM][BF_4] confined between two flat Au(111) slabs. The atomistic model used for [BMIM][BF_4] is non-polarisable [147], but its parameters are specifically calibrated to accurately reproduce key experimental properties such as diffusion coefficient, ionic conductivity, shear viscosity and heat of vaporisation. Stand-

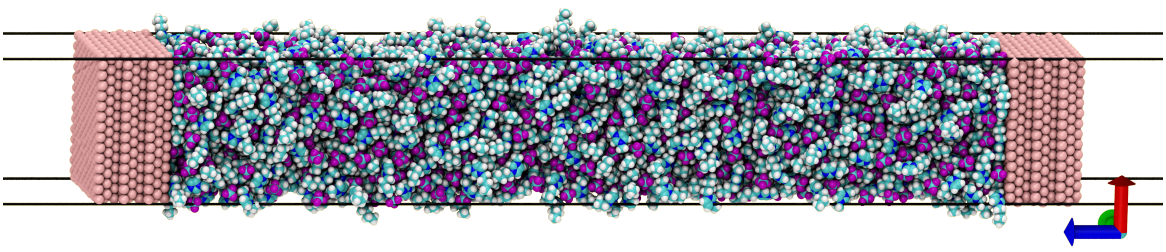

Figure 7: A unit box of RTIL in Au(111) slabs.

ard computational techniques are employed to manage the boundary effects inherent to

periodic MD systems. Two-dimensional periodic boundary conditions are enforced along the lateral (x and y) directions while interactions along confinement axis (z-direction) are treated using the Particle Mesh Ewald (PME) with slab correction to decouple periodic image interactions [148]. Simulations are performed using major computational packages, specifically GROMACS and LAMMPS.

A key methodological advancement of this research is the use of an advanced polarisable gold electrode model [149]. This approach addresses the anticipation that the metallic nature of the confining surfaces, particularly the presence of image charges, should significantly influence the static and dynamic properties of confined RTILs. Details of the polarisable model are presented in chapter 2.

To simulate conditions beyond PZC, the polarisable core-shell model is extended to describe the variable potential conditions. This is achieved by combining the polarisable model with the assignment of fixed additional charges on the electrode surface. This hybrid approach allows for the inclusion of local polarisation effects such as those induced by charge heterogeneity, that are elusive to traditional fixed-charge models.

Out-of-equilibrium properties are examined by applying shear flow through constant opposing velocities to the electrodes. In order to simulate realistic tribological conditions, the thermostat is strategically applied to allow thermal gradients to develop through the liquid.

This broader methodological framework is implemented with variations specific to each chapter. Accordingly, the individual details are therefore reserved for discussion within their corresponding chapters.

2

THE STRUCTURE, THERMODYNAMICS, AND DYNAMICS OF THE RTIL-GOLD INTERFACE AT EQUILIBRIUM—HOW IMPORTANT IS THE IMAGE CHARGE AT THE INTERFACE?

2.1 BACKGROUND AND MOTIVATION

The unique structure of RTILs in confinement is pivotal to their application in devices that require efficient energy storage and conversion. The presence of solid interfaces alters the liquid properties, often leading to a layered structure whose characteristics depend on both the liquid and the nature of the surface [103]. Experimental techniques like X-ray reflectivity, atomic force microscopy (AFM), and surface force balance (SFB) have demonstrated the formation of these layers [104, 105, 106, 57, 58, 107], yet the existence and properties of a diffuse layer remain controversial [25, 26, 27, 150, 151, 152, 110, 153, 154, 118, 155].

Electrostatic forces play a dominant role in determining the behaviour of ILs near metallic interfaces. Recent AFM experiments by Comtet et al. revealed an anomalous liquid-solid phase transition for [BMIM][BF_4], which is more pronounced on metallic surfaces. They proposed that image charges might drive this phase transition. These findings suggest that understanding the impact of image charges is crucial for predicting and controlling the behaviour of ILs in confined environments.

In this chapter we delve into investigating the behaviour of RTILs in confinement by exploring the impact of image charges on the IL 1-butyl-3-methylimidazolium tetrafluoroborate ([BMIM][BF_4]) confined between atomically flat gold electrodes in equilibrium conditions. Understanding the equilibrium behaviour of RTILs in confinement provides a baseline from which deviations can be measured when the system is subjected to external stimuli. This chapter serves as a reference for subsequent chapters that explore non-equilibrium conditions as well as more complex interfacial phenomena.

This work employs atomistic molecular dynamics simulations to elucidate the structural, dynamic, and thermodynamic properties of this system, aiming to shed light on the debated issue of interfacial layer characterisation and the influence of metallic surfaces on IL behaviour.

2.2 INTRODUCTION TO THE STUDY

2.2.1 *MD Simulation setup and details*

The molecular dynamics system was made of 1200 pairs of [BMIM][BF_4] (shown in Figure 8) confined in two slabs of either non-polarisable or polarisable gold. The non-polarisable gold (Figure 9 a) interacts purely through Lennard-Jones potentials whereas a single polarisable gold “atom" (Figure 9 b) consists of two masses of equal charge magnitudes but of opposing signs, so to give a net zero charge. The one mass of 195.96 u represents all of a gold atom (core) but its outermost deformable electron cloud, which is represented by the other mass of 1.00 u (dummy). Each mass has a charge magnitude of the elementary charge, e, the core being positive while the shell negative. The two masses are “bonded"

by a harmonic potential with a stiffness $k_r = 100.0\,\text{kcal mol}^{-1}\,\text{Å}^{-2}$ and with no separation when no external forces exist, $r_0 = 0.0\,\text{Å}$. The Lennard-Jones parameters are

$$\sigma_{ii} = 2.6246\,\text{Å} \qquad \epsilon_{ii} = 3.5\,\text{kcal mol}^{-1}$$

for the one mass representing the core and

$$\sigma_{ii} = 2.6246\,\text{Å} \qquad \epsilon_{ii} = 0.2\,\text{kcal mol}^{-1}$$

for the dummy. The Lorentz-Berthelot combination rules,

$$\epsilon_{ij} = \sqrt{\epsilon_{ii}\epsilon_{jj}} \qquad \sigma_{ij} = \frac{\sigma_{ii} + \sigma_{jj}}{2},$$

were used for interactions between nonidentical atoms, and the full interaction potential between the two masses of the polarisable gold "atom" was

$$V = \frac{1}{2}\sum_{\text{bonds}} k_r\,(r - r_0)^2 + \sum_{i<j} 4\epsilon_{ij}\left(\frac{\sigma_{ij}^{12}}{r_{ij}^{12}} - \frac{\sigma_{ij}^{6}}{r_{ij}^{6}}\right) - \frac{q_i q_j}{r_{ij}} \tag{23}$$

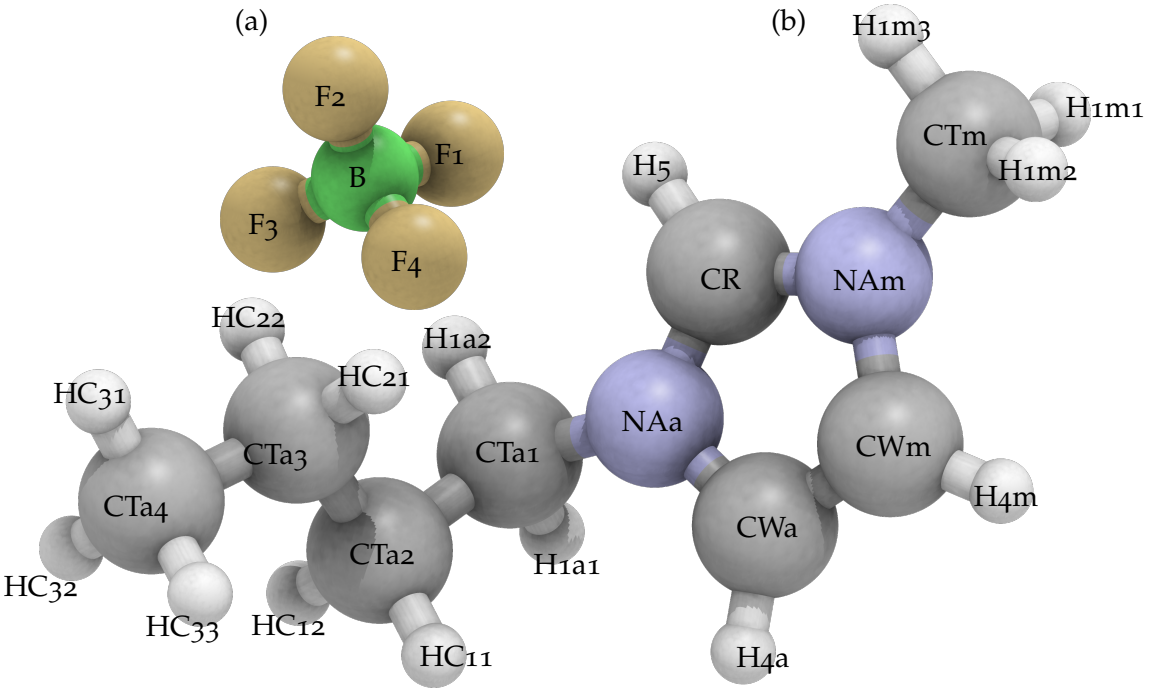

Figure 8: Ions of the [BMIM][BF_4] IL. (a) is the tetrafluoroborate (BF_4) anion and (b) is the 1-Butyl-3-methylimidazolium (BMIM) cation.

Each electrode slab was made of 9 layers of gold atoms in the (111) crystallographic plane. Five independent starting configurations of the ionic liquid confined in the slabs were sampled from an NPT run performed for 20 ns using a Nosé-Hoover thermostat at 298 K and semi-isotropic Berendsen barostat at 1 bar with compressibility only in the z-axis (normal to the slab surface) and with 3D periodic boundary conditions. Then NVT production runs were performed with each of the five starting configuration for 50 ns using a velocity rescale thermostat at 298 K. The systems were evolved at 0.5 fs timesteps and integrated with the leap-frog algorithm, saving information every 1000 molecular dynamics steps (0.5 ps). In such highly Coulombic systems, and for the purposes of this

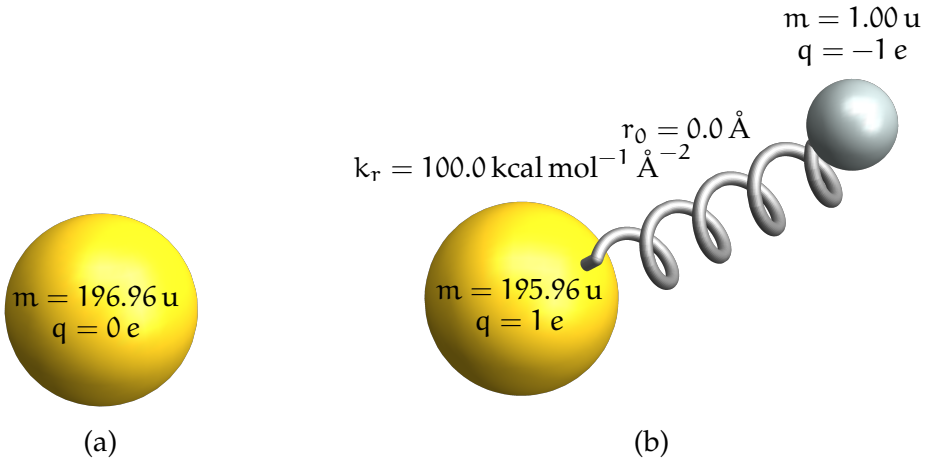

Figure 9: Non-polarisable (a) and polarisable (b) gold atoms.

study, inclusion of long-range Coulomb interactions was crucial. We employed the Particle Mesh Ewald (PME) with correction to slab geometries developed by Yeh and Berkowitz [148]. The slab geometry correction required vacuum of about three times (or more) of the system length, to be between the slabs, outside of the confining region. We used $4.055 \times 4.055 \times 250.000\,\mathrm{nm}^3$ as our simulation box dimensions in the production run, allowing for vacuum of 222 nm.

2.2.2 *Work of adhesion*

We calculated the work of adhesion using the dry surface approach by Leroy and Müller-Plathe [156]. In this scheme the calculation required a slightly different setup, that is, a single [BMIM][BF_4]-Gold interface. In particular, we calculated two values of the work of adhesion, namely one corresponding to the wall-liquid interface and another corresponding to the wall-solid interface. In the case of the wall-liquid, we used a system of one gold slab in contact with the liquid of 400 pairs of [BMIM][BF_4] with box dimensions $4.055 \times 4.055 \times 50.000\,\mathrm{nm}^3$. NVT runs of 2 ns were performed for 26 points along each coupling parameter axis shown in Figure 4 of this chapter's article on page 29, using the last configuration at one point as the starting configuration at the next point along the coupling parameter axis. Points along a coupling parameter were chosen to be denser near the point $\sqrt{\epsilon_s} = 0\ \sqrt{\mathrm{kJ/mol}}$ where ϵ_s is the Lennard-Jones energy parameter for the solid atoms, for good resolution. For each run, the temperature was kept at 298 K using a velocity rescale thermostat and electrostatics were calculated using PME with correction to slab geometries [148]. Lennard-Jones interactions were calculated using a cut-off of 1.5 nm and a potential shift with Verlet cut-off scheme, with dispersion correction to the energy and pressure as implemented in GROMACS 5.1.4 [157]. The systems were evolved at 0.5 fs timesteps and integrated with the leap-frog algorithm, saving information every 0.5 ps.

To ascertain the result, the same procedure was performed on a system with 3400 molecules of SPC/E water on non-polarisable gold to calculate a reference work of adhesion (blue line in Figure 4(A) of this chapter's article on page 29), which compared well with a similar system reported by Leroy and Müller-Plathe [156].

Calculating the work of adhesion allowed us to estimate the shift in freezing temperature that is due to confinement. In order to estimate the shift in temperature using Equation 2 of this chapter's article, we calculated also the work of adhesion γ_{sw} for the solid-wall interaction. Using the setup from the previous calculation of work of adhesion, we randomised the molecules by raising the temperature from 298 K to 500 K over 1 ns and then annealed to 150 K over 2 ns, after which the temperature was maintained at 150 K for 2 ns. We used then the final configuration to perform the free energy calculations at 150 K, keeping all other parameters the same as for the calculations done at 298 K.

2.2.3 *Layering and local structure*

The local interfacial structure is discussed in detail in the article (page 29). However, this section is to elaborate on a few important topics related to the structure of the RTIL at both the non-polarisable and polarisable gold interfaces.

In Figure 10, the ion number densities and the total mass densities (inset) for systems with polarisable and non-polarisable gold. We observe that from the gold surfaces the liquid retains a strong interfacial structure only to be lost beyond 2 nm from surfaces. The density distribution profiles for the non-polarisable (illustrated in black) and polarisable (illustrated in red) models exhibit remarkable congruence, with the agreement persisting even upon separate examination of cation and anion distributions.

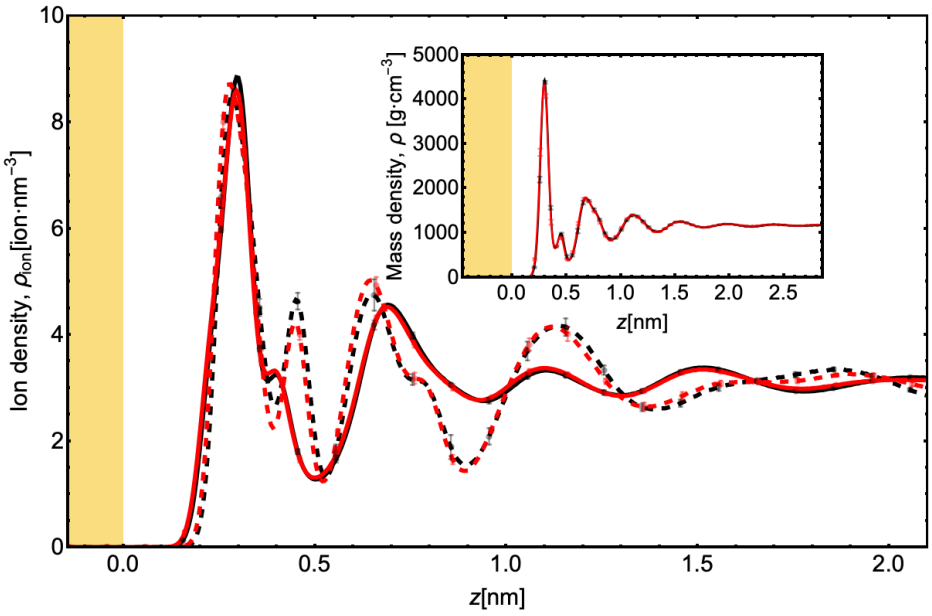

Figure 10: Liquid exhibits strong structure at the interface that extends to about 2 nm from the non-polarisable gold surface (black) and from the polarisable gold surface (red). The inset shows the liquid mass densities where the extent of the liquid interfacial structure is shown much clearly.

In Figure 11, a detailed examination of the ion densities at the interface, as further delineated in Figure 10, reveals that cations—represented by solid lines—tend to adsorb marginally closer to the gold surface, approximately 2.4 Å, compared to anions, which are depicted with dashed lines. This proximity is consistent across both non-polarisable (denoted by black lines) and polarisable (denoted by red lines) models of the gold systems. Owing to their more flat and elongated shape, the cations are able to maximise

van der Waals interactions with the gold surface, resulting in their closer adsorption. In compensation, the anions, due to their relatively higher packing, exhibit an excess which peaks at the interface at approximately 2.8 Å, preceding the cation peak at about 2.95 Å. This nuanced interplay of ionic positioning underscores the structure of the RTIL at the interface.

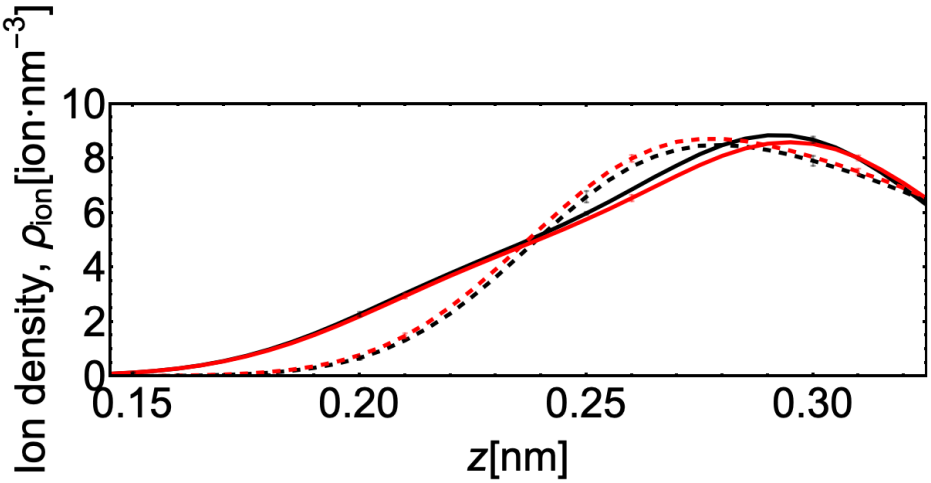

Figure 11: Cations (solid lines) adsorb closer to the gold than anions (dashed lines). The results for the non-polarisable model are reported in black, while those for the polarisable model are reported in red.

In our investigation we also examined the orientation of cations across the interface following the methodology presented by Ferreira et al. [158]. The normalised distributions of cation orientations in the initial adsorption layer on both non-polarisable and polarisable gold surfaces are depicted in Figure 12. Panel (A) illustrates the normalised distribution of angles between the axis traversing the imidazolium ring—from the methyl carbon to the first butyl carbon (blue axis)—and the perpendicular to the gold surface (yellow axis), revealing a predominant orientation where these axes are nearly orthogonal. Panel (B) presents the normalised distribution of angles between the gold surface normal (yellow axis) and the vector extending from the first to the last butyl carbon (blue axis). Panel (C) examines the orientation of the plane of the imidazolium ring (major blue axis, derived from the cross product of the two minor blue axes) relative to the surface normal (yellow axis). Consequently, cations in the foremost adsorbed layer predominantly adhere to the surface with their imidazole rings aligned parallel to the Au(111) surface, as corroborated by Figure 12. This alignment echoes findings from SFB experiments by Perkin et al. [57], which observed the aromatic rings of [EMIM] ions aligning parallel to mica surfaces when [EMIM][$EtSO_4$] was confined between them. Such an alignment is anticipated even in simplified ionic liquid models at neutrally charged electrodes, as demonstrated by Breitsprecher et al. [133, 159], with the likelihood of this orientation intensifying with increasing surface charge. In stark contrast, Figure 13 reveals the absence of a preferred cation orientation beyond the initial layer, with orientations randomising at a distance of approximately 10 Å from the gold surface.

In order to delve deeper into the structure of the RTIL at the gold interfaces, we consider now pair correlation functions at the interface. The pair correlation functions depicted in Figure 14, calculated using the x- and y-coordinates of the centres of mass of the anions, and the imidazolium of cations, reveal pronounced counterion peaks at approximately 0.502 nm radius between ions. This distinct feature gradually diminishes towards the bulk

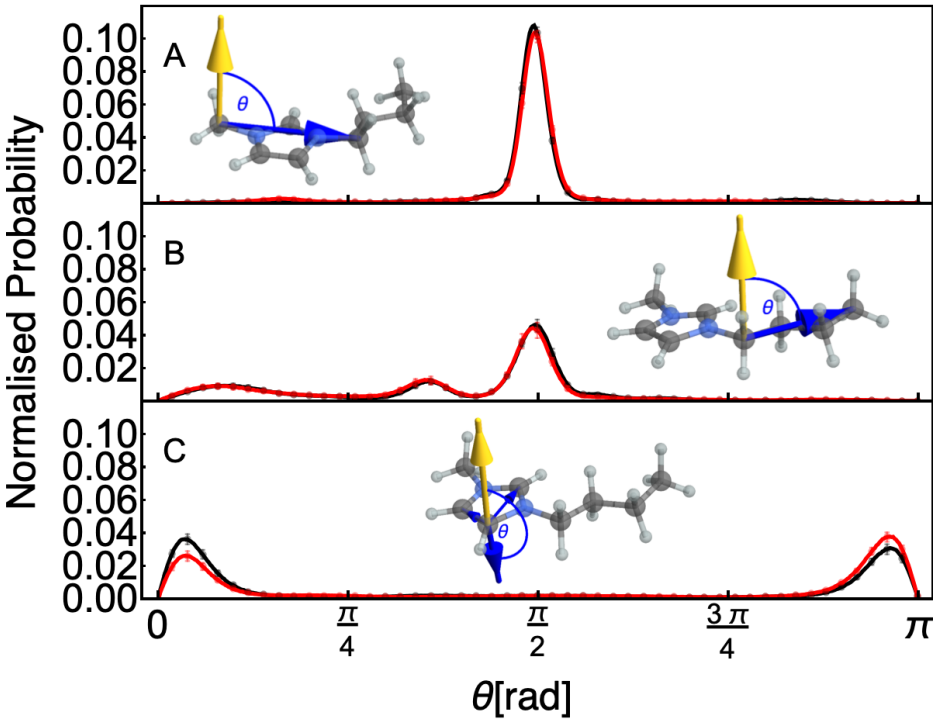

Figure 12: Normalised distribution of orientation of cations in the first adsorption layer. (A) Tilt of the ring head (B) Tilt of the butyl tail (C) Tilt of the plane in which lies the ring.

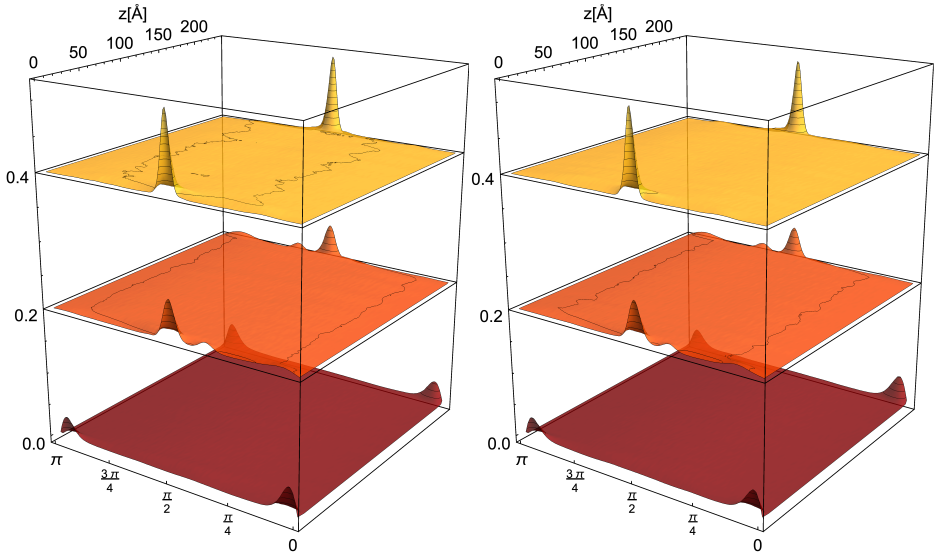

Figure 13: Evolution of cation orientation along the z-axis for non-polarisable (left) and polarisable (right) gold. The distributions have been shifted for clarity. Features of the distribution of angles in Figure 12 only persist within the first 10 Å from the surface.

with bulk structures reemerging beyond 1.9 nm as indicated by the yellowest lines in the figure, corroborating the recovery of bulk density shown by density profiles in Figure 10.

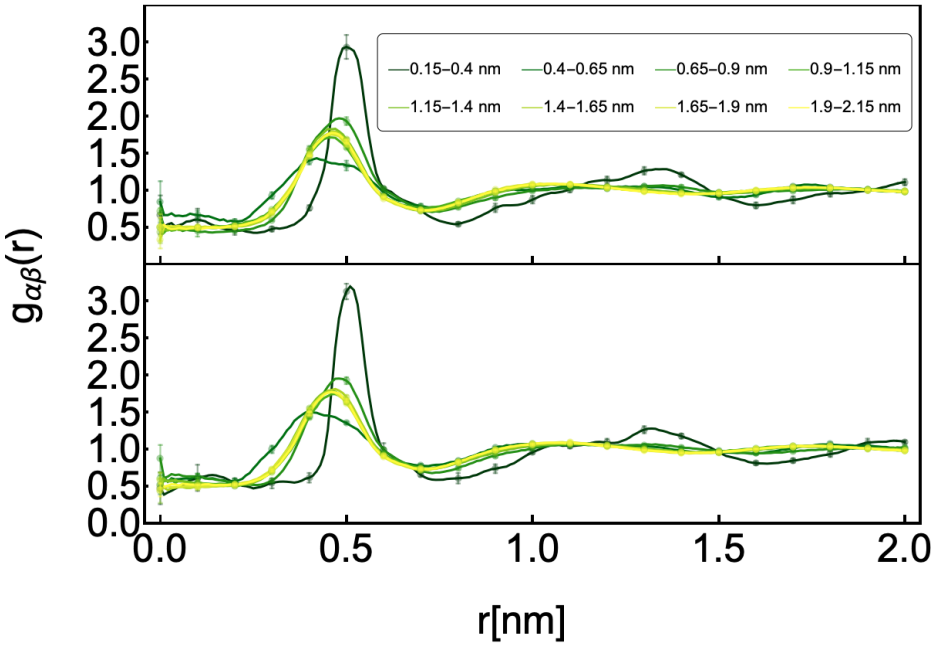

Figure 14: Pair correlation functions of centre of mass of imidazolium of cation and centre of mass of anion, calculated within regions of 0.25 nm width across the interface with non-polarisable (top) and polarisable (bottom) gold. Going from dark green to yellow correspond to going from regions at the interface to regions in bulk, respectively.

To further elucidate the subtle impact of metal polarisation on the stratification of the RTIL, we examined the variations in the charge densities in the liquid across the interface, as expressed by the equation:

$$\rho_{q,j}(n\Delta z) = \sum_{i \in j} q_i \rho_{N,i}(n\Delta z). \tag{24}$$

Here, q_i represents the charge of atoms of type i within a molecule of type j. The adsorption of cation at the surface builds up an excess of positive charge, evidenced by initial peak in the cation charge distribution (Figure 15). In response, the smaller anions, characterised by a higher packing density at the interface, form a subsequent layer that overcompensates the excess charge from the cations. This is then followed by a slightly positively charged layer, beyond which charge fluctuations persist up to 2 nm from the Au(111) surface (Figure 15). Notably, a comparable charge density distribution was observed for [BMIM][PF_6] and [BMIM][TNf_2] by Ferreira et al. [158].

The figure also illustrates the cumulative effect of charge densities of the ions, depicted in solid lines. The inset, however, highlights the electric field, clearly delineating the extent of influence of the interface. It is evident that the fluctuations in the charge density—and consequently the electric field—are significantly influenced by the anions. The positive peak at around 3.5 Å for the anions, surrounded by negative peaks, originate from the positively charged boron within the anion. The two negative peaks that surround this positive peak result from the tetrahedral configuration of fluoride ions around the boron.

2.2.4 *Diffusion coefficient*

The dynamical characteristics of the RTIL were probed by examining the self-diffusion of the ions. The interface was segmented into symmetrised regions, and within each region

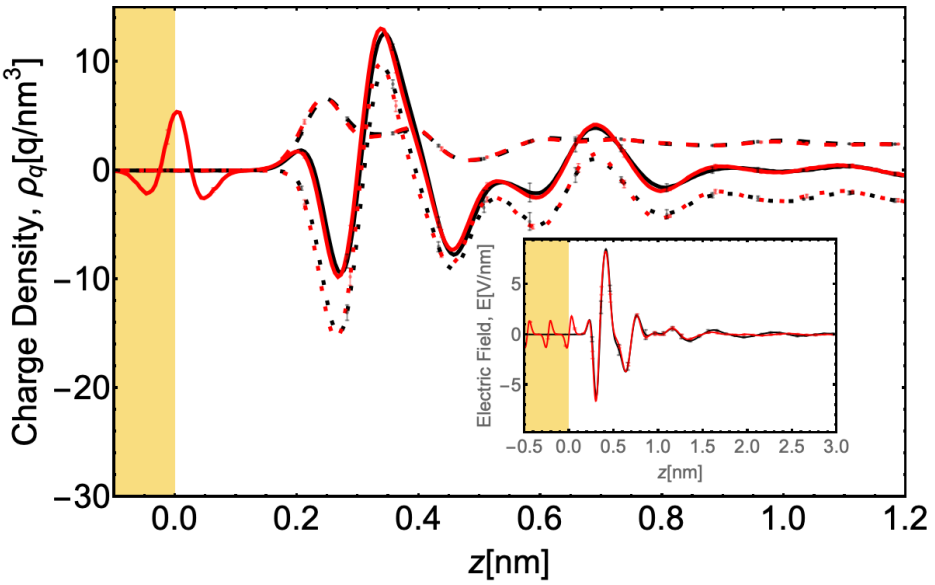

Figure 15: Distribution of charge on non-polarisable gold (black) and polarisable gold (red) surfaces across the interface. Dotted lines are densities for anions, dashed lines, those of cations and continuos lines, their sums. The inset shows the integral of charge distribution, the electric field.

α, the 2-dimensional diffusion coefficient D_α over a duration τ was determined using the Einstein relation:

$$D_\alpha = \frac{1}{4} \lim_{\tau\to\infty} \frac{d}{d\tau} MSD_\alpha(\tau). \tag{25}$$

Here MSD_α denotes the mean squared displacement within region α. For instance, along the x-axis and considering a reference time t, it is defined as:

$$MSD_{x,\alpha}(t,\tau) = \frac{\sum_i \sigma_{i,\alpha}(t)\sigma_{i,\alpha}(t+\tau)(x_i(t+\tau)-x_i(t))^2}{\sum_i \sigma_{i,\alpha}(t)\sigma_{i,\alpha}(t+\tau)} \tag{26}$$

The switching function $\sigma_{i,\alpha}(t)$ indicates the presence ($\sigma_{i,\alpha}(t) = 1$) or absence ($\sigma_{i,\alpha}(t) = 0$) of the ith particle in the region α at time t, and $x_i(t)$ is the coordinate of that ith particle at that time t. By restarting the calculation of $MSD_{x,\alpha}(t,\tau)$ at different reference times,

$$MSD_\alpha(\tau) = \frac{1}{N} \sum_{n=1}^{N} \sum_{j\in\{x,y\}} MSD_{j,\alpha}(n\Delta t, \tau). \tag{27}$$

In this equation, Δt is a restart time—the interval between two successive reference times—and N is the total number of such restarts. For each of the five independent trajectories, excluding the initial 10 ns, the subsequent 40 ns were divided into 16 consecutive parts. The MSD for $\tau = 2.5$ ns was calculated with a 10 ps restart time for each part and then averaged over all 16. The diffusion coefficients for each region were subsequently evaluated according to Equation 25, by calculating the slopes of the MSDs between $\tau = 0.25$ ns and $\tau = 1$ ns, and then averaging over all five trajectories.

In the computation of D_α the size correction [160] was disregarded due to its negligible impact, as demonstrated by the system dimensions $L_\perp = 23.7$ nm and $L_\parallel = 4.055$ nm,

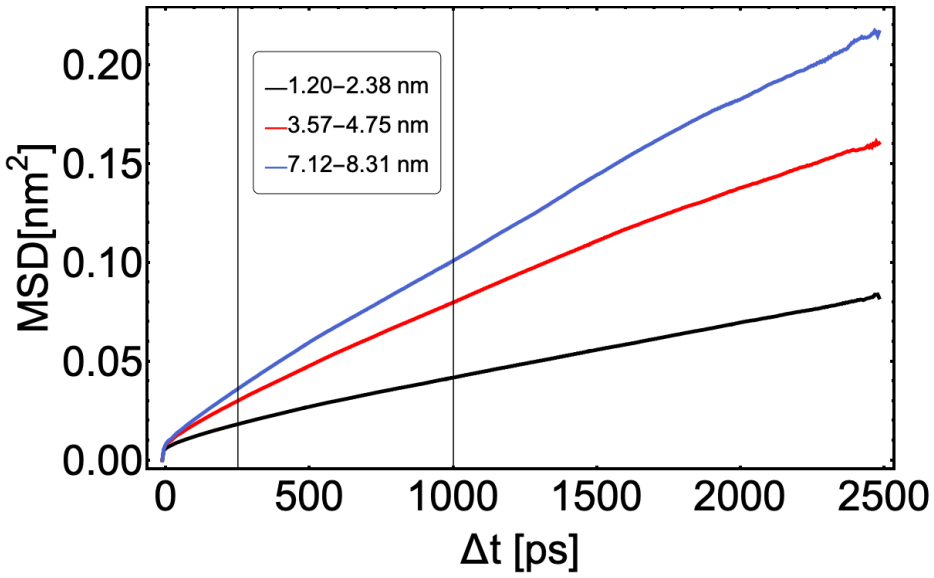

Figure 16: MSD for cations found in three regions. Vertical lines show portions of MSD used in calculation of corresponding D_α.

resulting in $h_{||} \approx 5.046$. With bulk viscosity $\eta \approx 150\,\mathrm{mPa\,s}$ at a temperature of $T = 298\,\mathrm{K}$, the correction to the diffusion coefficient is:

$$\Delta D_{||} = -\frac{k_B T}{6\pi\eta L_{||}} h_{||} \tag{28}$$

$$= -1.811 \times 10^{-12}\,\mathrm{m^2\,s^{-1}} \tag{29}$$

which is insignificant with respect to calculated D_α's. Similarly, for the bulk ionic liquid with isotropic box size $L = 6.355\,\mathrm{nm}$, we find that the correction to the diffusion coefficient [161] is

$$\Delta D_{bulk} = \frac{k_B T}{6\pi\eta L} \xi, \tag{30}$$

$$= 6.5 \times 10^{-13}\,\mathrm{m^2\,s^{-1}} \tag{31}$$

where $\xi, = 2.837$.

Contrary to the observations from structural properties, the interface exerts a more pronounced and extended influence on the dynamics. The diffusion coefficients of both ion species demonstrate a gradual transition to bulk value, underscoring the criticality of selecting an appropriate system size for accurate diffusion coefficient calculations. For instance, Figure 17 illustrates the diffusion coefficients of the cations within systems comprising 400, 800 and 1200 pairs of ions. In each of these three systems the lateral (x, y) dimensions are maintained at $4.055 \times 4.055\,\mathrm{nm^2}$, while the separation between the two gold surfaces along the z-axis is varied. A comparison of the smaller 400-pair system with its large counterparts revealed that the diffusion near the interface is not merely a function of proximity to the surface but is also influenced by the overall system size, as indicated by the varying slopes of the curves at the interface.

When the diffusion coefficients of the ions (in Figure 5 of this chapter's article) are fitted to the exponential function

$$f(z) = k\left(1 - e^{-(z-\zeta)/\lambda}\right), \tag{32}$$

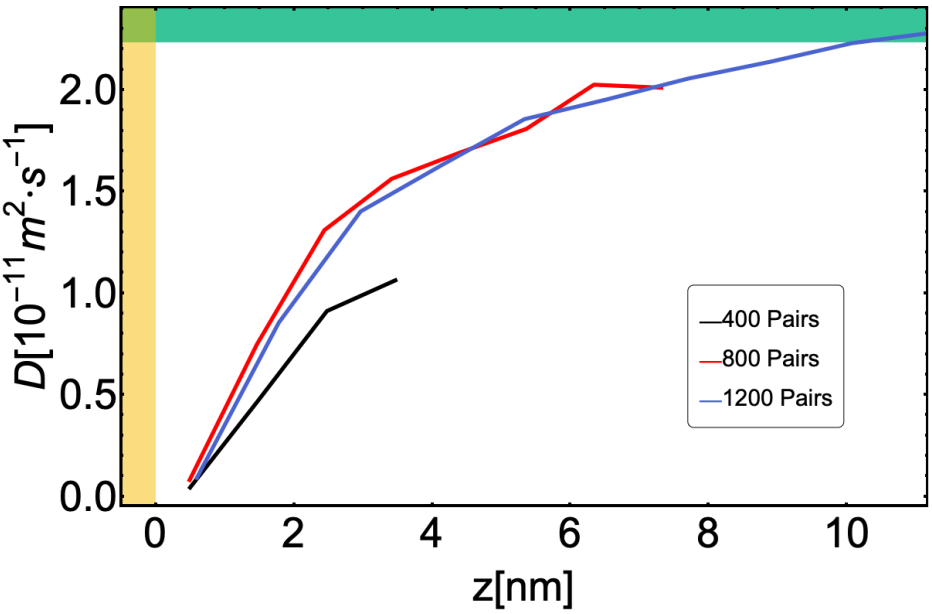

Figure 17: Effect of system size on the self-diffusion of cations. One recovers the bulk value for the largest system (1200 pairs. The bulk value for the diffusion coefficient, calculated from the simulations, is reported as green strip, along with the error bar.

Table 2: Table of exponential fit parameters.

	ζ/nm	$k/10^{-11}$ m^2 s^{-1}	λ/nm
		BMIM	
Non-polarisable gold	0.45	2.28	2.9
Polarisable gold	0.45	2.56	3.6
		BF_4	
Non-polarisable gold	0.52	1.68	3.5
Polarisable gold	0.51	1.90	4.5

they give the characteristic lengths λ shown in Table 2. Figure 18 shows the exponential fit curves (shown in thin lines) to the self-diffusion of ions across the interface in the system with non-polarisable gold (illustrated in black lines) and polarisable gold (illustrated in red lines) surfaces.

2.3 OBJECTIVES

The primary objective of this study was to investigate the role of image charges in the behaviour of [BMIM][BF_4] confined between gold electrodes in equilibrium conditions. We aimed to:

- CHARACTERISE THE STRUCTURAL PROPERTIES: Determine how image charges influence the layering and lateral organisation of ions at the interface.

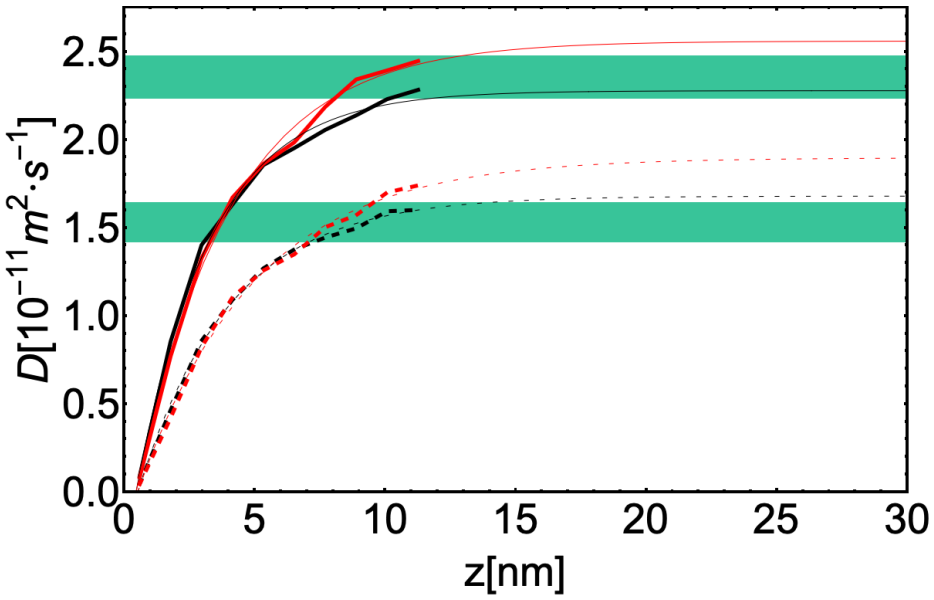

Figure 18: Exponential fit to the self-diffusion of ions in systems with non-polarisable gold (black) and polarisable gold (red) surfaces. Thin lines correspond to the fitted curves while thick lines correspond to the data. Dashed lines correspond to anions while those of cations are continuos lines.

- EVALUATE THERMODYNAMIC PROPERTIES: Assess the impact of image charges on interfacial free energy and phase behaviour, particularly with respect the "capillary freezing" transition.
- ANALYSE DYNAMICAL PROPERTIES: Explore how image charges affect the diffusion coefficients and overall dynamics of the IL in confined spaces.

2.4 KEY FINDINGS AND CONTRIBUTIONS

2.4.1 *Structural Properties*

The study reveals that the presence of an interface induces strong layering in the confined IL, consistent with previous observations [103, 57, 49, 108, 109]. The total mass density profile indicates that this layering extends up to 2 nm from the surface, with minimal effect from metal polarisation. Density maps of the first adsorbed layer show that cations adsorb onto the surface, creating vacant spots for anions, resulting in a defective hexagonal arrangement similar to that observed for [BMIM][PF_6] on graphite [162]. The potential profile across the interface shows oscillations corresponding to the layered structure of the ions. The PZC indicates that there is a charge imbalance at the interface even at equilibrium. However, the PZC is only slightly affected by image charges.

2.4.2 *Thermodynamic Properties*

The work of adhesion, which measures the free energy required to separate the liquid from the solid surface, calculated for both non-polarisable and polarisable gold models, indicates that image charges contribute minimally to the total adhesion energy. This finding aligns with the observation that the dielectric response of [BMIM][BF_4] significantly

screens electrostatic interactions, reducing the impact of image charges. The freezing temperature of the IL, although raised by approximately 26.6 K, remains well below room temperature.

2.4.3 *Dynamical Properties*

The diffusion coefficients for cations and anions increase with distance from the surface, approaching bulk values at around 10 nm. This extended influence of the interface on dynamics contrasts with the structural properties, suggesting that while the static structure is confined to a narrow region at the interface, dynamic effects persist over longer range. The exponential approach of the diffusion coefficient to bulk value implies a significant impact of confinement on viscosity, which is crucial for applications involving flow and transport of ILs in confined geometries.

2.5 CONCLUSIONS TO THE STUDY

Our study provides a comprehensive analysis of the role of image charges in the behaviour of ILs confined between metallic interfaces. The findings underscore the complex interplay between structure, thermodynamics, and dynamics in these systems, offering valuable insights for the design and optimisation of IL-based applications. The minimal impact of image charges on structural and thermodynamic properties, contrasted with their significant effect on dynamics, highlights the need for a nuanced understanding of IL behaviour in confined environments. This work sets the stage for future studies exploring the intricate mechanisms governing ILs at interfaces and their implications for practical applications.

PCCP

ROYAL SOCIETY OF CHEMISTRY

PAPER

View Article Online
View Journal | View Issue

Cite this: *Phys. Chem. Chem. Phys.*, 2020, **22**, 10786

Role of image charges in ionic liquid confined between metallic interfaces†

Samuel Ntim and Marialore Sulpizi *

Received 24th January 2020,
Accepted 19th March 2020

DOI: 10.1039/d0cp00409j

rsc.li/pccp

The peculiar properties of ionic liquids in confinement have not only become essential for energy storage, catalysis and tribology, but still pose fundamental questions. Recently, an anomalous liquid–solid phase transition has been observed in atomic force microscopy experiments for 1-butyl-3-methylimidazolium tetrafluoroborate ([BMIM][BF_4]), the transition being more pronounced for metallic surfaces. Image charges have been suggested as the key element driving the anomalous freezing. Using atomistic molecular dynamics simulations, we investigate the impact of image charges on structure, dynamics and thermodynamics of [BMIM][BF_4] confined between gold electrodes. Our results not only unveil a minor role played by the metal polarisation, but also provide a novel description of the interfacial layer. Although no diffuse layer can be defined in terms of the electrostatic potential, long range effects are clearly visible in the dynamical properties up to 10 nanometers away from the surface, and are expected to influence viscous forces in the experiments.

1 Introduction

Since the nineties room temperature ionic liquids (RTILs) have attracted constant interest from both the fundamental point of view as models for concentrated electrolytes, as well as for their applications. In particular the structure of RTILs in confinement has raised interest for its critical role in energy storage and transformation in supercapacitors,[1,2] actuators,[3,4] batteries,[5–7] and solar cells.[8] The presence of an interface with a solid surface modifies the liquid properties producing a layered structure, whose extent strongly depends on the liquid composition as well as on the nature and structure of the surface.[9] The presence of layers for several types of surfaces has been observed both in experiments, including X-ray reflectivity,[10] Atomic Force Microscope (AFM)[11,12] and Surface Force Balance (SFB),[13–15] as well as in simulations.[16] On the other hand, the presence of a diffuse layer, in analogy to what is found in dilute electrolytes, is still a debated issue in the community.[17–27] Therefore the detailed characterisation of the interfacial layer is still far from being clear and unanimous.

Additionally, due to the dominant role of electrostatic forces, one may anticipate that the metallic nature of the confining surfaces should affect the static and dynamic properties of confined RTILs. Such a relationship has been recently explored using tuning-fork-based atomic force microscope nanorheological experiments.[23] These revealed a dramatic change of the RTIL towards a solid-like phase below a threshold thickness related to the metallic nature of the confining materials, with more metallic surfaces facilitating capillary freezing. Siria and coworkers also proposed a simple explanation of the observed phenomena in terms of image charges.[23] The simple idea highlighted in ref. 23 is that if one considered a semi-infinite ionic crystal at the interface with a perfect metal, the network of image charges would build a crystal structure with an almost perfect symmetry with respect to the real half-lattice. Accordingly, one would expect the electrostatic contribution to the surface free energy to nearly vanish, as the system behaves as a single bulk lattice. In real systems further complications arise from the shape of the ions and their relative size. Moreover, as recently pointed out by Lhemerout and Perkin[26] in the SFB experiments it is difficult to separate the electrostatic and the viscous contributions to the measured forces. Ionic liquids may have dynamic viscosity even 100 times greater than that of water (as *e.g.* in the case of 1-butyl-3-methylimidazolium cation ($[BMIM]^+$) and tetrafluoroborate anion ($[BF_4]^-$) ([BMIM][BF_4]), and consequently may exhibit viscous forces of the same order of magnitude as the reported electrostatic forces at the approach velocities typically employed in experiments.

Our aim here is to investigate the role of the image charges by performing atomistic molecular dynamics simulations of ionic liquid in confinement. We consider simple equilibrium conditions in the absence of viscous forces. We choose the $[BF_4]^-$ [BMIM][BF_4]) system (as in ref. 23) confined between two Au(111) surfaces. To include the image charge effects we use the method which we have recently developed and which permits to describe

Institut für Physik, Johannes Gutenberg Universität, Staudingerweg 7, 55128-Mainz, Germany. E-mail: sulpizi@uni-mainz.de

† Electronic supplementary information (ESI) available. See DOI: 10.1039/d0cp00409j

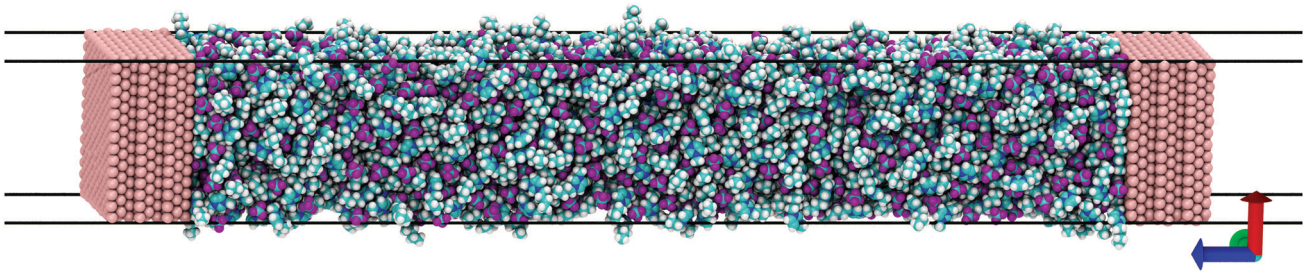

Fig. 1 Typical simulation box of 1200 pairs of [BMIM][BF_4] confined in non-polarisable gold. Gold atoms are replaced with polarisable gold "molecules" for simulations with polarisable gold.

the metal polarisation in a consistent way without additional computational costs.[28] Alternatively, a fixed potential approach could also be used[29] or the Electrostatic Layer Correction with Image Charges (ELCIC).[30] A snapshot of our model system is reported in Fig. 1. We analyse structural, energetic and dynamical properties of the RTIL/gold interfaces with and without image charges. In particular, we aim to address the role of image charges on the extent of the interfacial layering of the RTIL, to quantify the influence of image charges on the interfacial free energy and finally to investigate the influence of image charges on dynamical properties, such *e.g.* the diffusion coefficients.

2 Results and discussion

As already well established, the presence of an interface induces a strong layering in the confined RTIL.[9,13,16,32,33] This is also confirmed in our simulations and shown by the total mass density profile reported in the inset of Fig. S2 (ESI†) where the layering is observed to extend for about 2 nm from the surface. Interestingly the density profile is not affected by the metal polarisation effects. Further analysis of the first adsorbed layer, as provided by the density maps presented in Fig. 2, reveals that the cations adsorb onto the surface, leaving vacant spots to be occupied by the anions. This lateral organisation shows a defective hexagonal arrangement of the anions. A similar ions distribution has been reported for [BMIM][PF_6] on graphite[34] where the lattice spacing in the adsorbed ions was about 4 times that of carbons in the graphite surface. The metal polarisation does not cause any significant change in the cation orientation in the first adsorbed layer (see ESI†). Our picture of flat-lying imidazolium ions, separated by anions, which are only slightly above the cations plane is in agreement with experimental studies, where the orientation of imidazolium-based ionic liquids on Au(111) and Ni(111) has been probed by angle-resolved X-ray photoelectron spectroscopy (ARXPS),[35,36] on glass studied with X-ray photoelectron spectroscopy[37] and on Pt with sum frequency generation (Fig. 3).[38]

The organisation of the ions, creating variable local charge densities at the interface, in turn generate an electric field and hence a potential drop at the interface, according to Poisson's equation

$$\Phi = \Phi(\zeta) - \frac{1}{\varepsilon_0}\int_{\zeta}^{z} dz' \int_{-\infty}^{z'} dz'' \rho_q(z'') \quad (1)$$

where ζ is a reference in the left gold slab whose potential is $\Phi(\zeta)$ and $\rho_q(z)$ is the charge density. The potential profile shows an oscillating behaviour; a first positive peak corresponds to the closer adsorption of the cations, and it is followed by a negative peak, due to the anions layer. Due to their smaller size the anions can crowd in the second layer and overscreen the positive charge in the first layer. The fluctuation persist up to a few nanometers away from the gold surface. The potential of zero charge (PZC), defined here as the Poisson potential difference between the electrode and the bulk liquid, is 0.3 V and

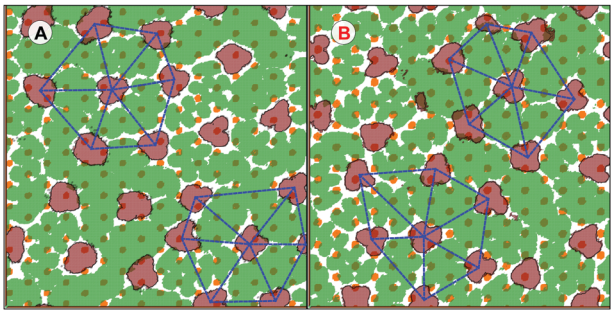

Fig. 2 Density map of adsorbed ions on (A) non-polarisable gold surface and (B) polarisable surface. Yellow dots represent the first layer of gold atoms, the green map corresponds to the cation while the brown map corresponds to the anion. The blue dashed lines are to emphasise the defective hexagonal arrangement of the anions.

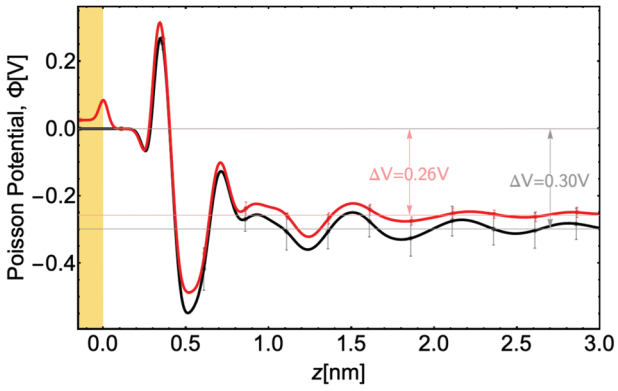

Fig. 3 Potential drop in liquid on non-polarisable gold surface (black) and on polarisable gold surface (red).

0.26 V for non-polarisable and polarisable gold electrodes respectively. A similar value was found for an Au(100)/[BMIM][PF_6] system (PZC $\approx$ 0.48).[39] Overall, the gold polarisation at the interface seem to have a negligible effect. The addition of the image charges only slightly reduce the ion unbalance at the interface, therefore reducing the overall potential by only about 13%.

At this point one may wonder why only such minor effects on the structure of the interfacial layer arise from the explicit introduction of the image charge effects. The reason may reside in the fact that locally the ion charges are screened by the surrounding counterions. Our analysis suggests that image charge effects are actually not so important as in vacuum, in analogy with the aqueous systems, which we have previously investigated,[28] and where charges coming from solvated ions or from charged groups in solvated biomolecules are strongly screened by the water dielectric response. The static dielectric constant of [BMIM][BF_4], which is 13.9 at 298 K,[40] ($\sim$1/6 of that of water), it is still large enough to reduce the electrostatic interactions by more than a factor of 10.

As next we would like to quantify and discuss the impact of the image charges on the local thermodynamic properties, namely on the interfacial free energy. We have calculated the work of adhesion, that is, the work needed to separate the liquid layer from the solid support, in both the non-polarisable and polarisable models The Lennard-Jones contribution to the work of adhesion, reported in Fig. 4(A) as function of the coupling parameter, is qualitatively similar to that obtained for other systems.[31,41,42] However, the work of adhesion for the ionic liquid, $W_{sl,LJ}$ = 485.9 mJ m^{-2}, is much higher than that of water calculated on the same surface. This is not surprising, considering that RTILs have a much lower surface tension with respect *e.g.* to that of water, which corresponds to a higher wettability of the gold surface and to a stronger solid/liquid interaction. We now turn to the evaluation of the purely electrostatic contribution to the work of adhesion, which only results from the inclusion of the image charges We remind here that, at the PZC, in the absence of metal polarisation, there is no net charge on the gold and therefore no electrostatic interaction between the liquid and the surface. The Coulomb contribution to the work of adhesion $W_{sl,Coul}$ = 9.9 mJ m^{-2} is about 2% of the total. This is at difference with the silica/water interface discussed by Surblys *et al.*,[42] where the Coulomb contribution accounts for about 15% of the total work of adhesion, as result of to hydrogen bonds between water molecules and surface silanols.

In order to appreciate the impact of the image charge contribution to the interfacial free energy on the macroscopic properties, we calculate the change induced on the freezing temperature at the interface. According to the Gibbs–Thomson equation for the shift in freezing temperature due to confinement, ΔT is given by[43]

$$\Delta T = T_{\text{confined}} - T_{\text{bulk}} = \frac{2T_{\text{bulk}}\Delta\gamma}{\rho L_h \lambda_{\text{width}}} \quad (2)$$

where T_{bulk} = 202 K is the freezing temperature of bulk

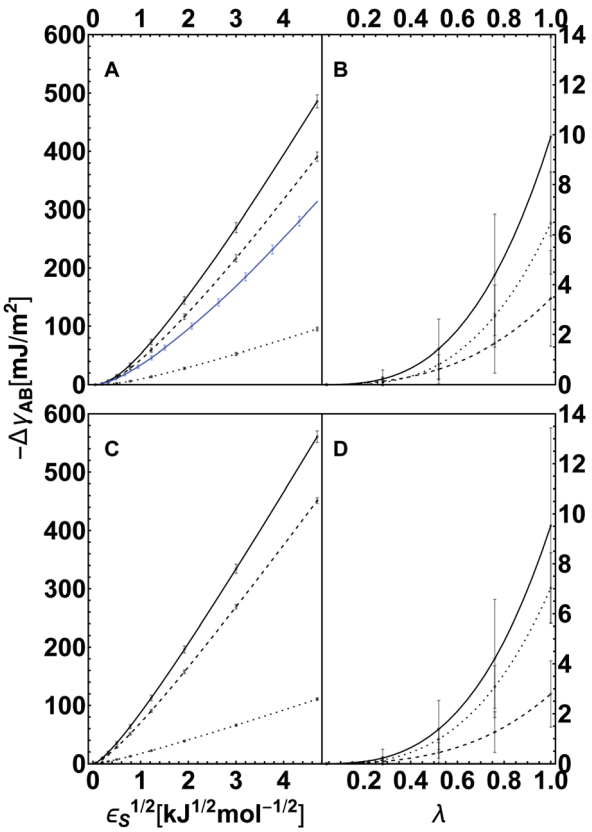

Fig. 4 Work of adhesion due to (A) Lennard-Jones gold–ionic liquid interactions and (B) electrostatic gold–ionic liquid interactions. Continuous black curves are the sums of their corresponding dashed (BMIM) and dotted (BF_4) curves. For sake of comparison, the blue curve in (A) represents the work of adhesion for the (non-polarisable) gold–SPC/E water interface and is very close to that reported in ref. 31 (C) and (D) are works of adhesion due to Lennard-Jones and electrostatic interactions respectively but at 150 K.

[BMIM][BF_4], ρ = 1211 kg m^{-3} its bulk density, L_h = 4.69 K kg^{-1} its latent heat of fusion and $\Delta\gamma = \gamma_{lw} - \gamma_{sw}$ is the difference in the liquid-wall and solid-wall interfacial free energies. The γ_{lw} has been discussed already, while the γ_{sw} requires an additional calculation for the wall(gold)–solid(ionic liquid) interface. To this purpose we have generated two wall-solid interfaces freezing two independent configurations at temperature T = 150 K. For these two interfaces we have calculated, with the same dry surface approach the interface free energies, obtaining an average value of γ_{sw} = $-$560.71 mJ m^{-2}. Interestingly the image charge contribution for γ_{sw} is very close to that found for γ_{lw}. For a confinement width of λ_{width} = 20 nm, the freezing temperature raises by $\Delta T \approx$ 26.6 K, which brings the bulk freezing temperature of 202.15 K to 228.75 K, still quite far from room temperature. Clearly λ_{width} at the denominator implies that the freezing temperature may raise to room value as the confinement width is reduced to 5 nm. Although the effect of confinement is quite important, the net contribution due to the image charge is actually negligible. This is essentially due to the fact that the solid [BMIM][BF_4] is actually amorphous, with a structure close to that of the interfacial liquid.

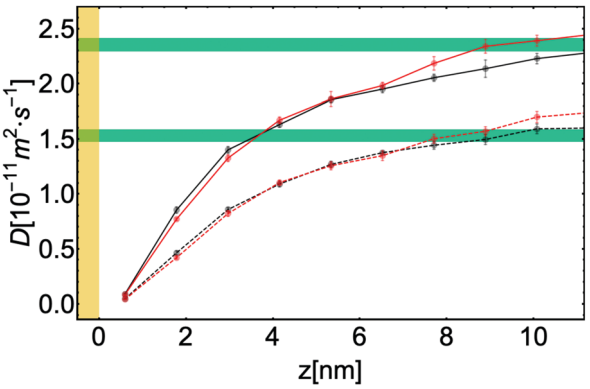

Fig. 5 Diffusion coefficient of the ions, across the interface. For each trajectory, we divided the symmetrised region between the gold slabs into ten regions and calculated the 2-dimensional diffusion coefficient in the plane of the gold surface (x–y plane) every 2.5 ns for 25 ns and averaged. Solid lines represent cation diffusion coefficient while dashed lines represent anion diffusion coefficient. Green strips indicate the bulk values (2.26×10^{-11} m^2 s^{-1} for the cations and 1.44×10^{-11} m^2 s^{-1} for the anions, respectively) with the corresponding error bars.

Having investigated, so far, the image charge effects on the structural as well as thermodynamical properties, a natural question arises on what is the impact of the image charges on transport and dynamical properties. We calculate here the translational self-diffusion of the two ionic components in the plane parallel to the surface (Fig. 5) The size corrections[44] for the diffusion coefficients are, for the considered sizes, negligible (see ESI† for a detailed discussion). The bulk diffusion coefficient of the ions, calculated from five independent trajectories of 800 ionpairs at 298 K and including the size correction[45] is also reported, including the statistical uncertainty as a green stripe.

The cations diffuse much faster than the anions, with values monotonically increasing to the bulk value (Fig. 5). From analysis of the structure, the interface only extends to about 2 nm from the gold surface. However, the dynamics shows that the interface extends about five times more, with the diffusion coefficient reaching bulk value only at 10 nm away from the gold surface. In particular the diffusion coefficient (Fig. 5) reaches the bulk value according to an exponential law with a characteristic lengths λ between 2.9 nm and 4.5 nm (see Table S1 and Fig. S10, ESI†). Interestingly this also implies an exponential dependence of the viscosity as function of the distance from the surface, which in turn would affect the viscous forces if non-equilibrium conditions are considered. Following the approach of Chan and Horn[46] and recently used by Perkin[26] to disentangle electrostatic and viscous contributions, the viscous contribution can be described with the Reynold formula:

$$F(t) = -\frac{6\pi\eta R^2 \dot{D}}{D - b} \quad (3)$$

where D is the distance between the solid surface in the SFB, η is the viscosity and b is the slip length. In their analysis of the experimental data the viscosity has been assumed as constant and a negative slip length has been introduced to take into account of the "frozen" interfacial layer.[26] From our simulations an interesting picture emerges where a "diffuse" layer may be defined not in terms of electrostatic, but instead of dynamical properties, as the region across which the liquid viscosity recovers its bulk value. Also for the self-diffusion of the ions, within the error bars, the non-polarisable and the polarisable gold models provide the same results. This last result suggests that viscous forces would be independent of the metallicity, at least under the investigated conditions, namely at the PZC.

3 Experimental section

Our system contains 1200 pairs of [BMIM][BF$_4$], confined between two gold slabs (electrodes) made each of 9 layers of gold atoms in the (111) crystallographic plane and spanning the 4.05457×4.05457 nm^2 cross-section of the box. Outside the electrodes a vacuum region of 222 nm is added. 2D periodic boundary conditions are enforced along the x and y directions, while the interaction between images along the z-directions are decoupled using the particle mesh Ewald with slab correction.[47] Two models for the gold were considered, a non-polarisable gold model[48] and a polarisable one,[28] which includes the induced image charges. To describe the ionic liquid, we use a non-polarisable model of [BMIM][BF$_4$] with force field parameters that reproduce experimental heat of vapourisation, diffusion coefficient, ionic conductivity and shear viscosity of [BMIM][BF$_4$].[49] In order to ensure a statistically relevant sampling five independent initial configurations were sampled from an equilibration run of 20 ns at a constant temperature of 298 K using a Nosé–Hoover thermostat, and at a constant pressure of 1 bar using a semi-isotropic Berendsen barostat. *NVT* production runs were performed on each of the five sampled configurations for 50 ns with a timestep of 0.5 fs and using a velocity rescale thermostat at 298 K, collecting system information every 0.5 ps. Fig. 1 shows a typical simulation system. Calculations of works of adhesion used the dry-surface approach (details in ESI†).[31,42] All simulations were performed with version 5.1.4 of the GROMACS simulation package.[50]

4 Conclusions

We have reported here a systematic analysis of the impact of the image charges on the structural, thermodynamical and dynamical properties of [BMIM][BF$_4$] confined between two Au(111) gold electrodes, using atomistic molecular dynamics simulations. Cations are overscreened by the subsequent layer of anions, forming the double layer. Charge oscillations persist up to a couple of nanometers away from the surface, although a preferential orientation of the cations only affect the very first adsorbed layer. From the structural point of view, at the PZC, the interfacial region is only 2 nanometers thick. On the other hand, from the dynamical point of view, we notice that the ions dynamics at the interface is considerably slowed down and bulk

diffusion is only recovered after 10 nm away from the gold surface.

Contrary to the somewhat intuitive expectations the image charges do not play any appreciable role on the structure and the dynamics. This is due to the strong electrostatic screening which takes place at the interface with the metal surface. Calculations of works of adhesion have shown that the impact of the classical image charge potential on the shift of the freezing temperature at the interface is negligible, which suggests that the cause of the increased capillary freezing observed in the work of ref. 23 must be sought somewhere else. Enhanced freezing at the interface may be due to more complex effects, including the charging of the tip, and out of the equilibrium conditions due to the squeezing of the liquid between the substrate and the tip. Further complications may arise from the nanostructuration of the metal surface, due *e.g.* to defects and reconstruction. It has been shown that separation of ions in nanoporous media can locally enhance the electrostatic effects,[51] also including image charge effects. More work is therefore required in order to include these further aspects into the modelling and to bring the simulations closer to the complex experimental conditions.

Conflicts of interest

There are no conflicts to declare.

Acknowledgements

We are grateful to Benjamin Rotenberg and Mathieu Salanne for useful discussions. Parts of this research were conducted using the supercomputer Mogon and/or advisory services offered by Johannes Gutenberg University Mainz (hpc.uni-mainz.de). This project has received funding from the European Union's Horizon 2020 research and innovation programme under grant agreement no. 674979-NANOTRANS and from the Deutsche Forschungsgemeinschaft under the TRR146 project.

References

1 A. Lewandowski and M. Galinski, *J. Power Sources*, 2007, **173**, 822–828.
2 H. Kurig, M. Vestli, K. TÃnurist, A. JÃnes and E. Lust, *J. Electrochem. Soc.*, 2012, **159**, A944–A951.
3 T. Torimoto, T. Tsuda, K.-I. Okazaki and S. Kuwabata, *Adv. Mater.*, 2010, **22**, 1196–1221.
4 J. Torop, M. Arulepp, T. Sugino, K. Asaka, A. Janes, E. Lust and A. Aabloo, *Langmuir*, 2014, **30**, 2583–2587.
5 D. Piper, T. Evans, K. Leung, T. Watkins, J. Olson, S. Kim, S. Han, V. Bhat, K. Oh, D. Buttry and S. Lee, *Nat. Commun.*, 2015, **6**, 6230.
6 D. R. MacFarlane, N. Tachikawa, M. Forsyth, J. M. Pringle, P. C. Howlett, G. D. Elliott, J. H. Davis, M. Watanabe, P. Simon and C. A. Angell, *Energy Environ. Sci.*, 2013, **7**, 232–250.
7 J. L. Schaefer, Y. Lu, S. S. Moganty, P. Agarwal, N. Jayaprakash and L. A. Archer, *Appl. Nanosci.*, 2012, **2**, 91–109.
8 B. Li, L. Wang, B. Kang, P. Wang and Y. Qiu, *Sol. Energy Mater. Sol. Cells*, 2006, **90**, 549–573.
9 R. Hayes, G. G. Warr and R. Atkin, *Chem. Rev.*, 2015, **115**, 6357–6426.
10 M. Mezger, H. Schröder, H. Reichert, S. Schramm, J. S. Okasinski, S. Schöder, V. Honkimäki, M. Deutsch, B. M. Ocko, J. Ralston, M. Rohwerder, M. Stratmann and H. Dosch, *Science*, 2008, **322**, 424–428.
11 R. Hayes, G. G. Warr and R. Atkin, *Phys. Chem. Chem. Phys.*, 2010, **12**, 1709–1723.
12 X. Zhang, Y.-X. Zhong, J.-W. Yan, Y.-Z. Su, M. Zhang and B.-W. Mao, *Chem. Commun.*, 2012, **48**, 582–584.
13 S. Perkin, T. Albrecht and J. Klein, *Phys. Chem. Chem. Phys.*, 2010, **12**, 1243–1247.
14 S. Perkin, *Phys. Chem. Chem. Phys.*, 2012, **14**, 5052–5062.
15 B. Zappone, W. Zheng and S. Perkin, *Rev. Sci. Instrum.*, 2018, **89**(8), 85112.
16 M. V. Fedorov and A. A. Kornyshev, *Chem. Rev.*, 2014, **114**, 2978–3036.
17 M. A. Gebbie, M. Valtiner, X. Banquy, E. T. Fox, W. A. Henderson and J. N. Israelachvili, *Proc. Natl. Acad. Sci. U. S. A.*, 2013, **110**, 9674–9679.
18 S. Perkin, M. Salanne, P. Madden and R. Lynden-Bell, *Proc. Natl. Acad. Sci. U. S. A.*, 2013, **110**, E4121.
19 M. A. Gebbie, M. Valtiner, X. Banquy, W. A. Henderson and J. N. Israelachvili, *Proc. Natl. Acad. Sci. U. S. A.*, 2013, **110**, E4122.
20 A. A. Lee, D. Vella, S. Perkin and A. Goriely, *J. Phys. Chem. Lett.*, 2015, **6**, 159–163.
21 M. A. Gebbie, H. A. Dobbs, M. Valtiner and J. N. Israelachvili, *Proc. Natl. Acad. Sci. U. S. A.*, 2015, **112**, 7432–7437.
22 N. Hjalmarsson, R. Atkin and M. W. Rutland, *Chem. Commun.*, 2017, **53**, 647–650.
23 J. Comtet, A. Niguès, V. Kaiser, B. Coasne, L. Bocquet and A. Siria, *Nat. Mater.*, 2017, **16**, 634–639.
24 M. A. Gebbie, A. M. Smith, H. A. Dobbs, A. A. Lee, G. G. Warr, X. Banquy, M. Valtiner, M. W. Rutland, J. N. Israelachvili, S. Perkin and R. Atkin, *Chem. Commun.*, 2017, **53**, 1214–1224.
25 A. A. Lee, C. S. Perez-Martinez, A. M. Smith and S. Perkin, *Faraday Discuss.*, 2017, **199**, 239–259.
26 R. Lhermerout and S. Perkin, *Phys. Rev. Fluids*, 2018, **3**, 014201.
27 G. Feng, M. Chen, S. Bi, Z. A. H. Goodwin, E. B. Postnikov, M. Urbakh and A. A. Kornyshev, 2018, arXiv e-prints, arXiv:1805.00697.
28 I. L. Geada, H. Ramezani-Dakhel, T. Jamil, M. Sulpizi and H. Heinz, *Nat. Commun.*, 2018, **9**, 716.
29 C. Merlet, B. Rotenberg, P. A. Madden and M. Salanne, *Phys. Chem. Chem. Phys.*, 2013, **15**, 15781.
30 K. Breitsprecher, P. Košovan and C. Holm, *J. Phys.: Condens. Matter*, 2014, **26**, 284114.
31 F. Leroy and F. Muller-Plathe, *Langmuir*, 2015, **31**, 8335–8345.

32 R. Hayes, N. Borisenko, M. K. Tam, P. C. Howlett, F. Endres and R. Atkin, *J. Phys. Chem. C*, 2011, **115**, 6855–6863.
33 S. Mossa, *Phys. Rev. X*, 2018, **8**, 031062.
34 S. A. Kislenko, I. S. Samoylov and R. H. Amirov, *Phys. Chem. Chem. Phys.*, 2009, **11**, 5584.
35 T. Cremer, M. Stark, A. Deyko, H.-P. Steinruck and F. Maier, *Langmuir*, 2011, **27**, 3662–3671.
36 T. Cremer, L. Wibmer, S. K. Calderón, A. Deyko, F. Maier and H.-P. Steinrück, *Phys. Chem. Chem. Phys.*, 2012, **14**, 5153.
37 T. Cremer, M. Killian, J. M. Gottfried, N. Paape, P. Wasserscheid, F. Maier and H.-P. Steinrück, *ChemPhysChem*, 2008, **9**, 2185–2190.
38 S. Baldelli, *Acc. Chem. Res.*, 2008, **41**, 421–431.
39 E. S. C. Ferreira, C. M. Pereira, M. N. D. S. Cordeiro and D. J. V. A. dos Santos, *J. Phys. Chem. B*, 2015, **119**, 9883–9892.
40 M.-M. Huang, Y. Jiang, P. Sasisanker, G. W. Driver and H. Weingartner, *J. Chem. Eng. Data*, 2011, **56**, 1494–1499.
41 V. R. Ardham and F. Leroy, *J. Chem. Phys.*, 2017, **147**, 074702.
42 D. Surblys, F. Leroy, Y. Yamaguchi and F. Müller-Plathe, *J. Chem. Phys.*, 2018, **148**, 134707.
43 C. Alba-Simionesco, B. Coasne, G. Dosseh, G. Dudziak, K. Gubbins, R. Radhakrishnan and M. Sliwinska-Bartkowiak, *J. Phys.: Condens. Matter*, 2006, **18**, R15.
44 P. Simonnin, B. Noetinger, C. Nieto-Draghi, V. Marry and B. Rotenberg, *J. Chem. Theory Comput.*, 2017, **13**, 2881–2889.
45 I.-C. Yeh and G. Hummer, *J. Phys. Chem. B*, 2004, **108**, 15873–15879.
46 D. Y. C. Chan and R. G. Horn, *J. Chem. Phys.*, 1985, **83**, 5311–5324.
47 I.-C. Yeh and M. L. Berkowitz, *J. Chem. Phys.*, 1999, **111**, 3155–3162.
48 H. Heinz, R. Vaia, B. Farmer and R. Naik, *J. Phys. Chem. C*, 2008, **112**, 17281–17290.
49 V. V. Chaban, I. V. Voroshylova and O. N. Kalugin, *Phys. Chem. Chem. Phys.*, 2011, **13**, 7910–7920.
50 D. V. D. Spoel, E. Lindahl, B. Hess, G. Groenhof, A. E. Mark and H. J. C. Berendsen, *J. Comput. Chem.*, 2005, **26**, 1701–1718.
51 M. Salanne, B. Rotenberg, K. Naoi, K. Kaneko, P.-L. Taberna, C. Grey, B. Dunn and P. Simon, *Nat. Energy*, 2016, **1**, 16070.

3

STRUCTURE, THERMODYNAMICS, AND DYNAMICS OF THE RTIL OUT OF EQUILIBRIUM DUE TO A SHEARING INTERFACE WITH GOLD

3.1 BACKGROUND AND MOTIVATION

Building on the equilibrium characterisation of [BMIM][BF_4] at the gold interface from chapter 2, in this chapter, our focus shifts to the exploration of the structural and dynamical characteristics of the RTIL [BMIM][BF_4], as it interacts with flat gold slabs under the influence of shear motion. This investigation aims to shed light on the impact of external mechanical forces on the RTIL, contrasting with the intrinsic electrostatic effects, such as image charge interactions, that were the subject of the preceding chapter. Through this comparative analysis, we aim to deepen our understanding of how RTILs respond to different types of stimuli, which is essential for their application in various technological and industrial processes.

The behaviour of RTILs under shear flow within nanoconfined environments is particularly intriguing due to the unique properties that arise from the confined geometries. Previous studies have indicated that metallic confinement can induce a transition toward a solid-like mechanical response in RTILs, which significantly affects their tribological properties and potential applications as lubricants. This study delves into the molecular dynamics of 1-butyl-3-methylimidazolium tetrafluoroborate ([BMIM][BF_4]) confined between gold slabs, exploring how shear flow influences the structure and dynamics of the ionic liquid at the interface.

3.2 INTRODUCTION TO THE STUDY

3.2.1 *Density and interfacial structure*

We studied the influence of the shearing interface on the structure of the ionic liquid through its density profiles at different shearing velocities. The utilisation of density profiles as a diagnostic tool is pivotal in the analysis of interfacial structure, as they provide a direct measure of the spatial distribution of ions across the interface. By mapping out the variations in ion concentration, density profiles enable us to discern the subtle changes in the structural organisation that occur under shear stress. This is particularly insightful for identifying stratification, layering phenomena, and the extent of molecular ordering, which are crucial for understanding the interfacial behaviour and the mechanisms governing the liquid's response to external forces. The use of density profiles here therefore offers an extended snapshot from the equilibrium state, revealing the dynamic adaptations of the ionic liquid's structure upon increasing shear flow velocity.

The density profile analyses of the ionic liquid showed that the most crucial difference in the stratification of the liquid upon shearing the interface is a narrowing of the density profile peaks, which suggest a more densely packed ionic arrangement at the interface. The positions of the peaks, however, remained predominantly unchanged at the interface. This is exemplified by the density profile of the anions in Figure 4 of this chapter's article

on page 44 where the system is at a shear velocity of $v_{slab} = \pm 10\,m\,s^{-1}$. Similarly, at an increased velocity of $v_{slab} = \pm 20\,m\,s^{-1}$, the interfacial structure shown in Figure 19c remains essentially identical to that of an equilibrium system with respect to peak position, indicating a remarkable structural resilience.

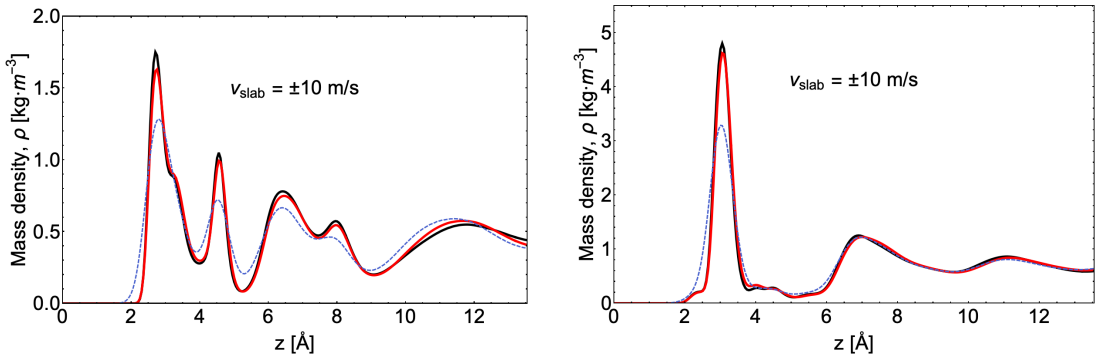

(a) Density profile of anions at slab velocity of $\pm 10\,m\,s^{-1}$.

(b) Density profile of cations at slab velocity of $\pm 10\,m\,s^{-1}$.

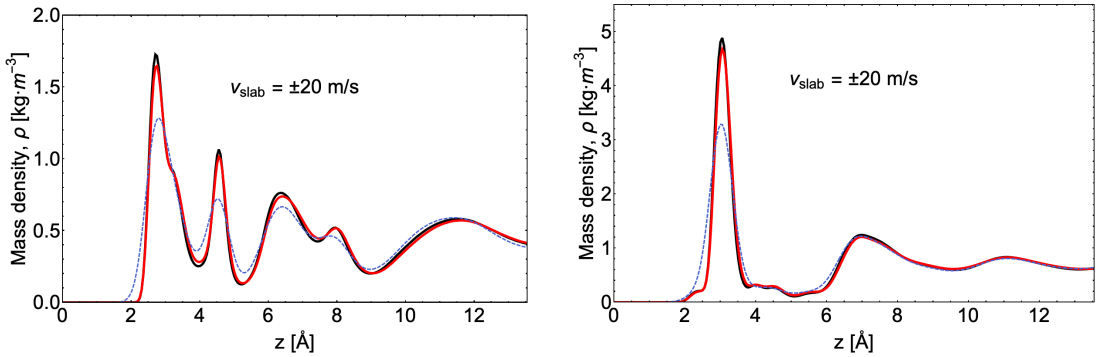

(c) Density profile of anions at slab velocity of $\pm 20\,m\,s^{-1}$.

(d) Density profile of cations at slab velocity of $\pm 20\,m\,s^{-1}$.

Figure 19: Density profiles of anions and cations at different slab velocities. The blue dashed lines represent the respective density profile at 298 K at equilibrium, where no shear is applied and the thermostat is applied to the whole system.

3.2.2 *Orientation of cations*

To further probe the structural resilience inferred from the density profiles under varying shear velocities, we conducted analyses on the cation orientation. The cation [BMIM] has an elongated structure with multiple orientational degrees of freedom which play a significant role in the structural arrangement of both cations and anions at the interface. It was therefore crucial to quantify the effect of the shearing interface on these orientational degrees of freedom and consequentially on the ionic liquid structure.

The study revealed that the cations, to a significant extent, retain their equilibrium orientation. This retention is apparent, irrespective of changes in shearing velocity and temperature, as evidenced by the angular distribution plots in Figure 20.

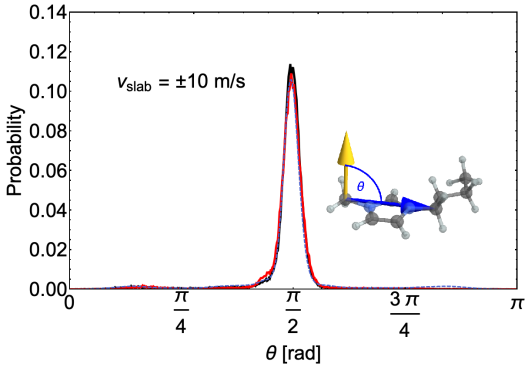

(a) Distribution of angle made by the axis through the imidazolium, at the interface with slab velocity of $\pm 10\,\mathrm{m\,s^{-1}}$.

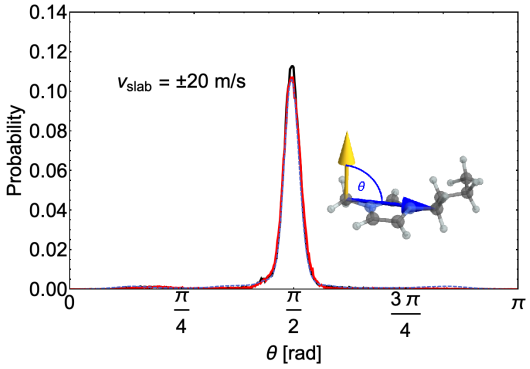

(b) Distribution of angle made by the axis through the imidazolium, at the interface with slab velocity of $\pm 20\,\mathrm{m\,s^{-1}}$.

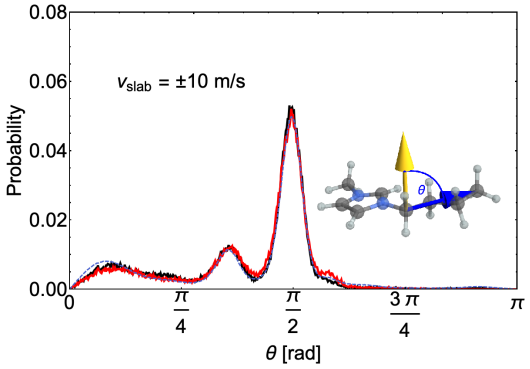

(c) Distribution of angle made by cation tail at the interface at slab velocity of $\pm 10\,\mathrm{m\,s^{-1}}$.

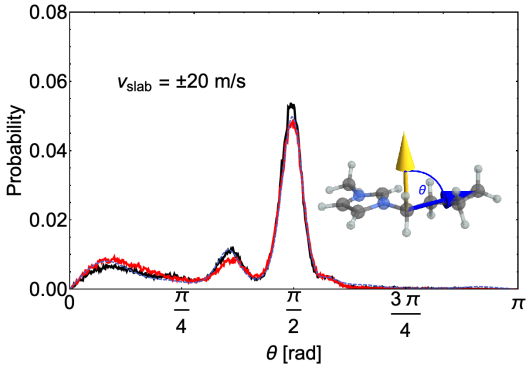

(d) Distribution of angle made by cation tail at the interface at slab velocity of $\pm 20\,\mathrm{m\,s^{-1}}$.

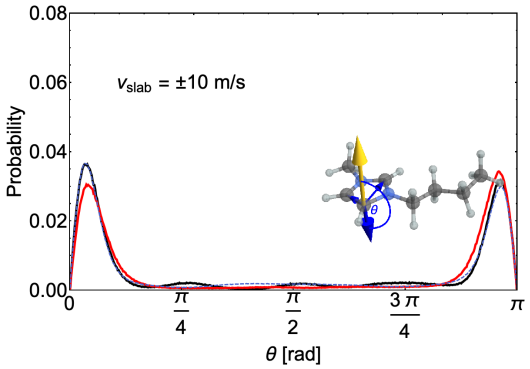

(e) Distribution of angle made by plane of imidazolium ring at the interface at slab velocity of $\pm 10\,\mathrm{m\,s^{-1}}$.

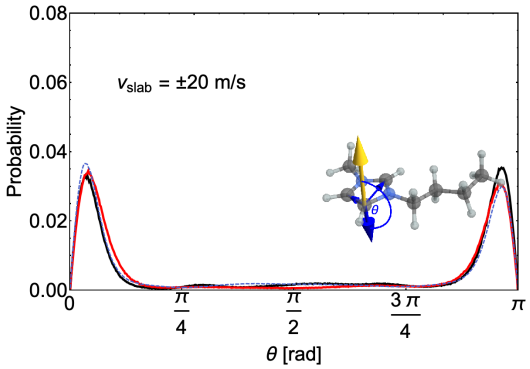

(f) Distribution of angle made by plane of imidazolium ring at the interface at slab velocity of $\pm 20\,\mathrm{m\,s^{-1}}$.

Figure 20: Distributions of angles in ionic liquid at slab velocities of $\pm 10\,\mathrm{m\,s^{-1}}$ (left) and $\pm 20\,\mathrm{m\,s^{-1}}$ (right). The blue dashed lines represent those at equilibrium and at 298 K.

3.2.3 *Steinhardt order parameter*

The phenomenon of crystallisation in a disordered glassy state at a weakly shearing interface presents a fascinating interplay between order and disorder. To delve deeper into the intricacies of the interfacial structure, we have previously employed various methodologies that have provided us with a foundational understanding. However, to further

our analysis, we now turn our attention to the local bond-orientational order analysis, a technique pioneered by Steinhardt et al. [163].

The local bond-orientational order analysis offers a robust framework for characterising the local arrangement of particles. By employing this method, we can discern the subtle differences between local crystal structures within the IL. One important feature of the Steinhardt order parameter is its rotational invariance, which ensures that the characterisation of the structure remains consistent regardless of the orientation of clusters.

We calculated the global Steinhardt order by averaging the local orientational order parameter for the ith atom

$$q_6(i) = \sqrt{\frac{4\pi}{13} \sum_{m=-6}^{6} |q_{6m}(i)|^2} \tag{33}$$

where $q_{6m}(i)$ are components of a 13-dimensional complex vector, used to describe the locality of the ith atom. It is defined as

$$q_{6m}(i) = \frac{1}{N_{nn}(i)} \sum_{j=1}^{N_{nn}(i)} Y_{6m}(\theta_{ij}, \phi_{ij}) \tag{34}$$

which is an average over all nearest neighbours of the ith atom, $N_{nn}(i)$ of the spherical harmonics $Y_{6m}(\theta_{ij}, \phi_{ij})$ of polar and azimuthal angles θ_{ij} and ϕ_{ij} made by the vector $\mathbf{r}_{ij}$ to some reference coordinate. The global order parameter Q_6 is then calculated as the average of $q_6(i)$ over all atoms.

Figure 21 shows the Q_6 profiles at slab velocities of $10\,\mathrm{m\,s^{-1}}$ and $20\,\mathrm{m\,s^{-1}}$, respectively, at the two temperature levels. The temperature profiles are only included to demonstrate the parabolic nature of the Q_6 profile.

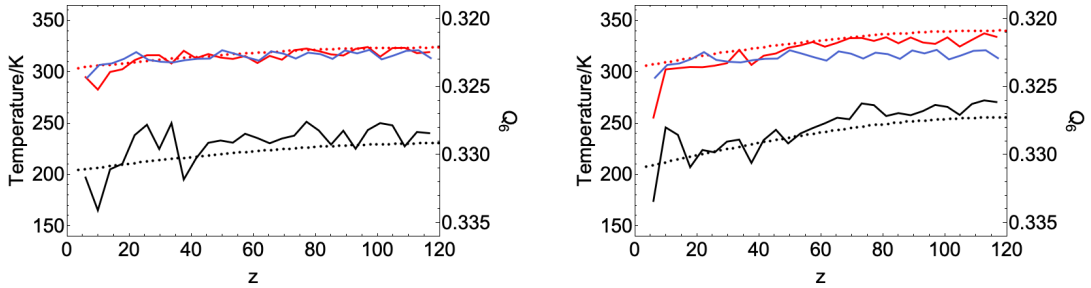

(a) Q_6 and temperature profiles at $\pm 10\,\mathrm{m\,s^{-1}}$ slab velocity.

(b) Q_6 and temperature profiles at $\pm 20\,\mathrm{m\,s^{-1}}$ slab velocity.

Figure 21: Steinhardt global order parameter Q_6 and temperature profiles at different slab velocities. Dotted curves represent temperature profiles while joined curves represent the Q_6 profiles. The blue is the Q_6 profile for an equilibrium system thermostatted at 298 K.

3.2.4 *Shear viscosity and shear thinning*

In our simulations, we had the flow of the liquid in the direction y and a velocity gradient in the direction z. We calculated the shear viscosities from the average of the components

of pressure tensor in these directions in the corresponding region R, and the shear rate $\dot{\gamma}_R$ in this way:

$$\eta_R = -\frac{\langle P_{yz} \rangle}{\dot{\gamma}_R} \tag{35}$$

$\dot{\gamma}_R$ being evaluated as:

$$\dot{\gamma_R} = \frac{2 \times v_B}{h_R},$$

where h_R is the thickness of the region R.

Table 3 shows the shear viscosity at different slab velocities calculated for the whole cavity of ionic liquid bounded at ±118.6 Å and for its midsection bounded by ±20 Å where we observe ideal Couette flow. We report also the velocities at these bounds and the average temperature within the bounds.

Table 3: Boundary velocity, average temperature, and viscosity at slab velocities $\pm 10\,m\,s^{-1}$ and $\pm 20\,m\,s^{-1}$ for low and high temperatures.

$v_{slab}/m\,s^{-1}$	Bounds/Å	Low temperature			High temperature		
		$v_B/m\,s^{-1}$	$\bar{T}/K$	$\eta/mPa\cdot s$	$v_B/m\,s^{-1}$	$\bar{T}/K$	$\eta/mPa\cdot s$
±10	±20.0	2.8	229.2	14.3	2.4	323.3	9.9
	±118.6	10.0	202.1	22.7	10.0	302.4	17.9
±20	±20.0	6.3	253.0	6.7	4.8	339.2	6.3
	±118.6	20.0	202.9	12.3	20.0	303.6	8.2

3.2.5 *Pressure in "frozen" layer and normal stress coefficients*

We show here in Table 4 a comparison of the average pressure in the "frozen" layer to that of the rest of the liquid for all our simulations. The pressure in a region is calculated from the average pressure tensor **P** of all atoms in that region as

$$p = \frac{1}{3V} \mathrm{Tr}(\mathbf{P}) \tag{36}$$

where V is the volume of the region under consideration.

Table 4: Average pressure in "frozen" layer p_f ($0 < z \leqslant \lambda$) in comparison with average pressure of rest of ionic liquid p_r ($|z| < \lambda$).

$v_{slab}/m\,s^{-1}$	Low temp.			High temp.		
	λ/Å	p_f/MPa	p_r/MPa	λ/Å	p_f/MPa	p_r/MPa
10	10.60	−344.01	−100.44	5.96	−337.10	47.08
20	16.51	−257.19	−74.91	6.49	−281.27	73.77

The average differences in normal stress coefficients are crucial in determining whether or not the liquid is readily deformable in a certain direction—whether or not the liquid is Newtonian. However, it is necessary to have a converged pressure tensor. In Figure 22 we show an example convergence of the diagonal components of the pressure tensor and their total, over time, for our low temperature system at $10\,\mathrm{m\,s^{-1}}$ slab velocity.

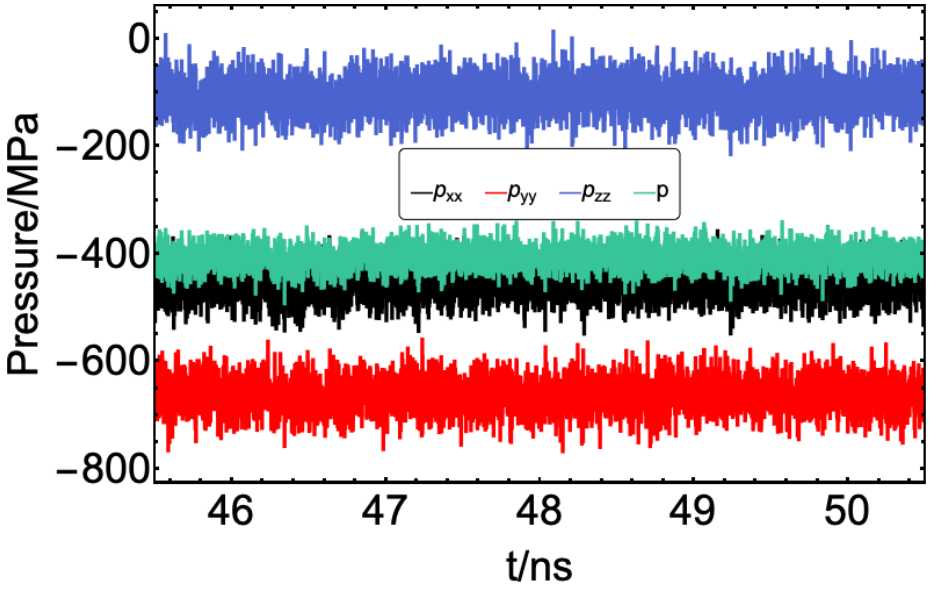

Figure 22: Convergence of the diagonal components of the pressure tensor for lower temperature system with slab velocity of $\pm 10\,\mathrm{m\,s^{-1}}$.

The first and second normal stress coefficients are defined here as

$$\Psi_1 = \frac{\langle P_{zz} - P_{yy} \rangle}{\dot{\gamma}^2} \tag{37}$$

and

$$\Psi_2 = \frac{\langle P_{xx} - P_{zz} \rangle}{\dot{\gamma}^2} \tag{38}$$

Table 5 shows the normal stress coefficients and their ratios, calculated from the diagonal elements of the pressure tensor according to these equations. Figure 23 shows their convergence over time, for our low temperature system at $10\,\mathrm{m\,s^{-1}}$ slab velocity.

Table 5: Average first and second normal stress coefficients, and their ratios at low and high temperatures.

$v_{slab}/\mathrm{m\,s^{-1}}$	Low temp.			High temp.		
	$\Psi_1/\mathrm{Pa\,s^2}$	$\Psi_2/\mathrm{Pa\,s^2}$	$\frac{-\Psi_2}{\Psi_1}$	$\Psi_1/\mathrm{Pa\,s^2}$	$\Psi_2/\mathrm{Pa\,s^2}$	$\frac{-\Psi_2}{\Psi_1}$
10	1050.88	−653.16	0.62	935.25	−555.63	0.59
20	265.15	−164.93	0.62	235.33	−138.66	0.59

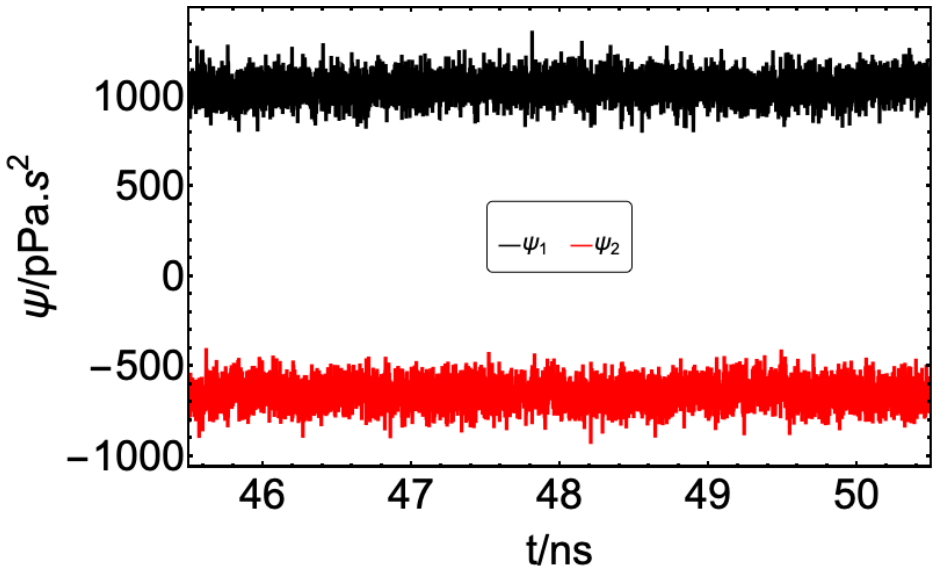

Figure 23: Convergence of ψ_1 and ψ_2 for lower temperature system with slab velocity of $\pm 10\,\mathrm{m\,s^{-1}}$.

3.2.6 *Load and friction*

We increased the load on the ionic liquid by moving the each gold slab in steps of 0.5 Å towards the other every 10 ps until the desired reduction in the slab separation was reached, and then a run of 52 ns. For a given slab separation reduction of s, the load L_s corresponding to a slab separation of $h = h_0 - s$ where h_0 is the equilibrium slab separation, is calculated with the difference in the average normal forces on the slabs. The average force on the lower slab, say, is calculate every 1 ps as

$$F^{\text{lower}} = \sum_{i \in \text{lower}} \langle \mathbf{f}_i(t) \rangle \tag{39}$$

then the load per area is evaluated as $f_L = 0.5 \times (F_z^{\text{upper}} - F_z^{\text{lower}})/(L_x L_y)$. Table 6 shows the load at different temperatures, velocities and slab separations. Figure 24 shows the density profiles at the smallest slab separation simulated, $h_0 - 12$ Å. The dashed lines indicate the corresponding density profiles at slab separation of h_0.

Table 6: Load on systems. Each L_s is the load for system with slab separation $h = h_0 - s$ where $h_0 = 237.15$ Å.

$v_{\text{slab}}/\mathrm{m\,s^{-1}}$	Low temperature			High temperature		
	L_0/GPa	L_6/GPa	L_{12}/GPa	L_0/GPa	L_6/GPa	L_{12}/GPa
10	−0.09	−0.01	0.09	0.06	0.15	0.27
20	−0.07	0.02	0.12	0.08	0.17	0.32

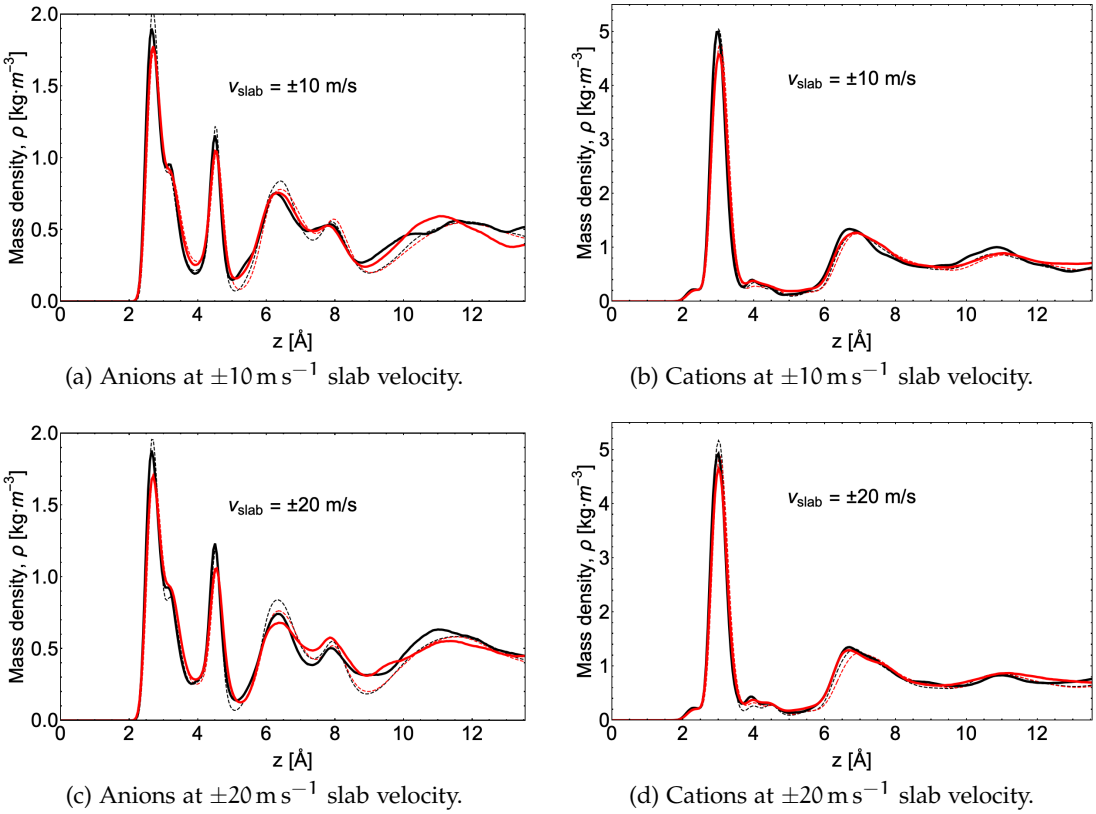

(a) Anions at $\pm 10\,\mathrm{m\,s^{-1}}$ slab velocity.

(b) Cations at $\pm 10\,\mathrm{m\,s^{-1}}$ slab velocity.

(c) Anions at $\pm 20\,\mathrm{m\,s^{-1}}$ slab velocity.

(d) Cations at $\pm 20\,\mathrm{m\,s^{-1}}$ slab velocity.

Figure 24: Density profiles of anions and cations at slab velocities of $\pm 10\,\mathrm{m\,s^{-1}}$ and $\pm 20\,\mathrm{m\,s^{-1}}$ at slab separation of $h_0 - 12\,\text{Å}$. The dashed line represents the corresponding density profile of cations at slab separation of h_0.

3.3 OBJECTIVES

This research aimed to address several critical questions regarding the behaviour of [BMIM][BF_4] under shear flow within a metallic nanoconfinement:

- CRYSTALLISATION UNDER SHEAR: Can shear flow promote the crystalline phase in [BMIM][BF_4]?
- SOLID-LIKE LAYER FORMATION: Does shear flow induce the formation of a solid-like layer at the interface with metallic surfaces?
- TRIBOLOGICAL PROPERTIES: What are the tribological characteristics of nanoconfined [BMIM][BF_4] under shear conditions?

The study employed molecular dynamics simulations to investigate these aspects, providing insights into the non-equilibrium properties of confined ionic liquids.

3.4 KEY FINDINGS

1. INTERFACIAL DENSITY PROFILES: The density profile at the interface narrow under shear. The number of ions in the first nanometre at the interface slightly increases under shear, suggesting enhanced layering due to shear-induced ordering.

2. CATION ORIENTATION: The orientation of [BMIM] cations at the interface remains largely unchanged by the shearing motion of the interface, indicating strong adhesion forces between the ionic liquid and the gold surface. The imidazole rings of the cations tend to lie flat on the Au(111) surface, maintaining their orientation regardless of the applied shear.

3. POISSON POTENTIAL PROFILES: The potential drop at the interface, as characterized by the Poisson potential profile, remains consistent with the equilibrium system under different shear velocities, indicating minimal changes in the electric double layer structure due to shear flow.

4. VISCOSITY AND SHEAR RATES: The shear viscosity of [BMIM][BF_4] decreases with increasing shear rates, suggesting non-Newtonian behaviour. The viscosity reduction is more pronounced at higher shear rates and is accompanied by changes in normal stress coefficients, indicative of complex rheological behaviour under shear.

5. GLASSY "FROZEN" LAYER FORMATION: A "frozen" layer forms at the interface, extending to a few nanometres. This layer was found to be glassy rather than crystalline.

3.5 CONCLUSION

This study provided a detailed molecular-level understanding of how shear flow affects the structural and dynamic properties of [BMIM][BF_4] confined between metallic surfaces. The findings highlight the resilience of the ionic liquid at the interface, the formation of a few nanometres of solid-like glassy layer, and the persistence of non-Newtonian behaviour of the liquid under shear, all of which are critical for the application of RTILs in lubrication and other technologies. These insights contribute to the broader understanding of RTIL behaviour in confined environments, paving the way for their optimised use in advanced material processes.

PCCP

PAPER

View Article Online
View Journal | View Issue

Cite this: *Phys. Chem. Chem. Phys.*, 2021, **23**, 24357

Effects of shear flow on the structure and dynamics of ionic liquids in a metallic nanoconfinement†

Samuel Ntim and Marialore Sulpizi *

Received 9th March 2021,
Accepted 1st October 2021

DOI: 10.1039/d1cp01055g

rsc.li/pccp

It has been shown that a weak shear can induce crystallisation in a disordered, glassy state. In this study, we use molecular dynamics simulations in order to investigate the out-of-equilibrium properties of [BMIM][BF_4] confined between metal slabs. In particular, we want to understand the extent to which the shear flow modifies the interfacial properties. In particular, the questions we address here are (i) is the shear able to promote the crystalline phase in [BMIM][BF_4]? (ii) Can, as a consequence of shear flow, a solid-like layer develop at the interface with a metallic surface? (iii) What are the tribological properties of nanoconfined [BMIM][BF_4]? We find that the system behaves quite differently from the ideal linear Couette flow. Indeed, the portion of fluid closer to the shearing slabs behaves as a disordered, solid-like layer, which, under the investigated conditions extends to a few nanometres. The linear velocity regime is only recovered in the central region of the ionic liquid slab. The formation of such a solid-like glassy rather than crystalline layer is in agreement with recent mechanical impedance measurements performed on nano-confined ionic liquids.

1 Introduction

Room Temperature Ionic Liquids (RTILs) are acquiring a more and more prominent role as electrolytes in safer batteries, cleaner solvents, and catalysts to improve efficiency in diverse chemical processes. Nonetheless, they are still far from being out-of-the-shelf tools in the chemical industry. In particular their behaviour in confinement, which is crucial to the functioning of modern devices as lithium-ion batteries and supercapacitors,[1] but also of relevance to the emerging field of nanofluids[2] (*e.g.*, in nanofluidic memristors[3]), is still puzzling and elusive. An important role in determining the properties of RTILs in confinement is played by the confining material. For example, for [BMIM][BF4] confined between metallic surfaces a transition toward a solid-like mechanical response below a threshold confinement was observed.[4,5] However the impact of metallic confinement on the properties of confined RTILs remains to be fully assessed, and calls for an understanding at the molecular scale.[6,7] The appearance of a solid-like layer at the confining surface is also at the base of the capability of RTILs to act as lubricants. Starting from 2001 the use of ILs as lubricants has been proposed,[8] as they show lower friction than conventional oils[9,10] and may help to reduce wearing in various systems.[11–14] In some cases quantised friction has been observed in sheared ionic liquids, namely discontinuities in the friction coefficients upon compression.[15–17] Given their very high viscosity, RTILs may be out of equilibrium under commonly encountered experimental conditions. In Surface Force Balance (SFB) experiments, it has been shown that the viscous force can be of the same order of magnitude as the reported electrostatic forces depending on the approach velocities employed. It is therefore important to disentangle the equilibrium and viscous contribution to the measured total forces.[18]

In this study, we use molecular dynamics simulations in order to investigate the out-of-equilibrium properties of RTILs. In particular we want to understand to what extent the shear modifies the interfacial properties. For example, is shear able to promote the crystalline phase in [BMIM][BF4]? Can as a consequence of shear flow a solid-like layer develop at the interface with a metallic surface? Finally, what are the tribological properties of nano-confined [BMIM][BF4] under shear? The answers to these questions are organised into three sections: namely a detailed discussion of (i) temperature and velocity profiles, (ii) the structural analysis of the interface and finally (iii) a load and friction paragraph.

2 Results and discussion

2.1 Temperature and velocity profiles

Shear is applied by adding velocities to solid walls confining the liquid system.[19] The system setup with moving solid surfaces is

Institut für Physik, Johannes Gutenberg Universität, Staudingerweg 7, 55128-Mainz, Germany. E-mail: sulpizi@uni-mainz.de

† Electronic supplementary information (ESI) available. See DOI: 10.1039/d1cp01055g

shown in Fig. 1. Typically high shear rates (generally $\geq 10^7$ s^{-1}) are required in order to reach steady state conditions,[20,21] in particular when highly viscous systems as RTIL are considered. Here we will discuss in detail the results for two shear velocities, namely 10 ms^{-1} and 20 ms^{-1}. For each of them two different temperatures are considered for a total of four different systems. The control over the temperature of the system is one of the issues to consider when dealing with non-equilibrium MD simulations. Several methods can be used to thermostat the system in confined NEMD simulations and one can refer to Bernardi *et al.*[22] and Yong and Zhang[23] for a couple of reviews. For shear flow simulations in confinement, the thermostat is most commonly applied only to the wall atoms (and in the two directions orthogonal to the flow). In this way a thermal gradient develops through the thickness of sheared fluid,[24] in a similar way as it happens in tribology experiments.[25] In our case the thermostat is applied to a portion of the confining walls (highlighted in orange in Fig. 1). In the following, two systems will be considered, with reference temperatures of the thermostats set to 200 K and 300 K, respectively. When the system reaches the steady state we obtain an approximately parabolic temperature profile in the IL, as typically expected in lubricants in tribology experiments.[26,27] Fig. 2 shows the temperature profiles, where filled circles correspond to the system with shear velocities of 10 ms^{-1} and the open circles to the system with shear velocities of 20 ms^{-1}. The maximum temperatures of the IL are found in the middle of the liquid and is significantly higher than the set target temperature which is assigned to the metal slab. For example, with a set reference temperature of 200 K, the temperature in the centre of the liquid can reach a maximum of about 230 K. Higher shear velocities (open circles corresponding to the higher shear velocity in Fig. 2) lead to even higher increase of temperature of the liquid, as more energy injected into the systems is dissipated. Table 1 shows the minimum and maximum temperatures in the IL for the two given shear velocities.

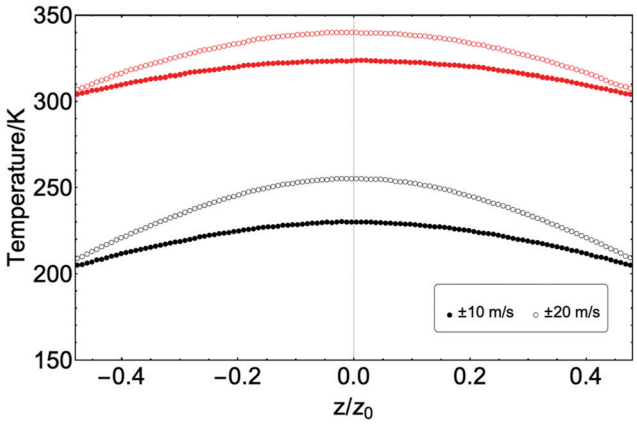

Fig. 2 Parabolic temperature profiles of the IL temperature in the steady state regime for the two different shearing velocities. Filled circles correspond to the system with shear velocity of 10 ms^{-1} and the open circles to the system with shear velocity of 20 ms^{-1}. The black symbols correspond to a reference temperature of 200 K within the slab, while the red ones to a reference temperature of 300 K.

In nanoconfinement the flow profile can deviate from the ideal linear velocity profile (Couette flow) as it was first suggested by surface force apparatus experiments[28] and later also confirmed by NEMD simulations.[29] Depending on the applied pressure various types of shear localisation have been identified.[30–33] For example the so called central localisation occurs when the outer regions of the fluid move jointly with the confining walls, while the central region is sheared, and *e.g.*, Couette flow can still be observed in such central region. An opposite behaviour where the outer regions of the fluid are sheared while the central region remains unsheared is also possible. This regime is typically addressed as a plug slip.[34] Fig. 3 shows the velocity profiles obtained by shearing the metal walls with opposite velocities of ±10 ms^{-1} and ±20 ms^{-1}. Our results show that although an ideal linear Couette flow can be detected in the central region of the liquid slab, the regions closer to the walls move jointly with the confining

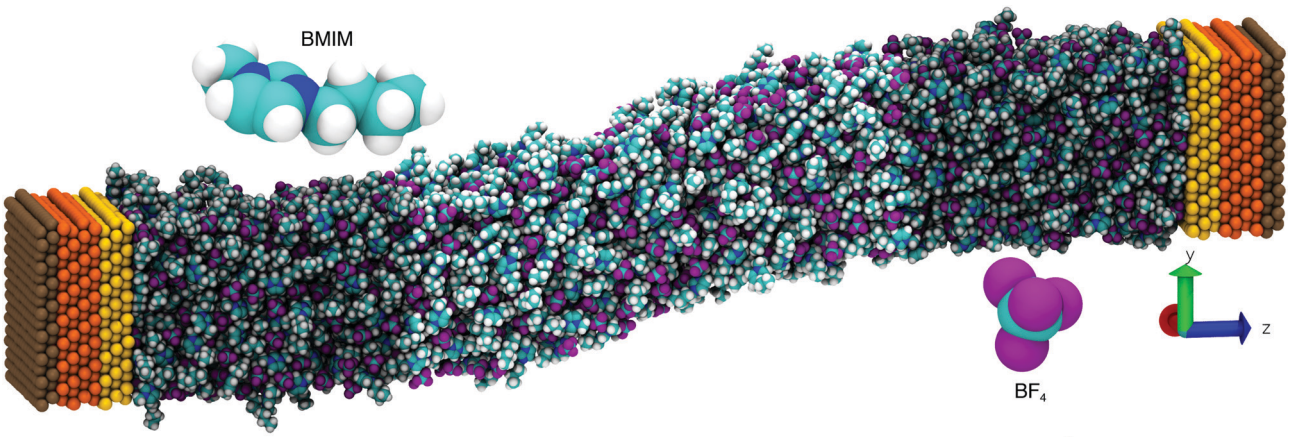

Fig. 1 Simulation box of two Au(111) slabs separated by 1200 pairs of [BMIM][BF_4]. Constant velocity is applied to the outermost layers (shown in brown) while the innermost layers (shown in yellow) are free to move according to interactions in the system. Layers coloured orange are coupled to a thermostat. Lighter coloured ionic liquid is in a linear Couette flow regime while darker coloured ionic liquid is more closely flowing along with the slab.

Table 1 Minimum and maximum temperatures (at the metal surface and in the middle of the bulk) in the ionic liquid for the two shear velocities at the low and high temperatures

	Thermostat 200 K (low)		Thermostat 300 K (high)	
v_{slab}/ms^{-1}	T_{Min}/K	T_{Max}/K	T_{Min}/K	T_{Max}/K
10	203.0	230.0	303.1	323.9
20	204.6	254.5	304.8	340.2

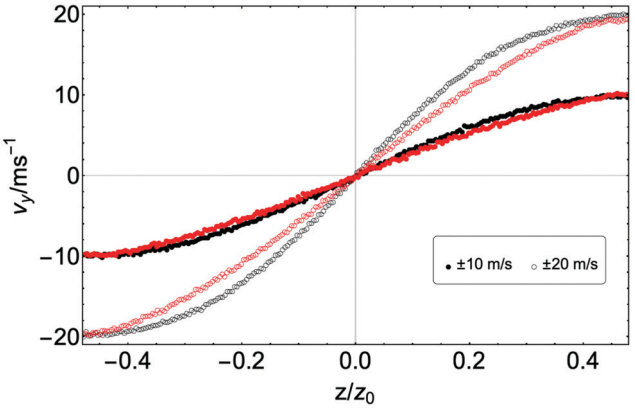

Fig. 3 Velocity profile of IL at slab velocity of ±10 ms^{-1} and ±20 ms^{-1}. Black points represent the lower temperature system while red points represent higher temperature for the corresponding shear velocity.

walls. The size of the ''frozen'' region, λ, has been identified as the distance from the surface of the slab within which the difference in velocity $v_{slab} - v \leq 0.025 v_{slab}$ and is reported in Table 2.

The average temperature in the frozen slab is also reported. For the lower temperature systems the ''frozen'' layer extends over 1 nm from the surface. It is interesting to notice here that although we call this region as ''frozen'', the average temperatures there are higher than the liquid's bulk freezing temperature of 202.15 K. For the higher temperature system the ''frozen'' layer is much smaller and below 1 nm, in this case, though, the local temperature at the interface is much higher than bulk freezing temperature, and around 305 K.

2.2 Shear viscosity and normal stress coefficients

Already on the bulk phase, the effect of shear rate on the sheared fluid can be quite diverse. *e.g.* for some ammonium based ILs a Newtonian behaviour has been observed at low shear rates, with a transition to shear thinning behaviour at higher shear rates. On the other hand, the opposite behaviour, namely shear thickening has been also observed for some ILs and attributed to packing and orientation effects.[35] More specifically, for the imidazolium-based ionic liquids, experimental results showed shear-thinning and shear-thickening behaviours for [BMIM][PF6] and [BMIM][NO3], respectively.[36] Other recent studies have questioned the non-Newtonian behaviour in studies attributing the decrease in the viscosity to viscous heating.[37] In the specific case of our interest, namely [BMIM][BF4], the presence of nano-confinement and of specific strong interactions with the surface already induces dramatic changes in the local viscosity under equilibrium conditions. In our previous work[7] we have shown that the self-diffusion coefficient recovers its bulk value only at a distance of about 10 nm from the surface. Such an effect is, of course, reflected in a parallel behaviour of the viscosity. In the nano-confined [BMIM][BF4], the interplay between such interfacial effects and shearing may lead to a new situation.

Table 2 Thickness of frozen IL layers and their average temperature within, for the two shear velocities and the two target temperatures

	Thermostat 200 K (low)		Thermostat 300 K (high)	
v_{slab}/ms^{-1}	λ/Å	T/K	λ/Å	T/K
10	10.6	205.5	6.0	304.0
20	16.5	211.6	6.5	306.3

We have also calculated the shear viscosity of the system from the shear flow simulations. In our simulations, we have the flow of the liquid in the y direction and a velocity gradient in the z direction. We calculate the shear viscosities from the components of the average pressure tensor in the corresponding region R and the shear rate $\dot{\gamma}_R$ using the velocity v_B at the boundary of that region in this way:

$$\eta_R = -\frac{\langle P_{yz} \rangle}{\dot{\gamma}_R} \quad (1)$$

where $\dot{\gamma}_R = \frac{2 \times v_B}{h_R}$, h_R being the thickness of the region R (more details on the calculations can be found in the ESI†). We have calculated the shear viscosity using the central portion of the fluid where the linear Couette flow is established. It is difficult to have direct comparison between the two different shear rates, as the increased shear rate is also responsible for an overall increasing in the temperature of the system. However, if we compare, for the lower temperature thermostat (200 K), the linear portion of the sheared liquid for the 10 ms^{-1} and the 20 ms^{-1}, we see that the viscosity decreases from 14.3 mPa s to 9.9 mPa s. The same is true also for the higher temperature systems (thermostat at 300 K) where the viscosity decreases from 6.7 mPa s to 6.3 mPa s when increasing the shear rate from 10 ms^{-1} to 20 ms^{-1}. Such behaviour suggests that the fluid is, at the considered shear rates, already in the non-Newtonian regime. For a non-Newtonian liquid undergoing shear flow, not only is the viscosity dependent on the applied shear rate, but also the diagonal elements of the pressure tensor show important difference, which appear in non-zero normal stress coefficients. The first and second normal stress coefficients are defined here as

$$\psi_1 = \frac{\langle P_{zz} - P_{yy} \rangle}{\dot{\gamma}^2} \quad (2)$$

$$\psi_2 = \frac{\langle P_{xx} - P_{zz} \rangle}{\dot{\gamma}^2} \quad (3)$$

From the physical point of view a non-zero coefficient corresponds to a compressing force perpendicular to the shearing direction.

The first stress coefficient ψ_1 is positive and decreases with the increasing of the shear rate. The second coefficient is negative and also decreases in modulus with increasing shear rate (see Table SIV, ESI†). This behaviour has also been found for other fluids having a non-Newtonian behaviour.[38] The ratios $-\psi_2/\psi_1$ are also reported in Table SIV of the ESI,† which shows that the values are $\sim$0.6, so higher than the 0.2 which, for example, is reported for branched polymers, where deformation occurs with shear.[38]

2.3 Structural properties at the interface

As the next step we are going to investigate the structural properties of the ''frozen'' layer at the interface, in order to compare them with the properties of interfacial fluid under equilibrium conditions. The shear motion only slightly modifies the interfacial structure. Fig. 4 shows the density profile of the anions at the interface with and without applied shear velocity of 10 ms^{-1}. The black and the red profiles correspond to two different reference temperatures. At the sheared interface the density profile of the ions (in the specific case of Fig. 4, the anions are shown) becomes narrower with respect to the equilibrium case. This is particularly evident in the system with the lower interface temperature (205 K) black line in Fig. 4. The total number of anions in the first nanometre at the interface is slightly increased by 0.013 nm^{-2} and 0.022 nm^{-2} for the lower and higher temperature cases, respectively. Similar profiles are also found when comparing the density profiles for the cations (see Fig. S2, ESI†). The cations, on the other hand (see the ESI†) show a decrease of about 0.027 nm^{-2} at the higher temperature (304 K) while remaining approximately the same at the lower temperature (205 K).

As the cations ([BMIM]) present a non-spherical structure, it is interesting to check if the shear flow modifies their orientation at the interface. Previous equilibrium simulations of the metal/liquid interface have shown how the cations tend to lie flat on the surface maintaining their imidazole ring parallel to the Au(111) surface.[7] Fig. 5 shows the orientational distribution of the cations in the adsorbed layer and in particular, the distribution of the angle between the imidazolium head and the surface of the gold slab as shown in the inset. More details of the orientation of the cations can be found in the Section S2 (ESI†). Essentially the flow does not change the cations orientation at the interface, as the adhesion forces between liquid and surface are extremely strong, as suggested by the work of adhesion calculated in our previous work.[7]

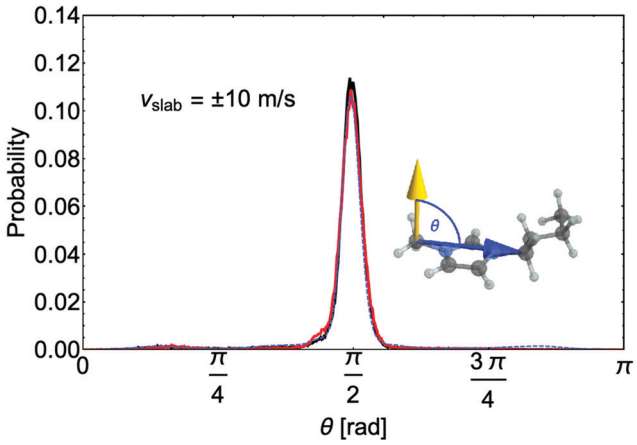

Fig. 5 Distribution of angle made by cation head at the interface at slab velocity of ±10 ms^{-1}. The blue dashed line represents that at 298 K and without shear. The inset is a schematic to visualise the angle θ where the yellow arrow represents the normal to the gold surface.

The structure and the arrangement of the ions at the interface determine the structure of the electric double layer (EDL) and therefore the potential drop at the interface. Fig. 6 presents the profile of the Poisson potential at the interface as function of the distance from the gold surface in comparison to the equilibrium system (blue dashed line) at 298 K. The profiles for the two different shearing velocities are very close, and, within the error bars, resemble that of the equilibrium system (also reported in the figure as a blue dashed line).

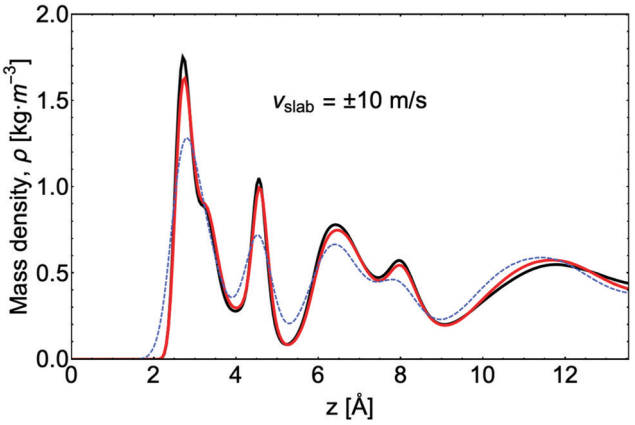

Fig. 4 Density profile of anions at slab velocity of ±10 ms^{-1}. The black and red lines represent the low and high temperatures respectively. The blue dashed line represents the density profile of anions thermostatted at 298 K coupled to the whole system and without shear.

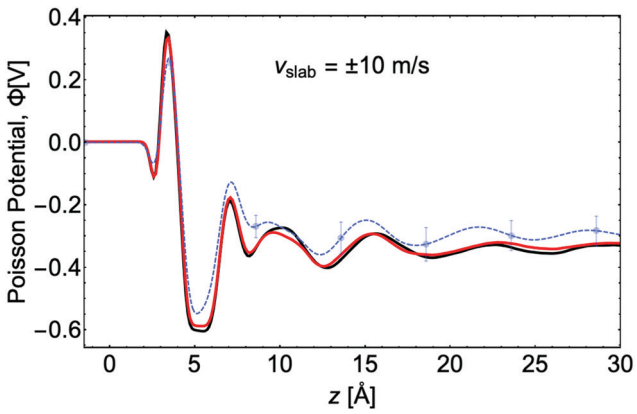

Fig. 6 Potential drop at the interface at slab velocity of ±10 ms^{-1}. The blue dashed line with error bars represents the same at 298 K and without shear. Black and red profiles correspond to low and high temperatures respectively.

It has been shown that a weak shear can induce crystallisation in a disordered, glassy state.[39,40] For [BMIM][BF4] no crystal structure has been experimentally detected so far, under equilibrium conditions. Rather the RTIL can get supercooled and form glasses.[41] A question that may be raised here is whether the shear could eventually favour the formation of a crystalline structure at the interface. To this scope an analysis of the crystal order, as provided *e.g.*, by the sixth order Steinhardt parameter (Q_6) has been performed. Q_6 allows to measure the degree to which the first coordination shell around an atom is ordered. It varies between 0 (for liquid-like order) and 1 (for solid-like order). In our current study, we compare the Q_6 value obtained in the sheared interface with that of the equilibrium (see Section S3 in the ESI,† for figures). The Q_6, for all temperatures and velocities, was of the order of 0.32, just as it is in the equilibrium simulation, and would rather exclude the formation of crystalline structures induced by shearing. This is in agreement with recent experimental observations. For example 2D IR spectroscopy experiments on RTILs thin films have revealed an extremely slow dynamical behaviour, resembling that of cooled liquids.[42] Moreover the mechanical measurements performed on the nanoconfined RTILs suggested a glassy nature of the solid-like interfacial layer.[5] The glass-like dependence of conductivity was also recently reported in conductivity measurements on ionic liquids of the imidazolium type in single conical glass nanopores with confinements as low as 20 nm.[43] A key role in determining the formation of a solid-like layer at the interface is certainly played by the specific surface–liquid interactions. In particular, for [BMIM][BF4] on Au(111) we know that the surface perturbs the dynamical properties of the liquids for several nanometres from the surface, and *e.g.*, bulk diffusion properties are recovered at about 10 from the surface.[7] The variation of Q_6 as a function of the distance from the metal surface correlates with the behaviour of the corresponding temperature profile (also as function of the distance from the metal surface), showing a parabolic curve in the non-equilibrium systems but fluctuating about a constant in an equilibrium system where the thermostat was coupled to the whole system. The Q_6 values as function of the distance from the metal slab are reported in Fig. S9 and S10 (ESI†) for shear velocities of ± 10 ms^{-1} and ± 20 ms^{-1}, respectively.

2.4 Load and friction coefficient

In order to get insights into the friction behaviour at the nanoscale we considered systems with different loads. The strategy is similar to that employed in ref. 44 and 45 where it was shown that from the tangential and normal components of the pressure tensor, calculated in a two-slab geometry, it is possible to obtain accurate friction coefficients. In our simulations the load is not directly applied, but calculated *a posteriori*, varying the separation distance between the confining metal slabs. More details can be found in the ESI.† In practice we reduced the distance between the slabs by 6 Å and 12 Å, respectively. The corresponding normal and lateral forces are reported in Fig. 7. Table SV in the ESI,† shows the load corresponding to difference in slab separation. A detailed analysis of the interfacial structure reveals no major structural differences in the considered load range. In Fig. 7 the average lateral forces per unit area, f_L are plotted against the average load, or normal force per unit area f_N. The graph shows the results for both 10 ms^{-1} and 20 ms^{-1} shearing velocities. A linear dependence between f_L and f_N is found, which can be fitted using the modified Amontons' law,[46] according to

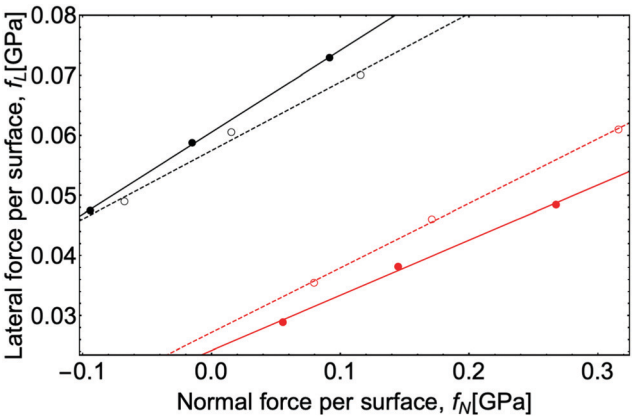

Fig. 7 Mean lateral forces per unit area against mean normal forces on the gold slabs per unit area. Low and high temperatures are shown in black and red respectively while slab velocities of 10 ms^{-1} and 20 ms^{-1} are marked by filled and open circles respectively, and their corresponding lines of best fit in solid and dashed lines respectively.

$$f_L = m f_N + f_0, \quad (4)$$

and permits to calculate the friction coefficient m, and the parameter f_0, an offset related to the adhesive interactions at the metal liquid interface. The values of m are summarised in Table 3. Our table of coefficients of friction for high temperature systems is consistent in order of magnitude with values reported by Canova *et al.*,[47] despite their smaller system size and higher values of lateral forces with respect to those of this work. The low temperature systems show, however, slightly larger friction coefficients. Our values for [BMIM][BF4] are also similar to those obtained for an ionic liquids composed of alkylammonium cations and alkylsulfonate anions confined between, respectively, iron surfaces[44] and amorphous carbon surfaces.[45]

The linear dependence of the lateral force on load in all our simulations suggests that the IL is always in the same frictional regime. The ions arrangement in the layers shows a similar behaviour when comparing three different loads, or in other words we can say that liquid resists the ''squeeze out'' due to the strong interaction between the ions, resulting in a layer

Table 3 Fit parameters for Amontons' law, showing the friction coefficients m and offsets due to adhesive interactions f_0, for the two shear velocities and the two target temperatures

	Thermostat 200 K (low)		Thermostat 300 K (high)	
v_{slab}/ms^{-1}	m	f_0/GPa	M	f_0/GPa
10	0.14	0.06	0.09	0.02
20	0.11	0.06	0.11	0.03

which remains in place at higher pressures. It is possible to compare the friction coefficient obtained from the simulations with the experimental values recently measured in AFM experiments for [BMIM][BF4].[48] In the experiment for mica surfaces, friction coefficients between 0.02 and 0.08 are obtained. Although a direct comparison is not possible as mica is a charged surface, it is still interesting to notice that the values from the simulations (at least for the lower temperature) are of the same order of magnitude.

Our results suggest that the investigated IL can behave as good boundary lubricants. Indeed, the glassy layer which is formed at the interface and strongly adheres to the surface, is able to bear high pressures without substantial modification. When two lubricated surfaces are sliding under high pressure the ''frozen'' layer which cover both sides, would protect them avoiding the direct contact between the surface. This would, in turn, prevent the direct contact between nano-metric asperities eventually present on the surfaces.

Further work should explore how the results discussed here for the condition of zero charge on the surface would be modified in the case of electrified interfaces. Some pioneering work[49] in this direction has been done with some simple physical model showing the friction forces are affected by the surface charge density strengthening the interactions between ionic layers and surfaces, and eventually enhancing lubrication properties of RTIL. More recently the high potential of diluted [BMIM][PF6] mixtures as electrotunable lubricants has been also demonstrated.[49,50]

3 Computational details

We used a pre-equilibrated system made of two gold slabs separated by 1200 pairs of [BMIM][BF4]. Each gold slab has 9 layers of gold atoms in the (111) crystallographic plane. The layers of gold atoms are grouped into sheared, thermostatted and free groups (see Fig. 1). The outermost two layers belong to the sheared group which is the group on which a constant velocity is applied while remaining fixed in the z-direction. A velocity of $-v$ and $+v$ was applied to the lower and upper sheared groups respectively. The innermost three layers belong to the free group which is allowed to freely move according to interactions within system. The four layers in between these two groups belong to the thermostatted group to which is coupled a thermostat. The thermostatted group of each slab is coupled to a separate thermostat in the x- and z-directions, perpendicular to the shear direction. The simulation box is a rectangular parallelepiped $L_x \times L_y \times L_z$ where $L_x = L_y = 4.05457$ and $L_z = 29$. We employ 2D periodic boundary conditions along the x and y directions, decoupling image interactions along the z direction *via* slab correction with vacuum three times the volume of the simulation box. We use the Particle–Particle Particle–Mesh (PPPM) solver for the calculation of electrostatics. The gold atoms are described by a non-polarisable model which accurately reproduce many properties of the metal/water interface.[51] Recently, we have also introduced metal polarisation, which can also take into account the effect of image charges.[52] We decided, here, however, to use the simple non-polarisable model,[51] as we have shown that image charge effects for this specific interface, at least in the equilibrium conditions, are negligible.[7] In order to describe the ionic liquid, we use a non-polarisable model of [BMIM][BF4] that reproduces very well experimental diffusion coefficient, shear viscosity, ionic conductivity and heat of vaporisation of [BMIM][BF4].[53] All Lennard-Jones interactions were cut off at 1.5 nm and Lennard-Jones interactions of non-identical atoms were generated with Lorentz–Berthelot mixing rules. For each slab separation of $h = 23.715$ nm, 23.115 nm and 22.515 nm we perform molecular dynamics simulations where the equations of motion were integrated using the the velocity–Verlet algorithm with a time step of 0.25 fs and using a 2D Nosé–Hoover chain thermostat with 3 chains with a temperature coupling constant of 1 ps coupled to the x and z. In order to obtain a subsequent slab separation, the slabs in the preceding system are shifted in steps of ± 0.5 Å until the desired separation was achieved, allowing for 10 ps of readjustment of the liquid especially near the interface, in between successive slab shifts. In each simulation, we collected system information every 0.5 ps for 52 ns, by which time the system would have reached a steady state and the temperature and velocity profiles already converged. Convergence was achieved faster for higher shear rates. It is also for this reason that we simulate such high shear rates although lower shear rates more closely resemble experiment. Fig. 1 shows a typical simulation system. All simulations were performed using the LAMMPS simulation package.[54]

4 Conclusions

We have presented a systematic analysis of non-equilibrium shear flow simulations of the RTIL [BMIM][BF4] confined between two Au(111) gold electrodes, using atomistic molecular dynamics simulations. The system behaves quite differently from the ideal linear Couette flow. The portion of fluid closer to the metal surface behaves as a glassy solid, which under the investigated conditions extends to a few nanometres. Only in the central region of the RTIL slab the linear velocity regime is recovered. Such a ''frozen'' layer doesn't show a crystalline structure, contrary to what was observed for other systems, but it is rather a glassy state. Although the shear rate used here, and typically employed for molecular dynamics simulations, is rather high, we do expect that such an effect would persist even at lower shear rate. The formation of such solid-like glassy layer is in agreement with recent mechanical impedance measurements performed on nano-confined RTILs. Finally, we discuss the friction of the nano-confined liquid. In all our simulations the lateral force shows a linear dependence on load, suggesting that the IL is always in the same frictional regime. In the explored range of loads, there is no significant change in the ion arrangement at the interface, which, thanks to their strong interactions and the strong interaction with the surface, form a

liquid, which resists the ''squeeze out'' and remains in place at higher pressures.

Conflicts of interest

There are no conflicts to declare.

Acknowledgements

The simulations were performed on the supercomputer Mogon from the Zentrum fuer Datenverarbeitung (zdv) at the Johannes Gutenberg University Mainz (hpc.uni-mainz.de), and on the HRLS supercomputing resources (project grant 2DSFG). This project has received funding from the European Union's Horizon 2020 research and innovation programme under grant agreement No. 674979-NANOTRANS and from the Deutsche Forschungsgemeinschaft under the TRR146 project.

References

1 M. Watanabe, M. L. Thomas, S. Zhang, K. Ueno, T. Yasuda and K. Dokko, *Chem. Rev.*, 2017, **117**, 7190–7239.
2 A. A. Minea and S. M. S. Murshed, *Renewable Sustainable Energy Rev.*, 2018, **91**, 584–599.
3 Q. Sheng, Y. Xie, J. Li, X. Wang and J. Xue, *Chem. Commun.*, 2017, **53**, 6125–6127.
4 J. Comtet, A. Niguès, V. Kaiser, B. Coasne, L. Bocquet and A. Siria, *Nat. Mater.*, 2017, **16**, 634–639.
5 A. Lainé, A. Niguès, L. Bocquet and A. Siria, *Phys. Rev. X*, 2020, **10**, 011068.
6 V. Kaiser, J. Comtet, A. Niguès, A. Siria, B. Coasne and L. Bocquet, *Faraday Discuss.*, 2017, **199**, 129–158.
7 S. Ntim and M. Sulpizi, *Phys. Chem. Chem. Phys.*, 2020, **22**, 10786–10791.
8 M. Cai, Q. Yu, W. Liu and F. Zhou, *Chem. Soc. Rev.*, 2020, **49**(21), 7753–7818.
9 C. Ye, W. Liu, Y. Chen and L. Yu, *Chem. Commun.*, 2001, 2244–2245.
10 W. Liu, C. Ye, Q. Gong, H. Wang and P. Wang, *Tribology Letters*, 2002, **13**, 81–85.
11 Q. Lu, H. Wang, C. Ye, W. Liu and Q. Xue, *Tribology International*, 2004, **37**, 547–552.
12 B. Phillips and J. Zabinski, *Tribology Lett.*, 2004, **17**, 533–541.
13 R. Gonzalez, A. Hernandez Battez, D. Blanco, J. Viesca and A. Fernandez-Gonzalez, *Tribology Lett.*, 2010, **40**, 269–277.
14 R. Lhermerout, C. Diederichs and S. Perkin, *Lubricants*, 2018, **6**, 9.
15 A. M. Smith, K. R. J. Lovelock, N. N. Gosvami, T. Welton and S. Perkin, *Phys. Chem. Chem. Phys.*, 2013, **15**, 15317–15320.
16 A. M. Smith, M. A. Parkes and S. Perkin, *J. Phys. Chem. Lett.*, 2014, **5**, 4032–4037.
17 R. Lhermerout and S. Perkin, *Phys. Chem. Chem. Phys.*, 2020, **22**, 455–466.
18 R. Lhermerout and S. Perkin, *Phys. Rev. Fluids*, 2018, **3**, 014201.
19 I. Bitsanis, J. J. Magda, M. Tirrell and H. T. Davis, *J. Chem. Phys.*, 1987, **87**, 1733–1750.
20 S. Bair, C. McCabe and P. T. Cummings, *Phys. Rev. Lett.*, 2002, **88**, 058302.
21 V. Jadhao and M. O. Robbins, *Proc. Natl. Acad. Sci. U. S. A.*, 2017, **114**, 7952–7957.
22 S. Bernardi, B. D. Todd and D. J. Searles, *J. Chem. Phys.*, 2010, **132**, 244706.
23 X. Yong and L. T. Zhang, *J. Chem. Phys.*, 2013, **138**, 084503.
24 R. Khare, J. de Pablo and A. Yethiraj, *J. Chem. Phys.*, 1997, **107**, 2589–2596.
25 J. Lu, T. Reddyhoff and D. Dini, *Tribol. Lett.*, 2018, **66**, 1–16.
26 J. Lu, T. Reddyhoff and D. Dini, *Tribology Lett.*, 2017, **66**, 7.
27 M. D. Marko, J. P. Kyle, Y. S. Wang and E. J. Terrell, *PLoS One*, 2017, **12**, 1–20.
28 J. N. Israelachvili, *J. Colloid Interface Sci.*, 1986, **110**, 263–271.
29 P. A. Thompson and M. O. Robbins, *Phys. Rev. A: At., Mol., Opt. Phys.*, 1990, **41**, 6830–6837.
30 D. M. Heyes, E. R. Smith, D. Dini, H. A. Spikes and T. A. Zaki, *J. Chem. Phys.*, 2012, **136**, 134705.
31 C. Gattinoni, D. M. Heyes, C. D. Lorenz and D. Dini, *Phys. Rev. E: Stat., Nonlinear, Soft Matter Phys.*, 2013, **88**, 052406.
32 S. Maćkowiak, D. M. Heyes, D. Dini and A. C. Brańka, *J. Chem. Phys.*, 2016, **145**, 164704.
33 A. Porras-Vazquez, L. Martinie, P. Vergne and N. Fillot, *Phys. Chem. Chem. Phys.*, 2018, **20**, 27280–27293.
34 D. M. Heyes, E. R. Smith, D. Dini, H. A. Spikes and T. A. Zaki, *J. Chem. Phys.*, 2012, **136**, 134705.
35 A. Shakeel, H. Mahmood, U. Farooq, Z. Ullah, S. Yasin, T. Iqbal, C. Chassagne and M. Moniruzzaman, *ACS Sustainable Chem. Eng.*, 2019, **7**, 13586–13626.
36 M. Moosavi and A. Daneshvar, *J. Mol. Liq.*, 2014, **190**, 59–67.
37 A. Piednoir, A. Steinberger, C. Cottin-Bizonne and C. Barentin, *J. Phys. Chem. B*, 2020, **124**, 2685–2690.
38 T. C. Le, B. D. Todd, P. J. Daivis and A. Uhlherr, *J. Chem. Phys.*, 2009, **131**, 044902.
39 A. V. Mokshin and J.-L. Barrat, *Phys. Rev. E: Stat., Nonlinear, Soft Matter Phys.*, 2008, **77**, 021505.
40 Z. Shao, J. P. Singer, Y. Liu, Z. Liu, H. Li, M. Gopinadhan, C. S. O'Hern, J. Schroers and C. O. Osuji, *Phys. Rev. E: Stat., Nonlinear, Soft Matter Phys.*, 2015, **91**, 020301.
41 J. D. Holbrey and K. R. Seddon, *J. Chem. Soc., Dalton Trans.*, 1999, 2133–2140.
42 J. Nishida, J. P. Breen, B. Wu and M. D. Fayer, *ACS Cent. Sci.*, 2018, **4**, 1065–1073.
43 S. Marion, S. J. Davis, Z.-Q. Wu and A. Radenovic, *Nanoscale*, 2020, **12**, 8867–8874.
44 A. C. F. Mendonça, A. A. H. Pádua and P. Malfreyt, *J. Chem. Theory Comput.*, 2013, **9**, 1600–1610.
45 A. C. F. Mendonça, Y. D. Fomin, P. Malfreyt and A. A. H. Pádua, *Soft Matter*, 2013, **9**, 10606–10616.

46 B. Derjaguin, *Zeitschrift für Physik*, 1934, **88**, 661–675.
47 F. F. Canova, H. Matsubara, M. Mizukami, K. Kurihara and A. L. Shluger, *Phys. Chem. Chem. Phys.*, 2014, **16**, 8247–8256.
48 R. An, X. Qiu, F. U. Shah, K. Riehemann and H. Fuchs, *Phys. Chem. Chem. Phys.*, 2020, **22**, 14941–14952.
49 O. Y. Fajardo, F. Bresme, A. A. Kornyshev and M. Urbakh, *Sci. Rep.*, 2015, **5**(1), 7698.
50 K. Pivnic, F. Bresme, A. A. Kornyshev and M. Urbakh, *ACS Appl. Nano Mater.*, 2020, **3**, 10708–10719.
51 H. Heinz, R. Vaia, B. Farmer and R. Naik, *J. Phys. Chem. C*, 2008, **112**, 17281–17290.
52 I. L. Geada, H. Ramezani-Dakhel, T. Jamil, M. Sulpizi and H. Heinz, *Nat. Commun.*, 2018, **9**(1), 716.
53 V. V. Chaban, I. V. Voroshylova and O. N. Kalugin, *Phys. Chem. Chem. Phys.*, 2011, **13**, 7910–7920.
54 S. Plimpton, *Fast parallel algorithms for short-range molecular dynamics*, Sandia national labs., albuquerque, nm (united states) technical report, 1993.

4

VALIDATION OF THE POLARISABLE GOLD MODEL FOR USE BEYOND PZC

4.1 BACKGROUND AND MOTIVATION

In the preceding chapters, we explored the behaviour and properties of the room temperature ionic liquid [BMIM][BF_4] at the interface with gold, particularly focusing on conditions where the potential of zero charge (PZC) was maintained. These studies provided critical insights into the structural, dynamic and thermodynamic characteristics of [BMIM][BF_4] under equilibrium and non-equilibrium conditions, where the electrostatic forces at the interface are neutral. However, real-world applications often involve scenarios where the system operates away from PZC, necessitating a deeper understanding of how the ionic liquid behaves under such conditions.

In this chapter, we shift our focus to investigating the [BMIM][BF_4]-gold interface under conditions deviating from PZC. This exploration is essential for expanding our knowledge of RTILs in practical applications, where the electric potential at the interface may vary significantly, influencing the ion distribution, structural organisation, and overall interfacial properties. Such scenarios are relevant in various technologies, including energy storage systems, sensors, and catalysis, where the interface between an ionic liquid and a metal surface plays a crucial role.

To approach this complex problem, we first establish the legitimacy of using a polarisable model of gold for simulations and calculations under off-PZC conditions. The polarisable model, as we have seen, allows for a more accurate representation of the electrostatic interactions at the interface. How then may we utilise the polarisable gold model for when the surface charge density is non-zero?

To simplify the investigation and validate our approach, we study a more straightforward system—a NaCl solution at an interface with gold. By analysing this simpler electrolyte-gold interface, we can better understand the fundamental interactions and validate the polarisable model with non-zero surface charge, before applying it to the more complex [BMIM][BF_4] system. The findings from this study serve as a foundation for the subsequent, more intricate analyses of the ionic liquid-gold interface away from PZC.

This chapter presents the methodology, results, and implications of using the polarisable model of gold in simulations involving NaCl solution, providing a critical step towards understanding and accurately modelling the behaviour of [BMIM][BF_4] under off-PZC conditions. The insights gained here will be instrumental in our ongoing efforts to predict and optimise the performance of RTILs in various applications, where control over the interfacial properties is paramount.

4.2 INTRODUCTION TO THE STUDY

4.2.1 *Parallel Plate Capacitor*

In an ideal parallel plate capacitor with just a unit test charge within it, the potential energy would be a combination of the potential energy due to the capacitor empty and

the potential energy of interaction between the test charge and the plates at zero surface charge, as depicted in Figure 25.

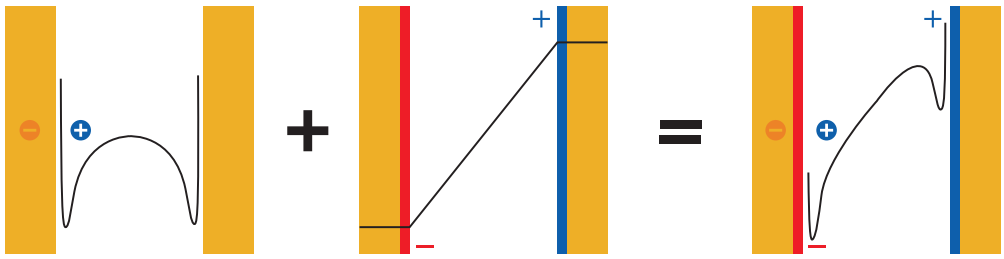

Figure 25: Schematic depiction expected potential energy within the parallel plate capacitor. The blue dots represent a unit test positive charge and its image charge in the metal.

We first verify this for our polarisable gold model by setting up an empty parallel plate capacitor with the model. With a unit test charge inside the capacitor, we move the unit test charge across charged plates of the capacitor and record the corresponding interaction potential energy. An example is shown in Figure 26 where the surface charge density is $\pm 0.061\, e\,\mathrm{nm}^{-2}$. By removing the linear slope in Figure 26 obtained from near the centre,

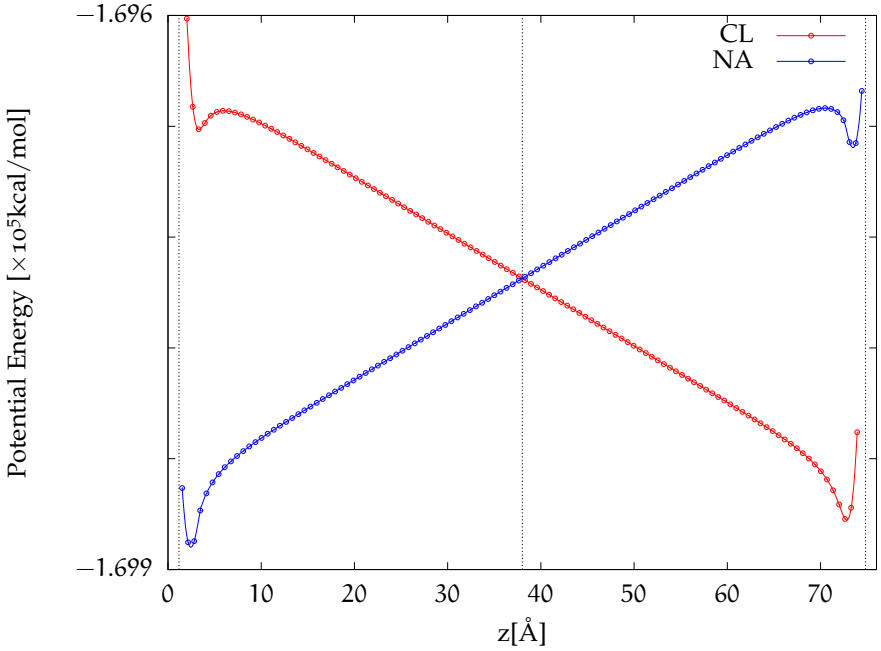

Figure 26: Potential energy of Na (blue) or Cl (red) with $-0.061\, e\,\mathrm{nm}^{-2}$ on left electrode and $0.061\, e\,\mathrm{nm}^{-2}$ on right electrode.

we obtain Figure 27 which is what is expected as the interaction potential between the test charge and the polarisable gold at zero surface charge density.

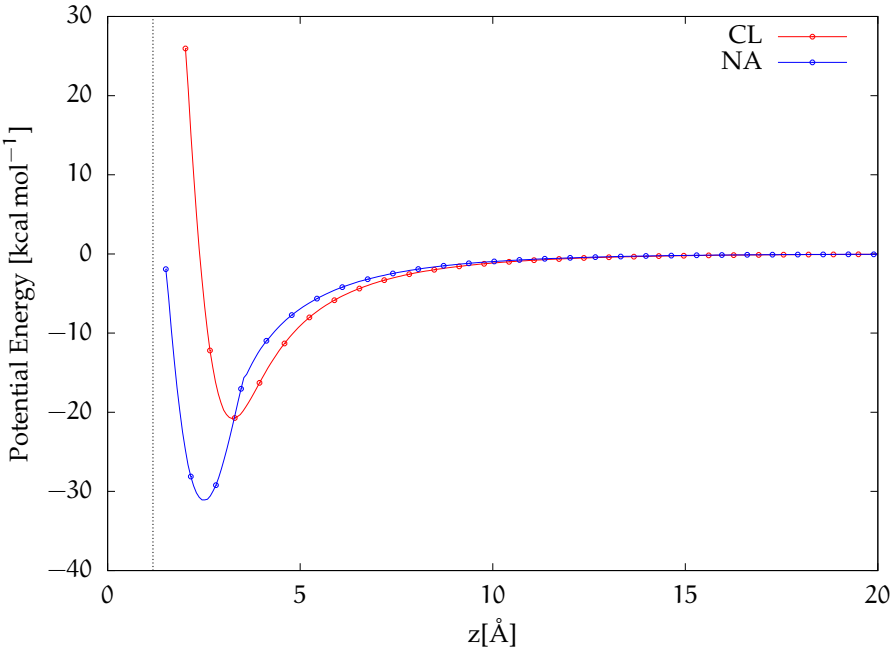

Figure 27: Potential energy of Na (blue) or Cl (red) less the slope in Figure 26

4.2.2 *Poisson potential*

We performed simulations at different surface charge densities. For each surface charge density, the corresponding potential drops were obtained according to the Poisson's equation

$$\Phi = \Phi(\zeta) - \frac{1}{\epsilon_0}\int_{\zeta}^{z} dz' \int_{-\infty}^{z'} dz'' \, \rho_q(z'') \tag{40}$$

where ζ is a reference point in the gold slab whose potential is $\Phi(\zeta)$ and $\rho_q(z)$ is the charge density. Figure 28 shows the potential drops in the NaCl solution for a set of various surface charges on the non-polarisable gold.

In Figure 29 we show that at the cathode, at higher surface charge, the hydrogens of water at the interface form a distinct peak. This suggests a transformation in the orientation of interfacial water, such that the hydrogens point towards the surface. To further establish this, we show in Figure 31 the cosine of the angle between the normal to the surface and the dipole moment of water at varying potentials.

4.3 KEY FINDINGS

This validation study provided several important findings that confirm the usability and suitability and necessity of the polarisable model in off-PZC electrolyte-metal simulations. The following key findings provide a solid foundation for use of the polarisable gold model in more complex systems as [BMIM][BF_4] at charged interfaces. This is particularly import for accurately extending traditional models without heavily suppressing performance.

1. POLARISABILITY OF METAL IS MORE CRUCIAL THAN POLARISABILITY OF WATER: The inclusion of polarisable water did not significantly affect the differential

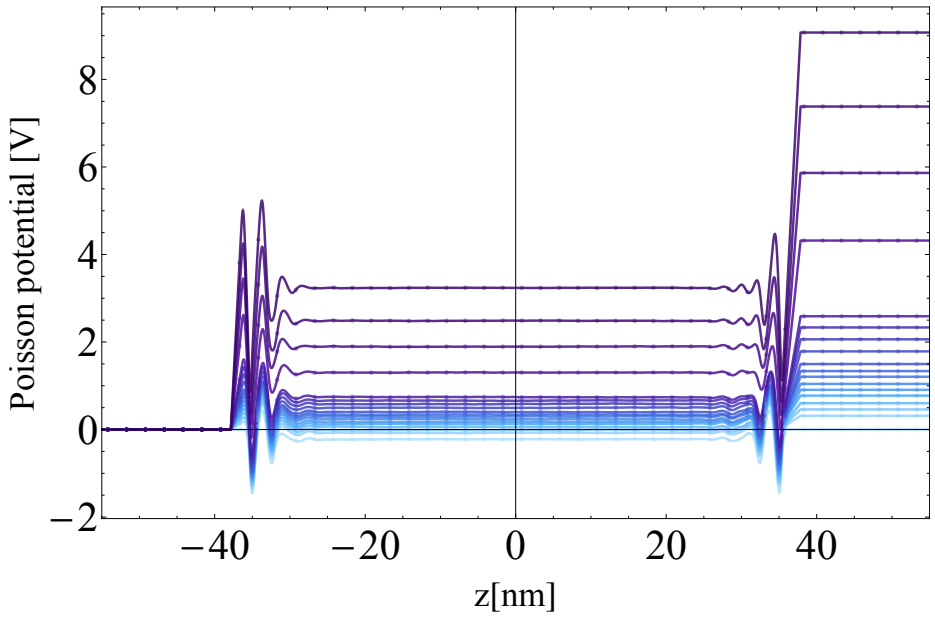

Figure 28: Poisson potential drops at different surface charges at a non-polarisable gold surface. Increasing magnitude of surface charge is shown by increasingly darker lines.

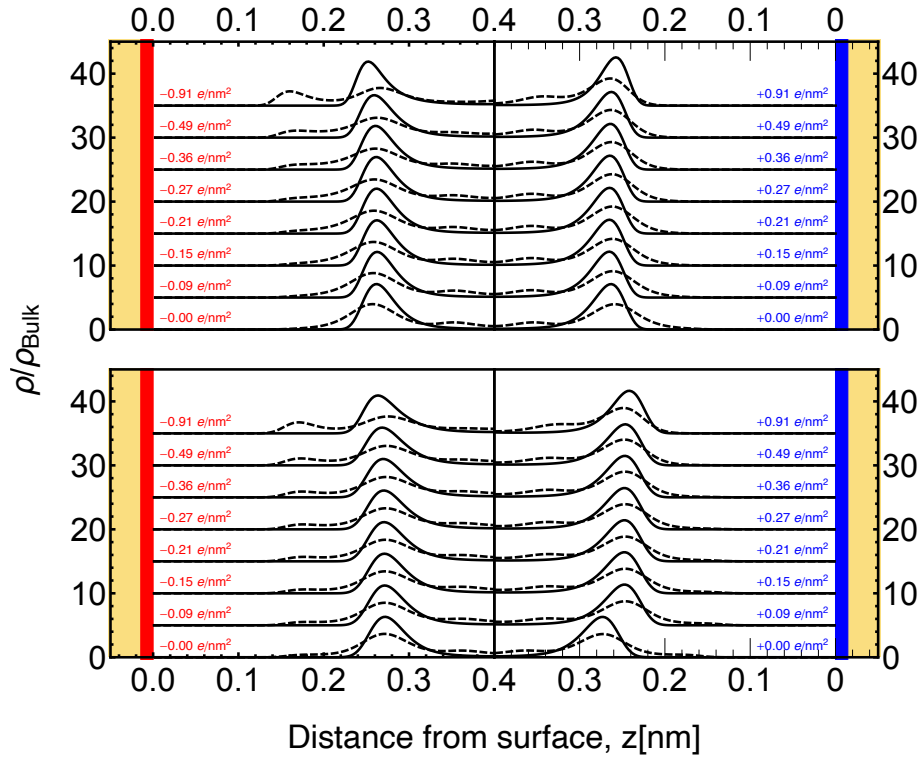

Figure 29: Number densities ρ of O (solid), H (dashed) normalised with their bulk densities ρ_{Bulk}, at the cathode (left) and at the anode (right) at varying surface charge. The top and bottom panels correspond to non-polarisable and polarisable gold respectively. The number densities are shifted up in steps of 5 in ascending surface charge for clarity.

capacitance, suggesting the major role of metal polarisation over water polarisation in enhancing interfacial capacitance. A small difference, however, was observed in

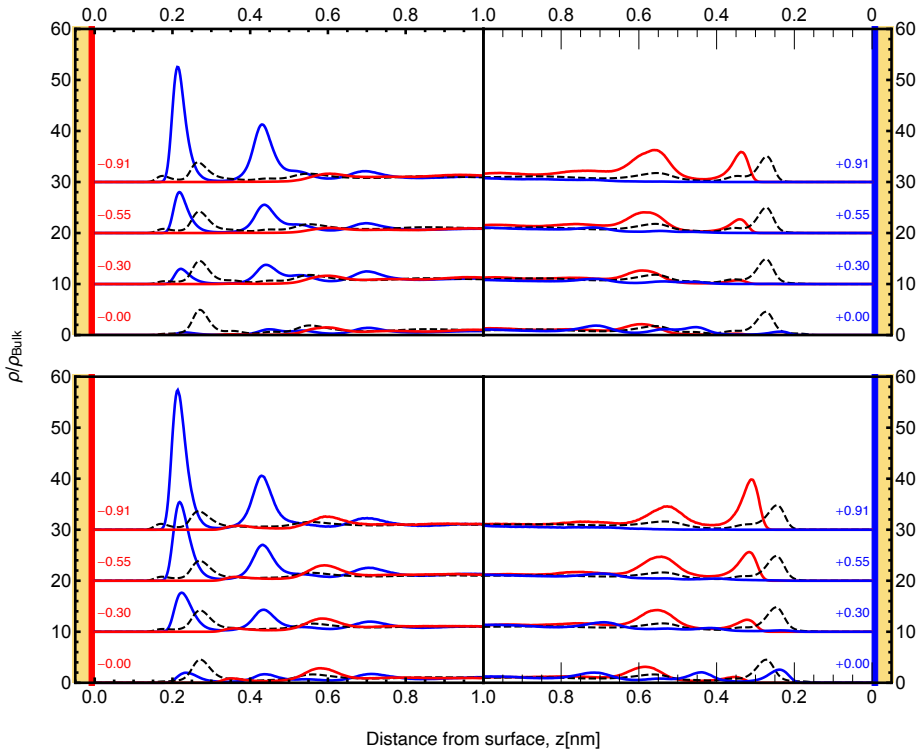

Figure 30: Number densities ρ of Na^+ (blue), Cl^- (red) and water (black, dashed) normalised with their bulk densities ρ_{Bulk}, at the cathode (left, with red surface) and at the anode (right, with blue surface) at varying surface charge in $e\,nm^{-2}$ (shown in small fonts). The top and bottom panels correspond to systems with SWM4-NDP water and SPC/E water respectively, confined in polarisable gold slabs. The number densities are shifted up in steps of 10 in ascending surface charge.

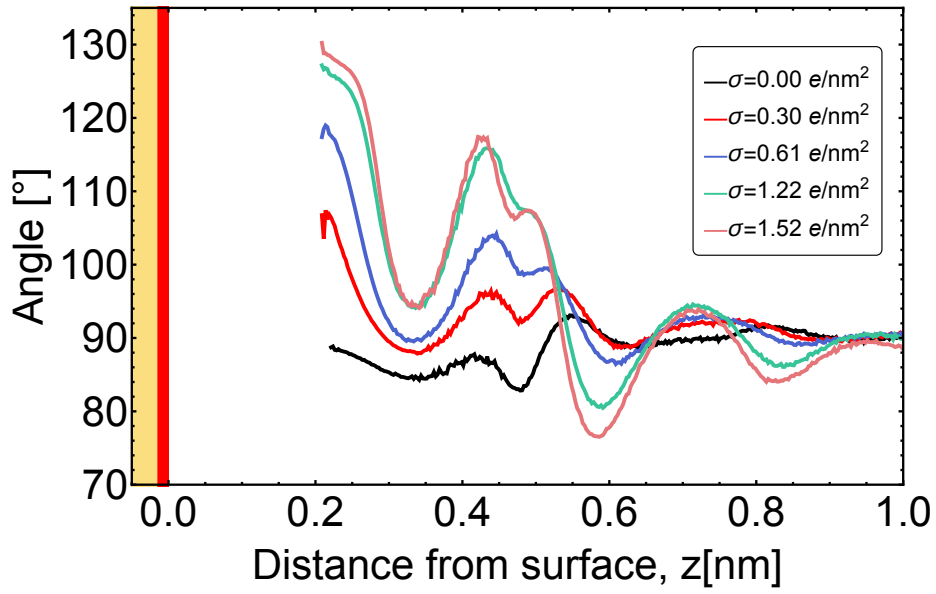

Figure 31: Orientation of water at the cathode of the nonpolarisable gold. The schematic diagrams show how a water molecule may appear at the grid line it is placed on.

the potential of zero charge (PZC), changing from 0.45 V to 0.54 V when SPC/E water was replaced with a polarisable water model.

2. ION AND WATER DENSITY PROFILES:
   - At the cathode, both polarisable and non-polarisable gold models showed that the first layer of ions in contact with the surface was primarily Na^+ ions.
   - In the non-polarisable gold model, there was a formation of a water layer at the first ion layer, while in the polarisable gold model, the first layer of ions was slightly pulled towards the gold surface.
   - The second ion layer exhibited different behaviours between the two gold models, affecting the charging mechanism and differential capacitance.
3. CAPACITANCE MEASUREMENTS:
   - Metal polarisation increased the overall capacitance, with a more significant impact on the negative potential branch.
   - Differential capacitance values for the non-polarisable gold model ranged from $5.1\,\mu F\,cm^{-2}$ to $9.1\,\mu F\,cm^{-2}$, with a peak near the PZC at $-0.8\,V$.
   - For the polarisable gold model, capacitance was found to be more pronounced at the cathodic interface, suggesting a higher charge storage capacity compared to the anodic interface.

4.4 CONCLUSION

The results of this chapter demonstrate that metal polarisation plays a crucial role in enhancing interfacial capacitance, particularly at the cathodic interface. The study provides a detailed atomistic description of the electric double layer and underscores the importance of accurately modelling metal-ion and metal-water interactions in molecular dynamics simulations of electrified interfaces. The results also successfully validate the suitability of the polarisable metal for use beyond PZC.

Volume 25
Number 34
14 September 2023
Pages 22541–23320

PCCP

Physical Chemistry Chemical Physics

rsc.li/pccp

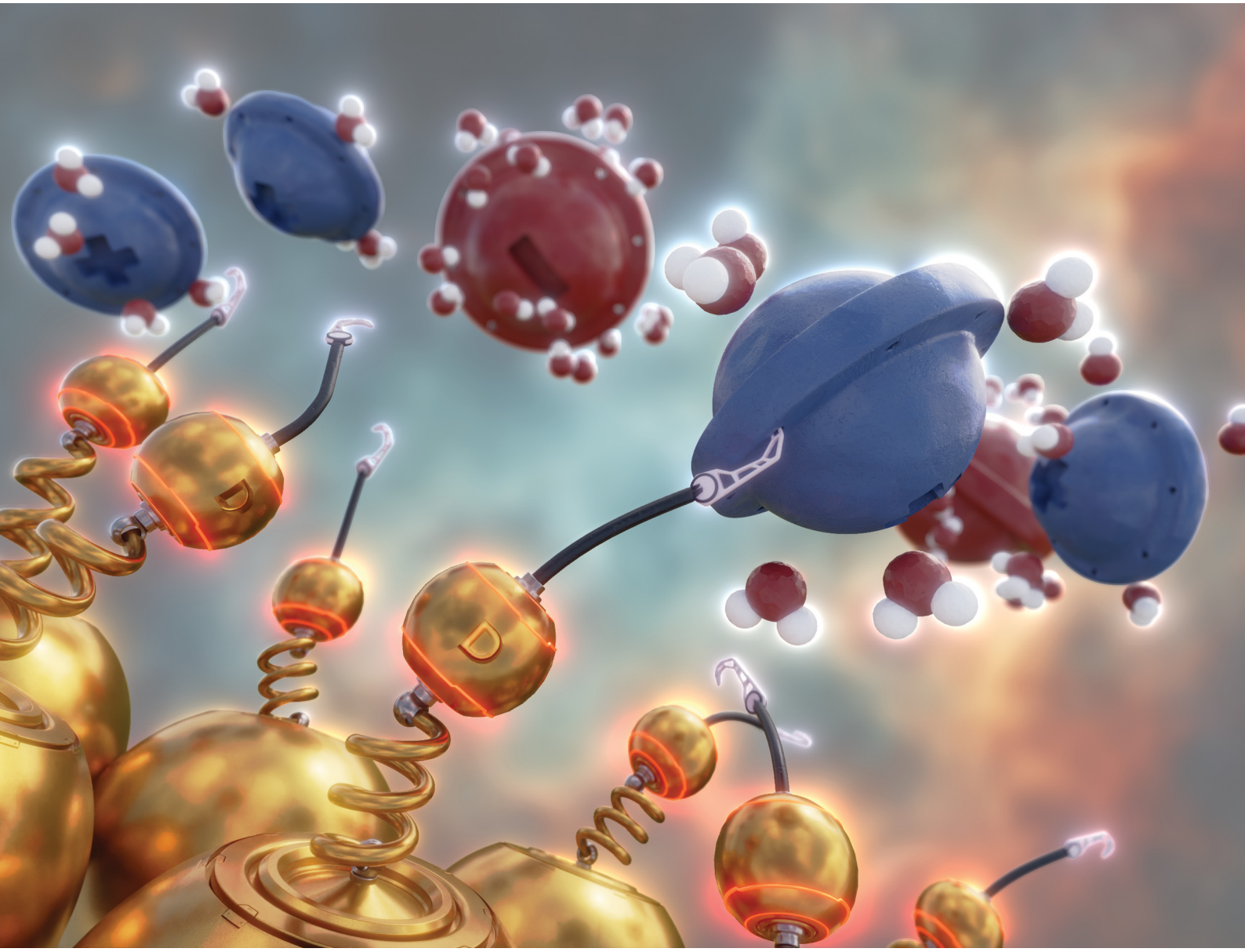

ISSN 1463-9076

ROYAL SOCIETY OF CHEMISTRY

PAPER

Samuel Ntim and Marialore Sulpizi

Molecular dynamics simulations of electrified interfaces including the metal polarisation

PCCP Owner Societies

PCCP

PAPER

Cite this: *Phys. Chem. Chem. Phys.*, 2023, **25**, 22619

Molecular dynamics simulations of electrified interfaces including the metal polarisation†

Samuel Ntim [b] and Marialore Sulpizi *[a]

Received 31st March 2023,
Accepted 17th July 2023

DOI: 10.1039/d3cp01472j

rsc.li/pccp

Understanding electrified interfaces requires an accurate description of the electric double layer which also takes into account the metal polarisation. Here we present a simple approach to the molecular dynamics simulation of electrified interfaces which combines fixed charges and a core–shell model for the description of the polarisable electron density on the metal electrode. The approach has been applied to the Au(111) surface in contact with a NaCl aqueous electrolyte solution in order to calculate the differential capacitance and to gain a detailed picture of the charging mechanism. Metal polarisation enhances the interfacial capacitance with a difference between the cathode and anode. In particular, we find that the influence of the metal polarisation on the electric double layer depends on the ion's solvation shell structure and, for the investigated interface, is more important at the cathode, where it modifies the sodium ion distribution.

1 Introduction

Electrified interfaces are ubiquitous in nature, from large atmospheric and geochemical systems down to microscopic biological systems. The interface between a metal and a liquid electrolyte solution is of particular importance to electrochemical studies and has applications in energy generation, harvesting and storage,[1–3] in electrochemical sensors,[4–6] and even in tribology.[7–9] Significant effort from both the experimental and the theoretical sides has been directed to the understanding of the structure and dynamics at interfaces and in particular to the electrical properties which develop between two different phases.[10] While our theoretical understanding of the electrical structure has been largely through the Electric Double Layer (EDL) model, for most systems the traditional model of the EDL is an oversimplification as it accounts only for ion charge magnitudes.[10,11] This picture breaks down when, for example, effects of asymmetry in ion shapes and sizes, and ion correlations are no longer negligible.[12–14] Not only in such cases have molecular simulations been significant in providing insight,[15,16] but also in cases where polarisation effects are an important consideration.[17,18] At interfaces, molecular simulations have been key in unravelling the microscopic nature of events and have provided detailed knowledge of physical and chemical properties which arise, distinct from bulk.[19–25] Recent quantum mechanical simulations[26] have shown promise in reproducing experimentally measurable quantities like the differential capacitance closer to well known experimental ranges.[27] However, quantum mechanical simulations are still too expensive for investigating fairly large systems and to describe more complex and realistic systems over longer timescales, where instead accurate classical molecular dynamics simulations can still be the method of choice.

Several models have been designed to describe metal polarisation within force field-based atomistic simulation approaches. One option is the so-called constant potential approach,[28–30] where fluctuating charges are assigned to the metal atoms to maintain a constant potential between electrodes.[31–36] Recent works using molecular dynamics simulations at constant potential[37,38] have shown that it is important to provide an accurate description of the "metallicity" of the electrode, beyond the ideal conductor case, to reproduce the experimental results. For example, in ref. 37, Serva *et al.*[37] by tuning the metallicity of the electrode, by way of changing the spread of the Gaussian charges on the electrode atoms, have shown improved results of the differential capacitance. An alternative possibility to include metal polarisation is the use of core–shells as in the model which we have recently introduced[17] and applied to the ionic liquid interface at the potential of zero charge.[24] The model reproduces the classical image potential of adsorbed ions as well as surface, bulk, and aqueous interfacial properties in agreement with experiment.[17] Here we propose an extension of the model to describe variable potential conditions beyond the potential of zero-charge conditions. This is obtained combing our polarisable model with (fixed) additional charges on the electrode surface. The advantage of our

[a] *Institut für Physik, Ruhr Universität Bochum, Universitätstrasse 150, 44801 Bochum, Germany. E-mail: Marialore.Sulpizi@rub.de*
[b] *Institut für Physik, Johannes Gutenberg Universität, Staudingerweg 7, 55128-Mainz, Germany*

† Electronic supplementary information (ESI) available. See DOI: https://doi.org/10.1039/d3cp01472j

model with respect to the traditional fixed charge model is that it allows to include local polarisation effects, such as, for example, those induced by the presence of local charge heterogeneity. In order to test our approach, we investigate a dilute electrolyte solution (1 M) confined between two gold nanoelectrodes of (111) surfaces and calculate the differential capacitance. To systematically increase the degree of complexity we first consider the metal polarisation only, using for water the non-polarisable SPC/E model.[39] In a second step we introduce also water polarisation using the polarisable SWM4-NDP[40] model. An extended discussion on how the results depends on the metal polarisation is also presented.

2 Results and discussion

2.1 Parallel plate capacitor

The model system in our work consists of two gold slabs that confine a NaCl solution (Fig. 1). The metal polarisation is described according to the method introduced in ref. 17 where to each metal atom a pair of a positive core charge $+q$ and a virtual (dummy) electron of negative charge $-q$ are assigned and coupled by a harmonic spring. The virtual electrons carry a mass of 1 a.u. and, in the absence of an external charge, rest at the atomic core. With this mass parameter the dummy electrons have only 0.5% of the mass of gold and move significantly faster than the metal nuclei, which ensure a timescale separation between the dynamics of the virtual electron and of the metal atoms, satisfying the Born–Oppenheimer approximation. The virtual electrons, which can move from their equilibrium position in response to external charges, aim to represent the electron density and are capable of reproducing the image charge potential. In addition to the polarisable dipoles, the surface gold atoms also carry net charges of opposite sign on the two electrodes. As a first step of our approach validation, we have considered the empty capacitor, without the electrolyte solution. When moving a unit positive test charge across the space between the two parallel plates we obtain a potential energy profile which is the sum of the image charge contribution and the linear potential between the plates as depicted in Fig. 2, where we report, as an example, the potential energy for a surface charge density of $\pm 0.061\ e\ \mathrm{nm}^{-2}$. For sake of comparison, in the case of the simple fixed charge model, one would just obtain the simple linear contribution due to the charges on the two parallel plates.

2.2 Interfacial electrostatic potential and differential capacitance

Let's now consider the capacitor containing the electrolyte solution. In Fig. 3 we compare the surface charge as function of the interface electrostatic potential for the polarisable (red line) and non-polarisable (black line) electrodes. In both cases the positive and negative potential branches have different slopes which show a linear behaviour at higher absolute potential values. Such linearity has also been observed in coarse-grained ionic liquids.[41–43] The different slopes are reflected in a difference in the capacitance for their respective electrode potential branches. The differential capacitances are obtained from Fig. 3 using the expression:

$$C_{\mathrm{d}} = \frac{\partial \sigma(\Phi)}{\partial \Phi} \tag{1}$$

where $\Phi = \Phi_{\mathrm{electrode}} - \Phi_{\mathrm{bulk}} - \Phi_{\mathrm{PZC}}$, where $\Phi_{\mathrm{electrode}}$ and Φ_{bulk} are electrostatic potentials at electrode surface and in the liquid bulk respectively. Φ_{PZC} is the potential at zero charge (PZC) also defined as the difference in potential between electrode surface and bulk at $\sigma = 0$. Fig. 4 reports the differential capacitance (again red and black lines for the polarisable and non-polarisable cases respectively). Similar to previous simulations studies, which used LiCl[44] electrolyte solution, the differential capacitance values for the non-polarisable gold model are in the range from 5.1 μF cm^{-2} to 9.1 μF cm^{-2} (taken from the two distinct slopes in Fig. 3) which are lower than what is obtained experimentally,[27] although there is a peak of 10.6 μF cm^{-2} near the PZC, at −0.8 V (*vs.* PZC). From experiments, a potential drop of about 1 V applied across an

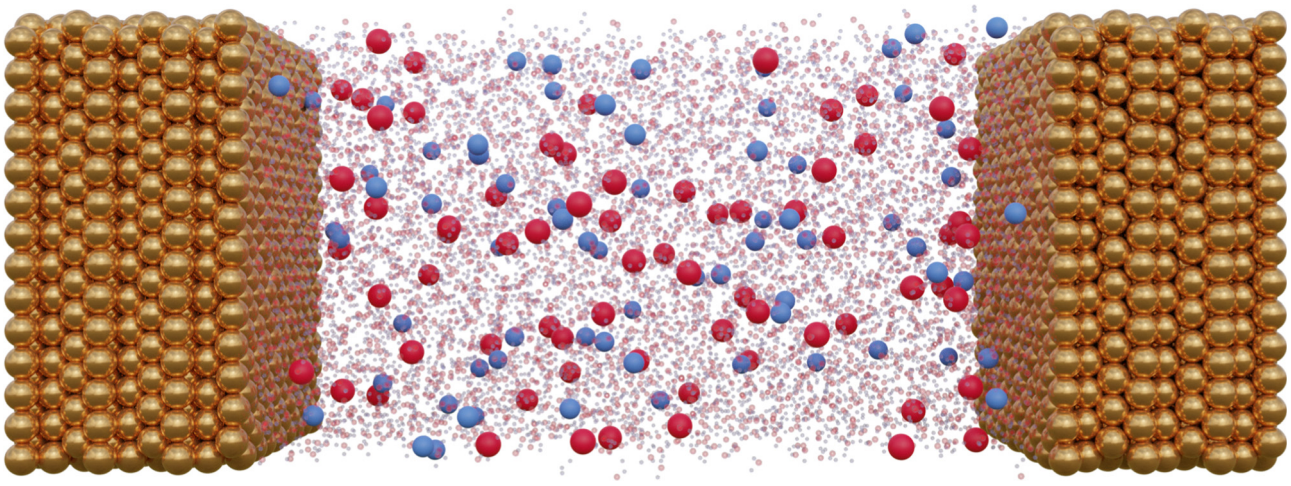

Fig. 1 System of NaCl solution confined in Au(111) constant-charge electrodes. Na^+ ions are represented as blue spheres and Cl^- as red spheres. O and H of water are represented with tiny translucent red and blue spheres respectively.

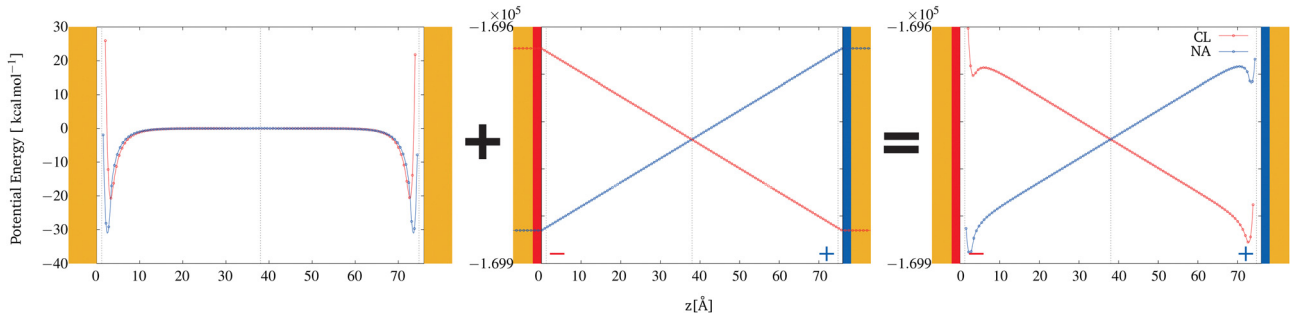

Fig. 2 Total potential energy of Na (blue) or Cl (red) in parallel plates of polarisable gold is a sum of potential energy on the particle in a parallel plate of non-polarisable gold and the potential within the empty parallel plate capacitor of polarisable gold. The plots shown for charged plates have surface charge density of -0.06 e nm^{-2} on left electrode and 0.061 e nm^{-2} on right electrode.

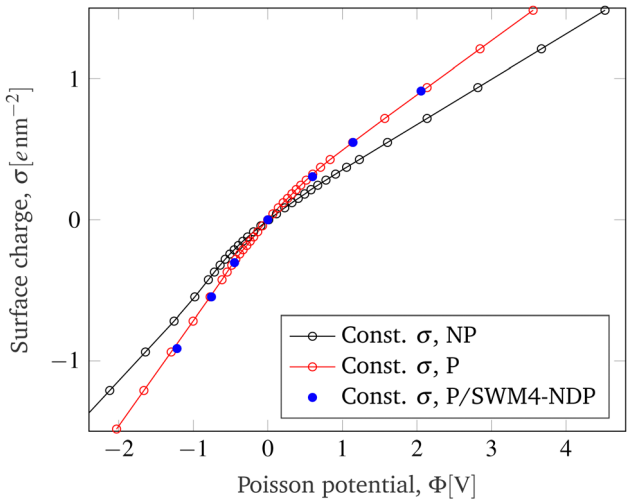

Fig. 3 Surface charge against Poisson potential for 1 M NaCl solution at constant surface-charged non-polarisable gold (black) and polarisable gold (red) electrodes. The blue circles correspond to the NaCl solution with polarisable SWM4-NDP water confined by polarisable gold electrodes.

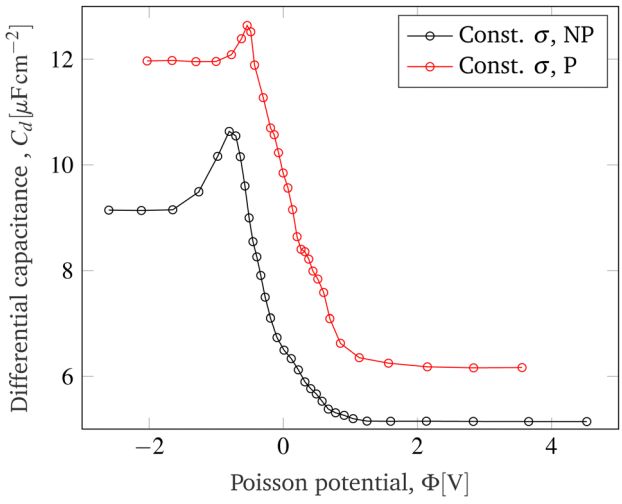

Fig. 4 Differential capacitance for the atomistic simulations of the gold/NaCl-solution interface with the non-polarisable gold model (black) and the polarisable gold model (red).

electrochemical interface such as in this work would yield capacitances between 20 μF cm^{-2} and 50 μF cm^{-2} [27] and even more recently, up to over 100 μF cm^{-2} [45] albeit for a different system. Although still below this range, the metal polarisation, however, increases the overall capacitance, with a slightly larger impact on the negative potential branch. In other words, the metal polarisation has slightly larger impact on the cathodic interface, which can store more charge than at the anodic one.

2.3 Water and ions densities at the interface: the atomistic structure of the double layer

The simulations also permit us to have an atomistic description of the electric double layer and of the impact of the metal polarisation on its structural details. In Fig. 5 we report the ions and water number densities as function of the distance from the Au(111) surface and as function of the different values of the charge (potential) on the electrodes. The first observation is that, at the cathode, for both polarisable and non-polarisable gold models, the first layer of ions in contact with the surface is formed by Na^+. However, for non-polarisable gold (top panel) there is also a formation of a water layer where the first ion layer is formed. At the polarisable gold (bottom panel), on the other hand, the first layer of ions is slightly pulled towards the gold surface. The second aspect, which in conjunction with the first, has a significant impact on the differential capacitance and in the charging mechanism, is that, the ions density in the second layer of Na^+, relative to the first layer, is different for the two gold models. The non-polarisable gold shows a denser second layer, which charges up more strongly than the first layer upon increasing the surface charge. The opposite is true at the polarisable gold, where the first layer is more prominent and has a higher density at higher negative charge. In other words, charging at the cathode predominantly occurs in the first ion layer (and overall more strongly) on the polarisable gold, while it predominantly occurs in the second ion layer on the non-polarisable gold. At the anode, however, there is a similar structure at both gold surfaces, especially at higher surface charge, where there is a consistent film of water

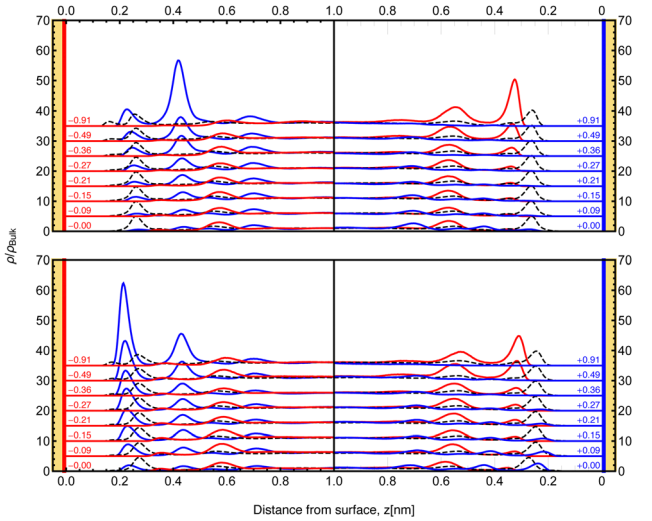

Fig. 5 Number densities ρ of Na^+ (blue), Cl^- (red) and water (black, dashed) normalised with their bulk densities ρ_{Bulk}, at the cathode (left, with red surface) and at the anode (right, with blue surface) at varying surface charge in e nm^{-2} (shown in small fonts). The top and bottom panels correspond to non-polarisable and polarisable gold, respectively. The number densities are shifted up in steps of 5 in ascending surface charge.

between Cl^- ions and the gold surface. We also notice that the behaviour of cathode and anode is not completely symmetric. In particular, we can observe that varying of the interface potential that Cl^- density has two well-defined peaks while no clear structure in the Na^+ is observed. The difference between the two electrodes is a consequence of the difference in the solvation shell of the cation (Na^+) and anion (Cl^-). Both ions strongly coordinate water, however, at PZC, the Na^+ solvation shell is smaller with 5.2 water molecules within its first hydration shell at the interface, while the Cl^- shell is larger with 6.6 molecules at the interface. The higher average number of water molecules solvating Cl^- more effectively screens the image charge interaction at the metal interface, therefore reducing the net Cl^- attraction for the interface. It is also interesting to compare the water structure on cathode and anode as function of the increasing negative and positive potentials respectively. We observe that near and at the PZC, the peaks position in the H and O densities (black dashed lines in Fig. 5) coincide at the interface, with H showing a broader peak than O, suggesting that the water molecules are preserved in an orientation that is in the same plane as the surface of the metal. Previous studies have shown similar structure of water at metal interfaces,[46–51] stabilised by a network of hydrogen bonds between neighbouring water molecules at the interface.[48] Further away from PZC, at the cathode, we can observe that, for sufficiently high values of the applied potential, a second water peak, closer to the gold surface, appears. This is at difference with respect to the case of the anode, where instead the water peak increases, but there is no second peak appearing closer to the metal as the absolute value of the potential increases. In the case of the cathode, the appearance of such a second peak closer to the gold surface is related to a change in the orientation of the water molecules. Upon increasing potential at the cathode, the interfacial water orients such that the hydrogens increasingly point towards the surface. The peak appearing closer to the interface is that formed by the increasing number of hydrogens pointing towards the surface. This is more clearly seen in Fig. S5 in ESI,† which separately shows the water H and O densities, and also in Fig. S7 in ESI,† which shows the angle between the water dipole and the normal to electrode surface. The reorientation of water molecules towards the direction of the field is a known feature upon charging the interface and has been presented even for *ab initio* calculations at Ag(111) surfaces.[46]

2.4 Interface charging mechanisms

The charging of the electrode surface is accompanied by a rearrangement of the solution, which counterbalances the surface charge. There are two competing processes in the charging mechanism at the interface, that determine this rearrangement and therefore the local density at the interface. On the one hand is the adsorption of counter-ions (ions with an opposing charge as the electrode surface charge) and on the other is the desorption of co-ions (ions with charge of the same sign as the electrode surface charge). In order to quantify the relative contribution of the two processes in the charging mechanism, we use the parameter $X(\Phi,\Phi_0)$ introduced in ref. 52. Although the parameter was originally defined for the case of porous carbon electrodes, its use is extended here to characterise the first adlayer of solution at the interface and is defined as:

$$X(\Phi,\Phi_0) = \frac{N(\Phi) - N(\Phi_0)}{(N_{\text{counter}}(\Phi) - N_{\text{co}}(\Phi)) - (N_{\text{counter}}(\Phi_0) - N_{\text{co}}(\Phi_0))} \quad (2)$$

where Φ_0 and Φ are the potentials of zero charge, and of any given surface charge, respectively. $N_{\text{counter}}(\Phi)$, $N_{\text{co}}(\Phi)$ and $N(\Phi)$ are the number of counter-ions, number of co-ions and total number of ions in the first adsorbed layer at a given charging potential Φ. When the counter-ion adsorption is the prevailing process, X is positive, for a perfect ion exchange, $X = 0$, and finally if the co-ion desorption prevails, X is negative. This definition allows X to have any value between -1 and $+1$. In Fig. 6 we have reported the calculated X-parameter within the first layer of solution at the interface during electrode surface charging. As previously shown, the position of the density peaks and their minima, which define the position of the first layer, may slightly depend on the applied potentials. Moreover, due to Na/Cl asymmetry, positive and negative electrode show a different layering. For this reason, in the evaluation of the parameter X, the first layer boundaries are determined separately for each surface charge and for each electrode. As reported in Fig. 6, we find that at the cathode (negative potential) X is $\approx +1.0$ for both polarisable and non-polarisable gold, showing that counter-ion adsorption prevails during charging. On the other hand, at the anode (positive potential), X shows that for lower values of the surface charges, charging occurs predominantly by co-ion desorption. However, the mechanism begins to evolve into a predominantly ion-exchange and then to a counter-ion adsorption mechanism of charging, as the positive charge increases.

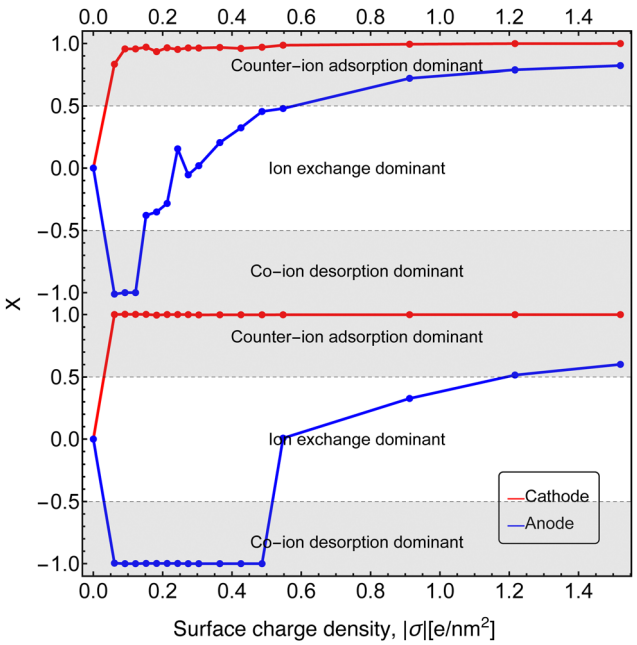

Fig. 6 *X*-Parameter calculated within the first layer of solution at the interface, during charging at the cathode (red) and at the anode (blue) of non-polarisable (top panel) and polarisable (bottom panel) gold respectively.

The difference between the non-polarisable and the polarisable gold systems is that in the absence of polarisation X changes already after $\sigma = 0.122\ e\ \mathrm{nm}^{-2}$ while for the polarisable gold this happens only after $\sigma = 0.487\ e\ \mathrm{nm}^{-2}$. It is worth noting that Na^+ (the cations) are the counter-ions and co-ions at the cathode and the anode, respectively. Therefore, the charging mechanism is primarily driven by the cations and their interplay with other species (water and anions) at the interface.

2.5 Adding water polarisation

In this section, we will discuss the impact of water polarisation on the previous results. For the systems also including polarisable water we have only considered a few selected values for the charge, namely $|\sigma| = 0.0\ e\ \mathrm{nm}^{-2}$, $0.304\ e\ \mathrm{nm}^{-2}$, $0.547\ e\ \mathrm{nm}^{-2}$, $0.912\ e\ \mathrm{nm}^{-2}$. The new data points for the surface charge against Poisson potential are shown as blue circles in Fig. 3. The new data fall on the red curve obtained for the polarisable gold electrodes, also suggesting that the water polarisation does not significantly affect the differential capacitance. A small difference is found for the PZC, which changes from 0.45 V to 0.54 V when the SPC/E water was replaced with a polarisable water. We have also calculated the density profiles for the ions and water in order to compare them with the non-polarisable water cases. A direct comparison is reported in Fig. S6 (ESI†): differences between upper (SWM4-NDP water) and lower (SPC/E water) panels are rather small, with slightly lower peaks for the polarisable water model. The charging parameter for the system including the polarisable water is reported in Fig. S8 (ESI†). The X evolution with the increasing surface charge is very similar to that obtained for SPC/E water, with the onset of the change in the X at the anode at slightly lower charge density.

3 Experimental section

Two systems were simulated, one system with a non-polarisable gold[53] and the other with a polarisable gold.[17] Each system consists of two gold slabs, each made of 9 layers of 224 gold atoms per layer in the (111) plane. The slabs confine 3900 water molecules and 70 pairs of NaCl, giving approximately 1 M NaCl solution in a box of lateral dimensions $L_x = L_y = 4.05457$ nm. The volume was determined by a 1 ns equilibration at a constant number, pressure and temperature. The surface charge at the interface is varied by equally distributing equal but opposite charge on the topmost layers, which are in contact with the solution, of either gold slabs. As for the polarisable gold, the surface charge is distributed on the core, leaving the dummy at a $1e$ charge. For the water molecules the SPC/E force field[39] has been used, while the Lennard-Jones parameters for Na^+ and Cl^- were taken from Dang.[54] We ran, for each surface charge density, a simulation of length 20 ns with a time step of 0.5 fs, collecting coordinates and other relevant system information every 0.5 ps. Each simulation was performed at a constant number, temperature and volume. Temperature was maintained at 298 K using a Nosé–Hoover chain thermostat with three chains and 1 ps time constant. All simulations were performed with the LAMMPS simulation package.[55] For testing the impact of water polarisation on our results, we have also performed a series of simulations where both the metal slabs and the water molecules are treated with polarisable models. In particular, we considered the zero surface charge system and three other values of the surface charges. These additional values for the surface charges were choses to span a broad range of values, and they fall on the linear portions of the charge *versus* potential curve of the polarisable gold system. For each simulated surface charge system, the system was set up from a random distribution of 3900 SWM4-NDP[40] water molecules and 70 pairs of NaCl confined between polarisable gold slabs. The system was maintained at a temperature of 800 K under constant number and pressure for 1 ns with all system charges turned off, and then annealed to 298 K. The box length was fixed to its average value after a 1 ns simulation at constant number, pressure (1 atm) and temperature (298 K). Production runs were performed for at least 20 ns length with time step of 1 fs.

4 Conclusions

We have presented a simple and easily implementable approach to simulating electrified interfaces at the atomistic level, which combines fixed charges on the electrode surface with a core–shell model to describe the metal polarisation. We have used the model to investigate the Au(111) surface in contact with a NaCl electrolyte solution within a wide range of interfacial electrostatic potentials and compared the results to a non-polarisable fixed charge approach. Metal polarisation enhances

the interfacial capacitance, influencing the ions distribution at the electrode/electrolyte interface. In particular, we have found that the double layer structure at the cathode is particularly sensible to the polarisation effects. The asymmetry between cation and anions is possibly due to the difference in their first solvation shell and in the water ability to screen the image charge interaction between the ion and its image charge on the metal plate. Additionally, treating the water with a polarisable model does not modify the results obtained for the polarisable metal, suggesting that the metal polarisation has a major role in increasing the interface capacitance with respect to the water polarisation. Our results are again a confirmation that the double layer structure is the result of a delicate balance between the metal–ion, metal–water, ion–water interactions, and therefore it is of uttermost importance to have an accurate description of all these components in the atomistic simulations. Our approach provides a simple, computationally inexpensive means to include metal polarisation at electrified interfaces, which can be easily used in all atomistic simulation packages and which can help to provide a more accurate description of the metal/water interface.

Conflicts of interest

There are no conflicts to declare.

Acknowledgements

The simulations were performed on the supercomputer Mogon from the Zentrum fuer Datenverarbeitung (zdv) at the Johannes Gutenberg University Mainz (hpc.uni-mainz.de), and on the HRLS supercomputing resources (project grant 2DSFG). This project has received funding from the European Union's Horizon 2020 research and innovation programme under grant agreement No 674979-NANOTRANS and from the Deutsche Forschungsgemeinschaft under the TRR146 project. This work also funded by the Deutsche Forschungsgemeinschaft (DFG, German Research Foundation) under Germany's Excellence Strategy-EXC 2033-390677874-RESOLV.

References

1 J. B. Goodenough and Y. Kim, *Chem. Mater.*, 2010, **22**, 587–603.
2 M. Salanne, B. Rotenberg, K. Naoi, K. Kaneko, P.-L. Taberna, C. P. Grey, B. Dunn and P. Simon, *Nat. Energy*, 2016, **1**, 1–10.
3 T. Bak, J. Nowotny, M. Rekas and C. C. Sorrell, *Int. J. Hydrogen Energy*, 2002, **27**, 991–1022.
4 K. Białas, D. Moschou, F. Marken and P. Estrela, *Microchim. Acta*, 2022, **189**, 172.
5 Y. Shao, J. Wang, H. Wu, J. Liu, I. A. Aksay and Y. Lin, *Electroanalysis*, 2010, **22**, 1027–1036.
6 M. Shiran Chaharsoughi, J. Edberg, P. Andersson Ersman, X. Crispin, D. Zhao and M. P. Jonsson, *npj Flexible Electron.*, 2020, **4**, 1–7.
7 G. Xie, D. Guo and J. Luo, *Tribol. Int.*, 2015, **84**, 22–35.
8 H. A. Spikes, *Tribol. Lett.*, 2020, **68**, 90.
9 R. B. Waterhouse, *Tribology*, 1970, **3**, 158–162.
10 R. Parsons, *Chem. Rev.*, 1990, **90**, 813–826.
11 J. Wu, *Chem. Rev.*, 2022, **122**, 10821–10859.
12 A. A. Kornyshev, *J. Phys. Chem. B*, 2007, **111**, 5545–5557.
13 M. Fedorov, N. Georgi and A. Kornyshev, *Electrochem. Commun.*, 2010, **12**, 296–299.
14 A. A. Kornyshev, N. B. Luque and W. Schmickler, *J. Solid State Electrochem.*, 2014, **18**, 1345–1349.
15 K. Breitsprecher, P. Košovan and C. Holm, *J. Phys.: Condens. Matter*, 2014, **26**, 284108.
16 K. Breitsprecher, P. Košovan and C. Holm, *J. Phys.: Condens. Matter*, 2014, **26**, 284114.
17 I. L. Geada, H. Ramezani-Dakhel, T. Jamil, M. Sulpizi and H. Heinz, *Nat. Commun.*, 2018, **9**, 716.
18 C. Y. Son and Z.-G. Wang, *Proc. Natl. Acad. Sci. U. S. A.*, 2021, **118**, e2020615118.
19 J. Vatamanu, L. Cao, O. Borodin, D. Bedrov and G. D. Smith, *J. Phys. Chem. Lett.*, 2011, **2**, 2267–2272.
20 C. Merlet, B. Rotenberg, P. A. Madden, P.-L. Taberna, P. Simon, Y. Gogotsi and M. Salanne, *Nat. Mater.*, 2012, **11**, 306–310.
21 P. Wu, J. Huang, V. Meunier, B. G. Sumpter and R. Qiao, *J. Phys. Chem. Lett.*, 2012, **3**, 1732–1737.
22 J. Vatamanu, O. Borodin and G. D. Smith, *J. Am. Chem. Soc.*, 2010, **132**, 14825–14833.
23 Z. Hu, J. Vatamanu, O. Borodin and D. Bedrov, *Phys. Chem. Chem. Phys.*, 2013, **15**, 14234–14247.
24 S. Ntim and M. Sulpizi, *Phys. Chem. Chem. Phys.*, 2020, **22**, 10786–10791.
25 S. Ntim and M. Sulpizi, *Phys. Chem. Chem. Phys.*, 2021, **23**, 24357–24364.
26 Z. K. Goldsmith, M. F. C. Andrade and A. Selloni, *Chem. Sci.*, 2021, **12**, 5865–5873.
27 D. M. Kolb, *Surf. Sci.*, 2002, **500**, 722–740.
28 J. I. Siepmann and M. Sprik, *J. Chem. Phys.*, 1995, **102**, 511–524.
29 S. K. Reed, O. J. Lanning and P. A. Madden, *J. Chem. Phys.*, 2007, **126**, 084704.
30 Z. Wang, Y. Yang, D. L. Olmsted, M. Asta and B. B. Laird, *J. Chem. Phys.*, 2014, **141**, 184102.
31 T. Gingrich, *Master's thesis*, Oxford University, Oxford, 2010.
32 A. Marin-Laflèche, M. Haefele, L. Scalfi, A. Coretti, T. Dufils, G. Jeanmairet, S. K. Reed, A. Serva, R. Berthin, C. Bacon, S. Bonella, B. Rotenberg, P. A. Madden and M. Salanne, *J. Open Source Software*, 2020, **5**, 2373.
33 A. Coretti, C. Bacon, R. Berthin, A. Serva, L. Scalfi, I. Chubak, K. Goloviznina, M. Haefele, A. Marin-Laflèche, B. Rotenberg, S. Bonella and M. Salanne, *J. Chem. Phys.*, 2022, **157**, 184801.
34 G. Jeanmairet, B. Rotenberg and M. Salanne, *Chem. Rev.*, 2022, **122**, 10860–10898.
35 L. Scalfi, M. Salanne and B. Rotenberg, *Annu. Rev. Phys. Chem.*, 2021, **72**, 189–212.
36 L. Scalfi, T. Dufils, K. G. Reeves, B. Rotenberg and M. Salanne, *J. Chem. Phys.*, 2020, **153**, 174704.
37 A. Serva, L. Scalfi, B. Rotenberg and M. Salanne, *J. Chem. Phys.*, 2021, **155**, 044703.

38 G. Pireddu, L. Scalfi and B. Rotenberg, *J. Chem. Phys.*, 2021, **155**, 204705.
39 H. J. C. Berendsen, J. R. Grigera and T. P. Straatsma, *J. Phys. Chem.*, 1987, **91**, 6269–6271.
40 G. Lamoureux, E. Harder, I. V. Vorobyov, B. Roux and A. D. MacKerell, *Chem. Phys. Lett.*, 2006, **418**, 245–249.
41 C. Merlet, M. Salanne, B. Rotenberg and P. A. Madden, *J. Phys. Chem. C*, 2011, **115**, 16613–16618.
42 C. Merlet, M. Salanne, B. Rotenberg and P. A. Madden, *Electrochim. Acta*, 2013, **101**, 262–271.
43 C. Merlet, M. Salanne and B. Rotenberg, *J. Phys. Chem. C*, 2012, **116**, 7687–7693.
44 A. P. Willard, S. K. Reed, P. A. Madden and D. Chandler, *Faraday Discuss.*, 2008, **141**, 423–441.
45 K. Ojha, N. Arulmozhi, D. Aranzales and M. T. M. Koper, *Angew. Chem., Int. Ed.*, 2020, **59**, 711–715.
46 C. G. Sánchez, *Surf. Sci.*, 2003, **527**, 1–11.
47 A. Michaelides, V. A. Ranea, P. L. de Andres and D. A. King, *Phys. Rev. Lett.*, 2003, **90**, 216102.
48 D. T. Limmer, A. P. Willard, P. Madden and D. Chandler, *Proc. Natl. Acad. Sci. U. S. A.*, 2013, **110**, 4200–4205.
49 A. Huzayyin, J. H. Chang, K. Lian and F. Dawson, *J. Phys. Chem. C*, 2014, **118**, 3459–3470.
50 J. M. Fischer, D. Mahlberg, T. Roman and A. Groß, *Proc. R. Soc. A*, 2016, **472**, 20160618.
51 S. Park and J. G. McDaniel, *J. Phys. Chem. C*, 2022, **126**, 16461–16476.
52 A. C. Forse, C. Merlet, J. M. Griffin and C. P. Grey, *J. Am. Chem. Soc.*, 2016, **138**, 5731–5744.
53 H. Heinz, R. Vaia, B. Farmer and R. Naik, *J. Phys. Chem. C*, 2008, **112**, 17281–17290.
54 L. X. Dang, *J. Am. Chem. Soc.*, 1995, **117**, 6954–6960.
55 A. P. Thompson, H. M. Aktulga, R. Berger, D. S. Bolintineanu, W. M. Brown, P. S. Crozier, P. J. in't Veld, A. Kohlmeyer, S. G. Moore, T. D. Nguyen, R. Shan, M. J. Stevens, J. Tranchida, C. Trott and S. J. Plimpton, *Comput. Phys. Commun.*, 2022, **271**, 108171.

5

IMPROVING THE DIFFERENTIAL CAPACITANCE OF CONFINED ELECTROLYTES

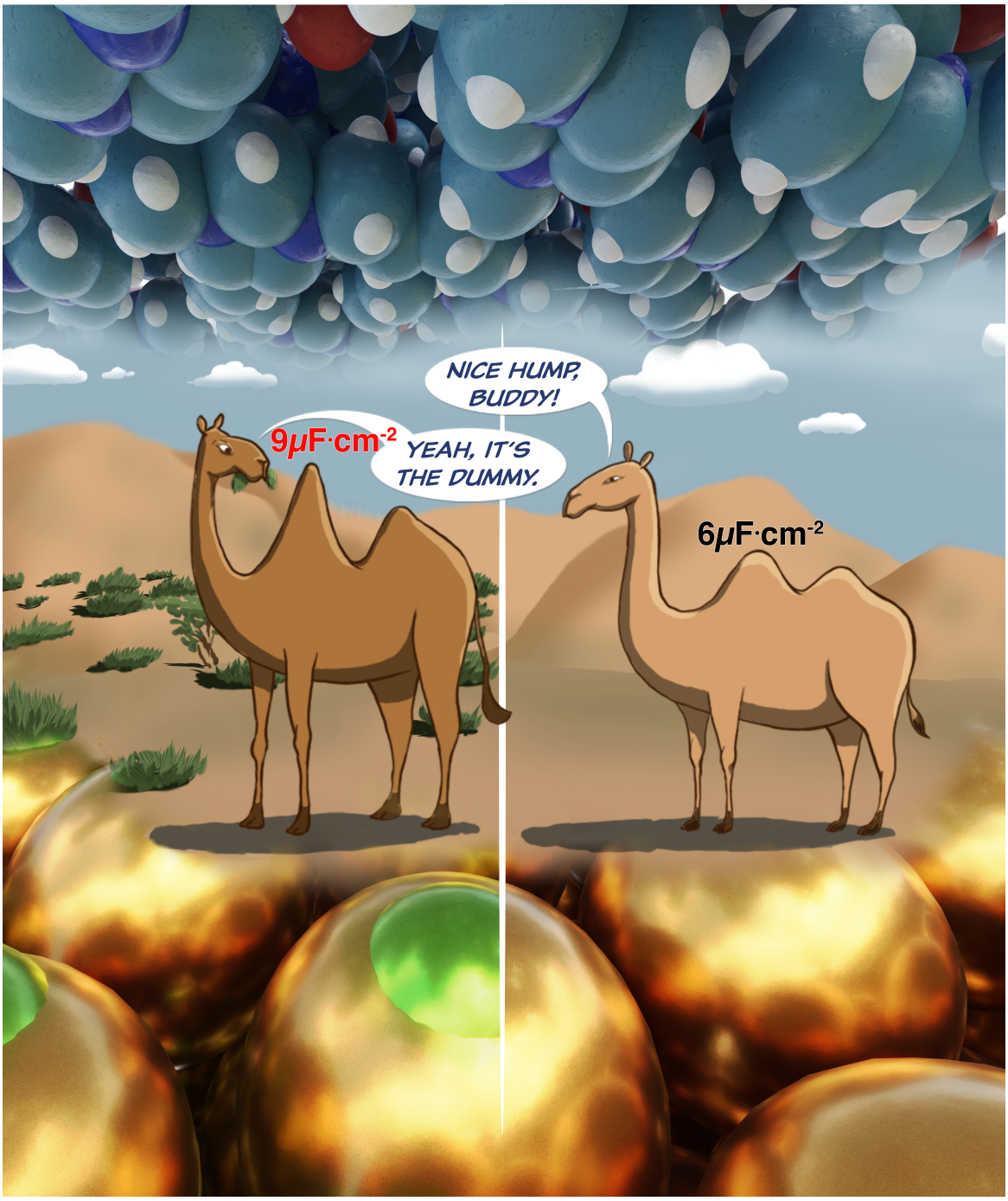

5.1 BACKGROUND AND MOTIVATION

Research in electrochemical systems has increasingly focused on the behaviour of ionic liquids (ILs) at electrified interfaces due to their unique properties and potential applications in energy storage devices, such as supercapacitors and batteries. Ionic liquids, characterised by their low volatility, high thermal stability, and wide electrochemical window, have emerged as promising candidates for electrolytes in these applications [164]. A critical aspect of understanding and optimising these systems is the study of the electric double layer (EDL) at the interface between the electrode and the ionic liquid. The structure and dynamics of the EDL significantly influence the overall performance of electrochemical devices [165]. Recent studies have shown that the differential capacitance of the EDL, which quantifies the ability of the interface to store charge, can exhibit complex behaviour depending on the properties of the ionic liquid and the nature of the electrode surface [151]. Traditional models often fail to capture the intricacies of these systems, necessitating advanced approaches that incorporate the polarisable nature of both the ionic liquid and the electrode.

Having validated the polarisable gold model in chapter 4, we now apply this model to study the behaviour of [BMIM][BF_4] at a charged gold interface. In earlier chapters, we explored the equilibrium and non-equilibrium behaviour of the RTIL at a neutral interface, providing insights into the baseline structural and dynamical properties. However, in practical applications, metal surfaces often carry a charge, which significantly alters the behaviour of the IL at the interface.

This chapter delves into interfacial phenomena beyond the traditional model. The motivation for this chapter is to understand how charging the gold surface, coupled with inclusion of image charges, influences the interfacial properties of [BMIM][BF_4]. This is particularly relevant for devices like supercapacitors and batteries, where the performance depends on the ability to control the electric double layer and the associated charge storage mechanisms. This chapter is to provide critical insights for optimising these technologies.

5.2 INTRODUCTION TO THE STUDY

5.2.1 *MD Simulation details*

We perform constant surface charge simulations by evenly distributing charge on the surface gold atoms. In the case of our polarisable gold model, the charge may be placed on either the core or on the dummy. Given a surface charge density σ, mass of a gold atom m, gold surface area A and number of surface gold atoms N_s, Figure 32 shows how the charge on each gold atom is defined, subscripts c and d corresponding to core and dummy respectively. The full list of parameters for the polarisable gold is reported in Ref. 149.

5.2.2 *Potential calculation and differential capacitance*

The potentials are calculated as

$$\Phi = \Phi_{electrode} - \Phi_{bulk} - \Phi_{PZC}. \tag{41}$$

$\Phi_{electrode}$ in Equation 41 is the potential of a chosen point in the electrode and is straightforwardly chosen to be any point within the traditional gold electrodes. On our po-

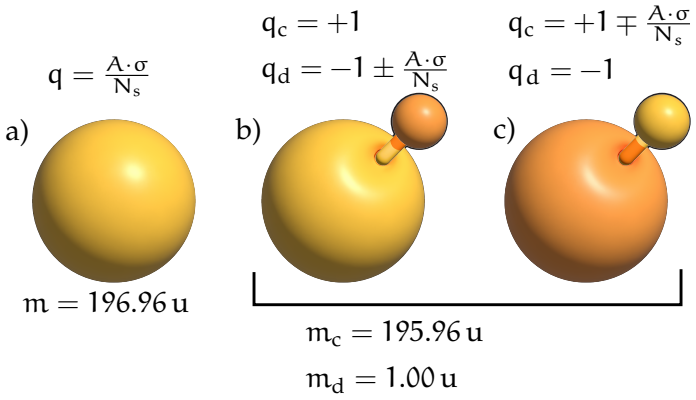

Figure 32: Gold models and the method charging. a) Traditional gold; b) polarisable gold with excess charge on dummy; c) polarisable gold with excess charge on core.

Table 7: Differential capacitance peaks.

	$\sigma/e\,\text{Å}^{-2}$	Φ/V	C_d/nm
	Peak at cathode		
Non-polarisable gold	−0.3678	−1.498	5.977
Polarisable gold (PC)	−0.3678	−1.265	8.738
Polarisable gold (PD)	−0.3678	−1.281	8.061
	Peak at anode		
Non-polarisable gold	0.5926	2.309	5.328
Polarisable gold (PC)	0.6846	2.223	6.741
Polarisable gold (PD)	0.5926	2.021	7.185

larisable gold, however, it is important to exclude the artefact of internally created double layer. We do so by setting $\Phi_{electrode}$ to the potential at the surface of the electrode, determined by the spheres occupied by the surface gold core-dummy pairs.

Figure 33 shows the surface charge density versus potential curves. Note the similarity between the curves for the polarisable with charge-on-core and charge-on-dummy models. The differential capacitance is calculated as the derivative of the surface charge density σ as function of potential, Φ. We use the Savitzky-Golay smoothing algorithm to smooth the function before taking the derivative. Differential capacitance curves for charge-on-core and charge-on-dummy models are shown in Figure 34 where the two give identical results. Table 7 reports on the two differential capacitance peaks found in all systems.

5.2.3 *Ion densities and X parameters*

The calculation of X parameters were performed in the region within 3.8 Å off the surface of the gold slabs. This region is so chosen to include only the first density peaks from the surfaces. To show the impact of the cut-off on the X parameter we have reported in Figure 35 the comparison between cut-off values of 3.8 Å (top panel) and 5 Å (bottom panel). Figure 36 shows the total ion number densities at different surface charge densities for

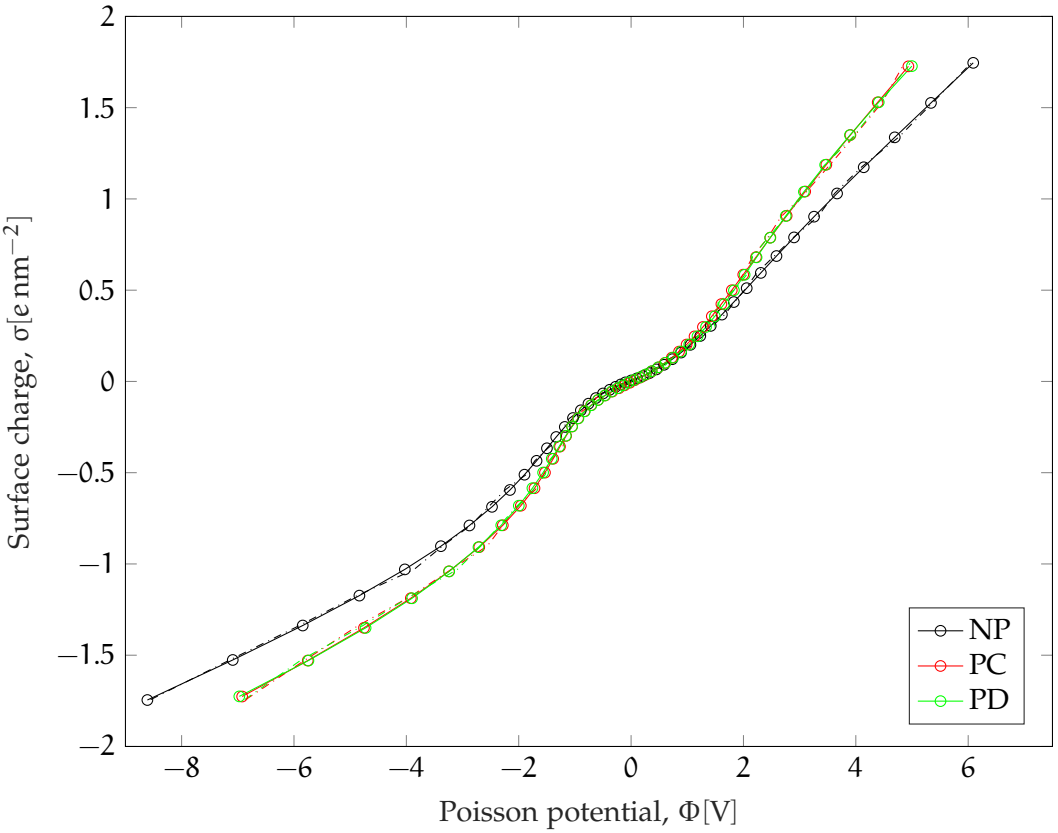

Figure 33: Surface charge density as function of electrostatic potential. Dashed lines correspond to the actual data while solid lines correspond to the smoothed data. NP, PC and PD are for traditional, polarisable with charge-on-core and polarisable with charge-on-dummy models.

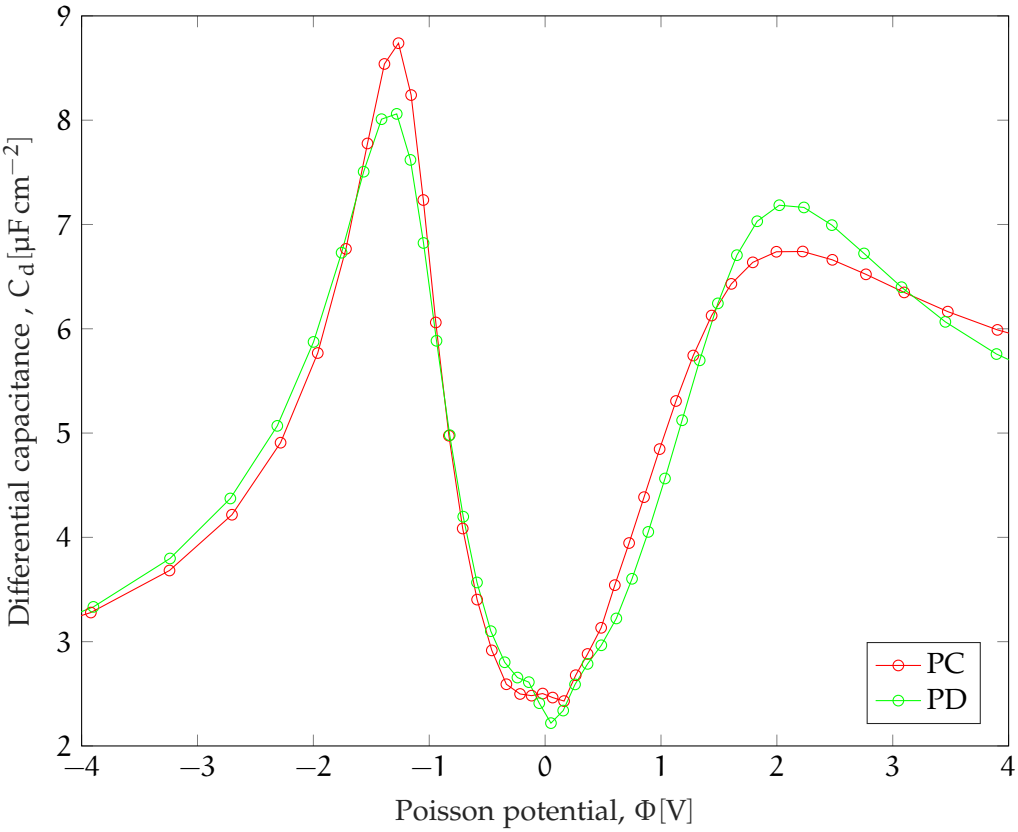

Figure 34: Differential capacitance curves comparing charge-on-core (PC) to charge-on-dummy (PD) systems.

atomistic ionic liquid on polarisable gold (charge-on-core). The plots are shifted vertically for clarity and the vertical line marks the end of the region within with X parameters were calculated. Figure 37 shows the evolution of the ions density with respect to changing surface charge.

5.2.4 *Orientation of cations at interface*

We show here the orientation of the cation at the interface for atomistic ionic liquid on traditional gold (Figures 39 and 40). Comparing ϕ distributions of Figure 39 and Figure 3 of this chapter's article, we find that the butyl tail in the former does not have as much tendency to raise at higher potentials as the latter. Nevertheless, similar orientational adjustments are made in order to accommodate more cations at the interface with traditional gold.

5.3 OBJECTIVES

Despite significant advancements in the study of ionic liquids at electrified interfaces, several gaps remain. Traditional non-polarisable models of electrodes often do not account for the image charge effects that are crucial in accurately describing the EDL structure and dynamics. Moreover, the influence of ion size, shape, and specific adsorption phenomena on the differential capacitance remains inadequately understood [166]. Addressing these gaps is essential for optimising the design and performance of electrochemical capacitors and other related technologies.

The objectives of this chapter were:

- To investigate the structural organisation of [BMIM][BF_4] at a charged gold interface with image charge inclusion
- To analyse the effect of a charged interface on the EDL and the nature of the differential capacitance of the RTIL.
- To study the dynamical properties, including ion mobility and liquid viscosity at the interface, under charged conditions.
- To investigate the method of ion-charging the interface both at the anode and cathode.

5.4 KEY FINDINGS

The study reveals several significant findings regarding the structure and dynamics of the EDL at the gold electrode/[BMIM][BF4] interface:

- ELECTRIC DOUBLE LAYER STRUCTURE: The polarisable model results in a more detailed and accurate depiction of the EDL structure. The inclusion of image charges enhances the ion density in the double layer, particularly around the maxima of the differential capacitance curve.
- DIFFERENTIAL CAPACITANCE SHAPE: The differential capacitance exhibits a double bell (camel) shape, attributed to the polarisation effects of the metal electrode. This shape is indicative of complex ion adsorption and desorption processes at the interface.

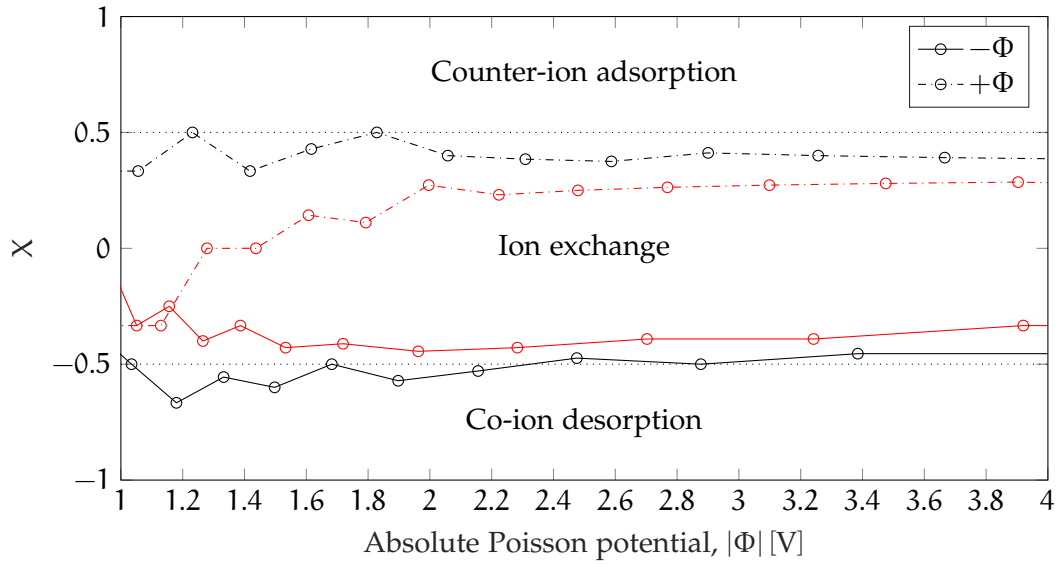

(a) The X parameters calculated within 3.8 Å from gold surface as function of the interface potential.

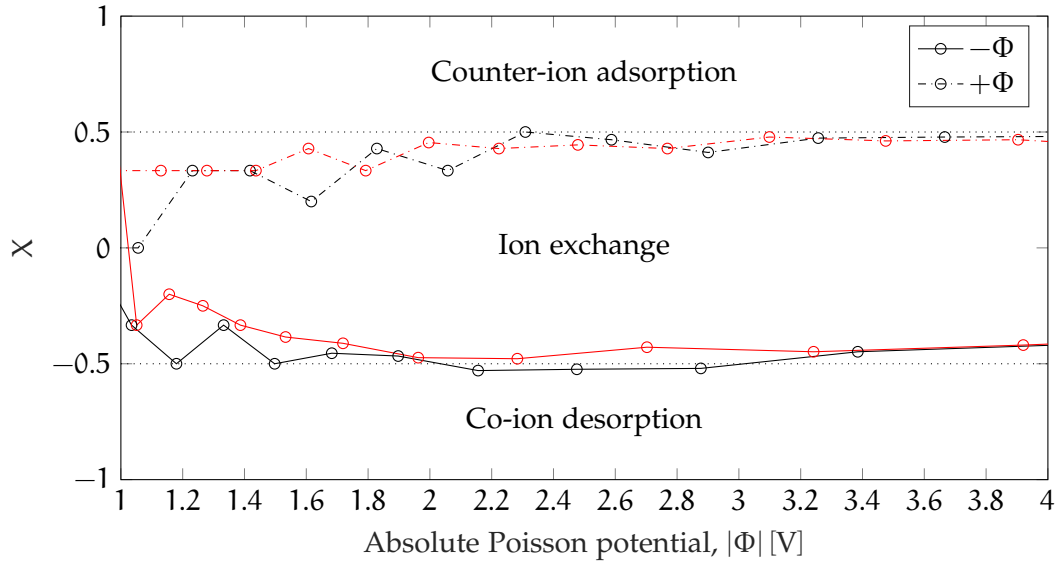

(b) The X parameters calculated within 5 Å from gold surface as function of the interface potential.

Figure 35: X parameter at interface. Black and red lines are for non-polarisable and polarisable gold models, respectively, while solid and dashed lines are for negative and positive potentials (or surface charge densities). Horizontal dotted lines indicate boundaries separating the various charging mechanisms.

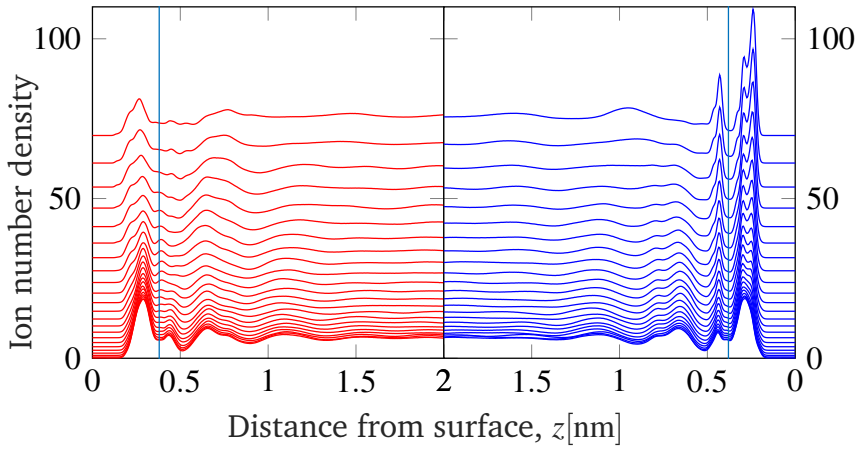

Figure 36: Ionic liquid number density within the first 2 nm from electrode surfaces, and for all charge densities, Plots are shifted vertically by 20 times their charge densities, for clarity. The first peaks from the gold surfaces fall within 3.8 Å, shown with the vertical line.

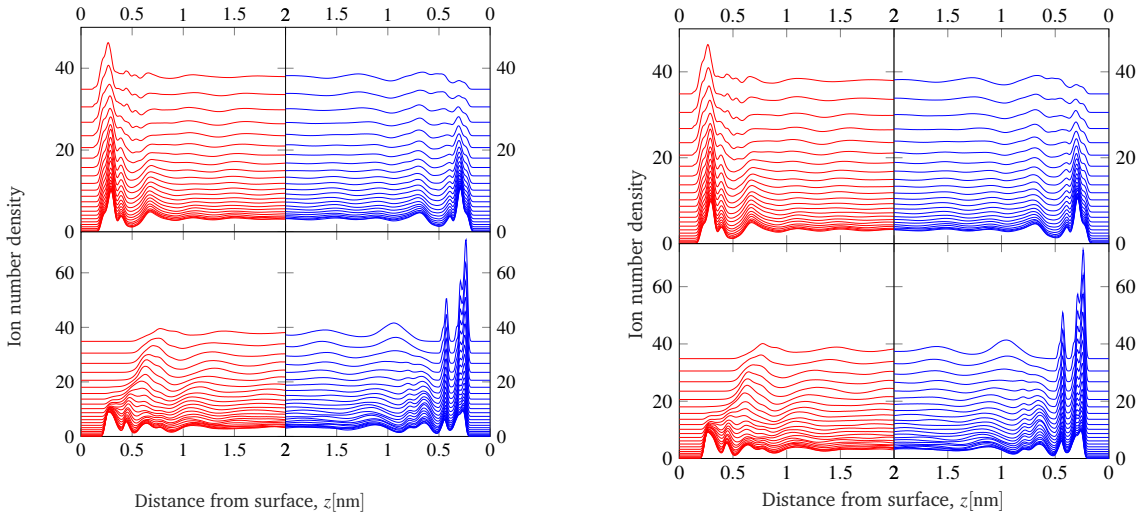

(a) (b)

Figure 37: Ionic liquid number density within the first 2 nm from electrode surfaces for all charge densities. The left panel is for traditional gold while the right panel is for polarisable gold. In each panel the top is for cations and the bottom is for anions, while the left (red) and right (blue) correspond to cathode and anode respectively.

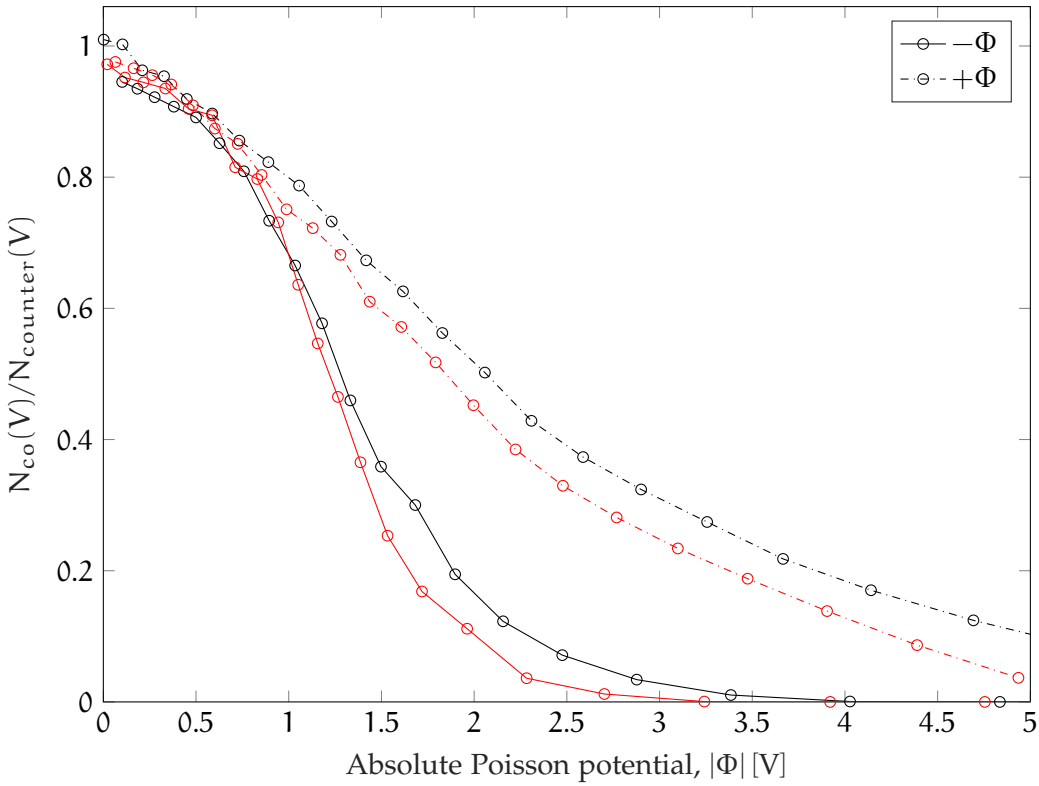

Figure 38: Ratio of ion numbers within 3.8 Å. Black and red lines are for traditonal and polarisable gold respectively, while solid and dashed lines are for negative and positive potentials.

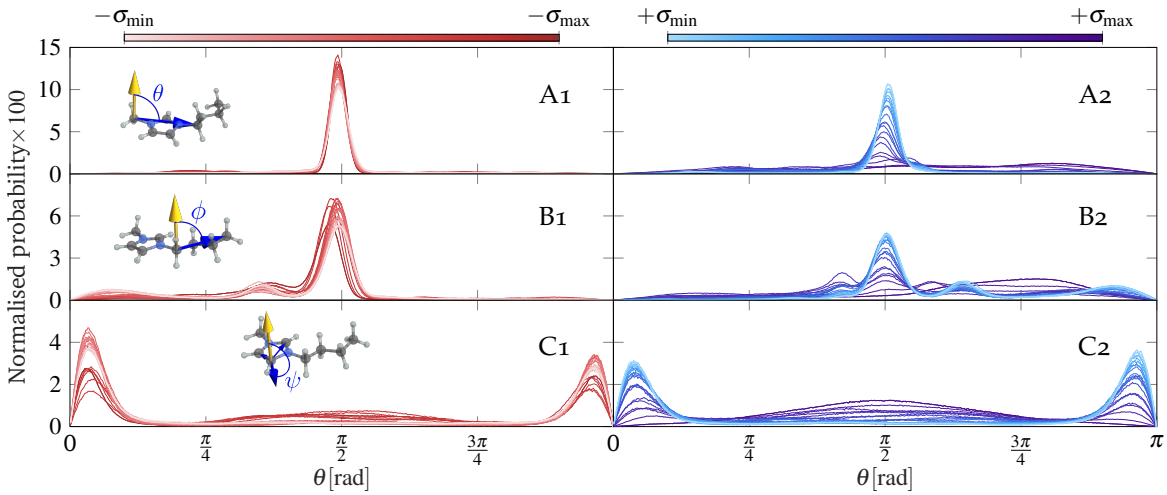

Figure 39: Orientation of cations within 5 Å from traditional gold surface. Panel labels A, B and C represent the distributions of the angles θ, ϕ and ψ respectively. The left panel (red lines) and the right panel (blue lines) correspond to the negatively and positively charged surfaces, respectively

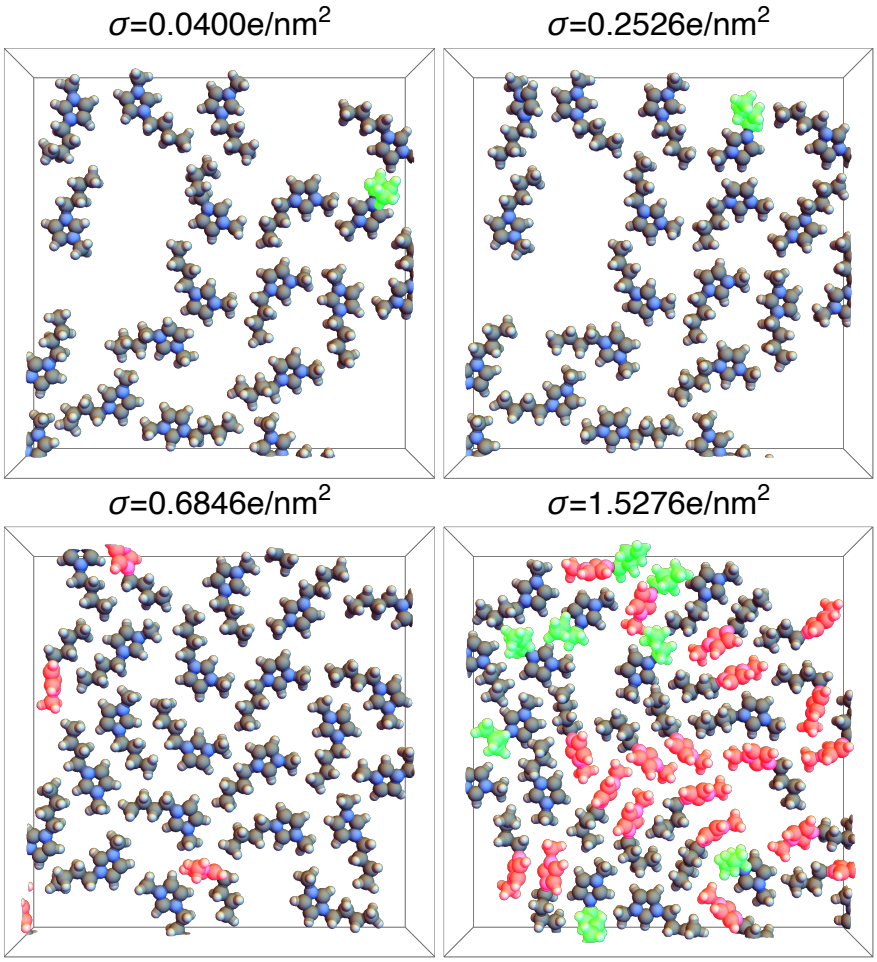

Figure 40: Orientation of cations at traditional gold cathode. Upon charging, we find adjustments to permit crowding similar for polarisable gold cathode shown in Figure 4 of this chapter's article on page 78.

- CHARGING MECHANISM: At the anode, the charging mechanism is dominated by the adsorption of BF_4^- anions, whereas at the cathode, co-ion desorption of BF_4^- is prevalent. This asymmetric behaviour underscores the distinct roles played by the ions in the charging process.
- DYNAMICAL PROPERTIES: Minor changes in the diffusion coefficients of ions were observed within the potential range considered. Notably, the bulk properties of the ionic liquid were restored at a shorter distance from the electrode surface at the anode compared to the cathode.

5.5 CONCLUSION

In conclusion, this chapter contributes significantly to the understanding of the differential capacitance and electric double layer structure at the gold electrode/[BMIM][BF_4] interface. By incorporating a polarisable model for the electrode, the study provides a more accurate representation of the EDL and highlights the importance of metal polarisation in enhancing the capacitance. The distinct charging mechanisms at the anode and cathode offer valuable insights into the ion interactions and adsorption phenomena at electrified interfaces. The implications of these findings are far-reaching for the field of electrochemistry and the development of energy storage devices. The enhanced understanding of the EDL structure and dynamics provided by the polarisable model can lead to better design and optimisation of supercapacitors and batteries.

THE JOURNAL OF PHYSICAL CHEMISTRY B
A JOURNAL OF THE AMERICAN CHEMICAL SOCIETY

pubs.acs.org/JPCB Article

Differential Capacitance of Ionic Liquid Confined between Metallic Interfaces

Samuel Ntim and Marialore Sulpizi*

Cite This: https://doi.org/10.1021/acs.jpcb.3c08042 Read Online

ACCESS | Metrics & More | Article Recommendations | Supporting Information

ABSTRACT: We present here a detailed analysis of the electric double layer at the gold electrode/[BMIM][BF_4] interface using a polarizable model for the electrode, based on our recent approach to include image charges [Geada et al. *Nat. Commun.* **2018**, *9*, 716]. A double bell (camel) shape is obtained for the differential capacitance, where the inclusion of metal polarization allows for a higher density of ions in the double layer, particularly around the maxima, thereby increasing the capacitance. The charging mechanism differs for the positive and negative electrodes, with counterion adsorption prevailing at the anode and co-ion desorption prevailing at the cathode. The charging mechanism is predominantly governed by the BF_4 anions, serving as counterions and co-ions at the anode and cathode, respectively. Within the considered range of potentials, only minor changes are observed in the dynamical properties, specifically in the diffusion coefficients. Notably, it is interesting to observe that bulk properties are restored at a shorter distance from the gold surface in the case of the anode compared to the cathode.

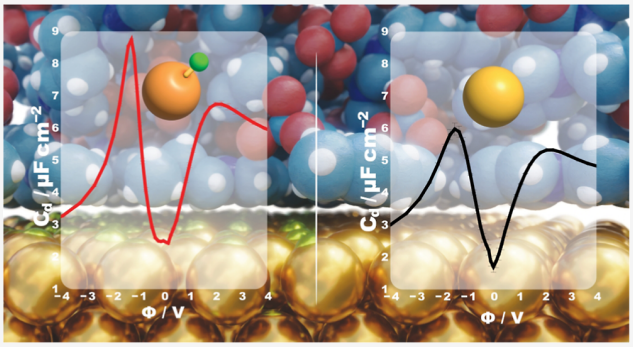

INTRODUCTION

The last two decades have seen a strong development of research in ionic liquids (IL) due to their application as the electrolyte in electrochemical capacitors, or supercapacitors.[1−4] A crucial step to advance such applications is the understanding of the structure of the electric double layer (EDL) at the electrolyte/electrode interface.[5,6] Experimentally, information on the EDL structure can be indirectly obtained by measuring the differential capacitance,[7] namely, the capacitance as a function of the applied voltage. A few features of the differential capacitance of ILs are well established, e.g., its asymmetry as consequence of the asymmetry in the constituent ions. Mean-field theory,[8−11] classical density functional theory,[12,13] as well as molecular dynamics (MD) simulations,[9,14−17] and experiments[18] have shown that the capacitance presents a higher value on the electrode containing the smaller ions. Another important aspect influencing the shape of the differential capacitance is the nonspherical shape of the ions, as well as the presence of charged heads and neutral tails. Both elements have been shown to be responsible for the camel-shape (or double-bell) of the capacitance as a function of the applied voltage. Indeed, in both cases, a nonspherical shape[16] as well as the possibility to replace neutral tails with charged groups via rotation and translation[15] provide extra degrees of freedom for the field-induced charge rearrangements in the double layer. The specific ion adsorption modifies the position of the potential of zero charge (PZC).

In the calculation of the differential capacitance two approaches are typically used, namely the constant charge,[19,20] where a constant charge is uniformly distributed on the electrodes, and the constant potential approaches,[21−26] where instead a constant potential is imposed on the electrode. In the fixed potential approach, the partial charges carried by the electrode atoms are treated as additional degrees of freedom, which can fluctuate during the simulation, and whose values are determined self-consistently for each electrolyte configuration. In the case of flat electrodes (surfaces), previous calculations on coarse-grained ILs confined between graphite electrodes[27] have shown that the two approaches provide similar, although not identical, results. Different is the situation of nanostructured electrodes, as e.g., carbon electrodes in supercapacitors where instead the presence of corrugated surfaces, channels, etc. can lead to strong charge localization and strong electric field heterogeneities.[28−30]

Recently we have introduced a simple model to include the metal polarization, which consists of a Lennard-Jones potential and a harmonically coupled core−shell charge pair for every

Received: December 8, 2023
Revised: February 7, 2024
Accepted: February 8, 2024

https://doi.org/10.1021/acs.jpcb.3c08042
J. Phys. Chem. B XXXX, XXX, XXX−XXX

metal atom. The model reproduces the classical image potential of adsorbed ions as well as surface, bulk, and aqueous interfacial properties in agreement with experiments.[31] We have also extended the model to describe variable potential conditions beyond the potential of zero-charge conditions. This is obtained by combining the polarizable model with additional charges on the electrode surface. Our approach has been used to investigate the Au(111) surface in contact with a NaCl electrolyte solution within a wide range of interfacial electrostatic potentials, where we found that the metal polarization enhances the interfacial capacitance influencing the ions distribution at the electrode/electrolyte interface.[32] In this contribution we apply our polarizable model for the metal in combination with additional fixed charges placed on surface atoms of the metal to simulate the ideal metallic behavior. We vary the potential via the surface charge density to calculate the differential capacitance for EDL at the Au(111) electrode/[BMIM][BF_4] interface. The motivation for such a choice is that, although such a system has been extensively investigated both on the experimental and on the computational point of view, some open questions still remain regarding the structure and dynamics of the EDL. When charging the electrode, the advantage of our model with respect to the traditional fixed charge model, is that it allows to include local polarization effects, as for example, those induced by the presence of local charge heterogeneity. Charges of opposite sign are evenly distributed on the surface of two electrodes, which confine the IL. During the MD simulation, for each configuration, every surface gold atom carries a net charge and an instantaneous dipole moment. A question may arise if the extra $\pm\Delta q$ charge should sit on the core (gold atom) or on the dummy. We have considered both possibilities, and we do not observe significant differences between them. In the current manuscript, we will always refer to the charge-on-core case, while the detailed comparison between the two cases can be found in the Supporting Information.

The paper is organized as follows: the structure of the double layer is investigated using atomistic simulations within our polarizable model for the metal surface[31] and the results compared to the fixed charge approach. In particular, the details of the differential capacitance are discussed for both cases. The charging mechanism, as well as the structural evolution, as a function of the interfacial electric potential, will also be presented. Along with structural properties, dynamical properties will also be discussed, particularly, the self-diffusion coefficient.

METHODOLOGY

Our model system contains 1200 pairs of [BMIM][BF_4], confined between two gold electrodes each made of 9 layers of gold atoms in the (111) crystallographic plane and spanning the 4.055 × 4.055 nm^2 cross-section of the box. Outside the electrodes, a vacuum region of 222 nm is added. Two-dimensional periodic boundary conditions are enforced along the x and y directions, while the interaction between images along the z-directions are decoupled using the Particle Mesh Ewald with slab correction.[33] To describe the atomistic IL, we use a nonpolarizable model of [BMIM][BF_4] with force field parameters that reproduce experimental heat of vaporization, diffusion coefficient, ionic conductivity, and shear viscosity of [BMIM][BF_4].[34] An extensive characterization of such a system at the PZC has been presented in our previous work.[35]

Two models for the gold were considered, a nonpolarizable gold model[36] and a polarizable one,[31] which includes the induced image charges. In order to obtain variable potentials for the electrodes, charges of opposite signs are evenly distributed on the two surfaces that confine the IL; $+\Delta q$ on the anode and $-\Delta q$ on the cathode, with the result of an overall neutral system. As a net result, for each configuration, every topmost-layer gold site carries a net charge and an instantaneous dipole moment. The net charge at each site of the topmost layer is obtained by an equal distribution of total surface charge that yields a desired surface charge density. We performed, for each gold model, 23 simulations at different charge densities. The charge densities are obtained from $\sigma = \sinh((0.05x)^2)e$ nm^{-2}; $x \in [1, 23]$ to give values ranging from 0.0025 to 1.7432 e nm^{-2} and to allow for a higher density of points near $\sigma = 0$ e nm^{-2}. Charge interactions in the gold are limited to those between different sites, excluding on-site interactions between bonded Au-core and Au-dummy.

To address the difference in the dynamical properties of our systems, we calculate the 2D diffusion coefficient in the plane of the gold surfaces within bins between gold surfaces. The calculation of the diffusion coefficient is performed with the same approach as in our previous work[35] such that given a bin, α, the 2D diffusion coefficient is calculated according to the Einstein relation

$$D_\alpha = \frac{1}{4}\lim_{\tau\to\infty}\frac{\mathrm{d}}{\mathrm{d}\tau}\mathrm{MSD}_\alpha(\tau) \tag{1}$$

where MSD_α is the mean squared displacement within the bin α, defined, for example along the x-axis and with a reference time t, as

$$\mathrm{MSD}_{x,\alpha}(t,\tau) = \frac{\sum_i \sigma_{i,\alpha}(t)\sigma_{i,\alpha}(t+\tau)(x_i(t+\tau)-x_i(t))^2}{\sum_i \sigma_{i,\alpha}(t)\sigma_{i,\alpha}(t+\tau)} \tag{2}$$

where $\sigma_{i,\alpha}(t)$ is a switching function for the ith particle in the bin α at time t, and $x_i(t)$ is the coordinate of that ith particle at time t. The switching function allows to account for particles entering and exiting a bin during the course of the simulation. Then by restarting the calculation of $\mathrm{MSD}_{x,\alpha}(t,\tau)$ at different reference times

$$\mathrm{MSD}_\alpha(\tau) = \frac{1}{N}\sum_{n=1}^{N}\sum_{j\in\{x,y\}}\mathrm{MSD}_{j,\alpha}(n\Delta t,\tau) \tag{3}$$

where Δt is a restart time, which is the time between two successive reference times, and N, is the number of restarts.

In order to ensure a statistically relevant sampling, five independent initial configurations were sampled from an equilibration run of 20 ns at a constant temperature of 298 K using a Nosé−Hoover thermostat, and at a constant pressure of 1 bar using a semi-isotropic Berendsen barostat. Therefore, for each value of the charge on the electrode, 5 independent realizations are considered.

All simulations were performed with version 5.1.4 of the GROMACS simulation package.[37]

RESULTS AND DISCUSSION

At the point of zero charge (PZC), when no net charge is present on the surface, an overscreening effect is observed, due to the size and shape difference between cations and anions. In particular, the cations adsorb closer to the gold surface than

https://doi.org/10.1021/acs.jpcb.3c08042
J. Phys. Chem. B XXXX, XXX, XXX−XXX

the anions, with the imidazole ring parallel to the gold surface. For the employed model (including the metal polarization) this leads to a PZC, $\Phi_0 = 0.26$ V. As discussed in our previous work,[35] the inclusion of the image charges for the metal does not have a big impact on Φ_0.

It is interesting to compare the differential capacitance, C_d, for the nonpolarizable and the polarizable gold models. C_d is defined as

$$C_d = \frac{\partial \sigma(\Phi)}{\partial \Phi} \tag{4}$$

where $\Phi = \Phi_{electrode} - \Phi_{bulk} - \Phi_0$, where $\Phi_{electrode}$ and Φ_{bulk} are electrostatic potentials at the surface of the electrode and in the liquid bulk, respectively. The electrode surface for polarizable gold was determined from the density profiles as the edge of the average sphere, centered on the topmost Au-core atoms, within which lies the topmost Au-dummies. In Figure 1, we

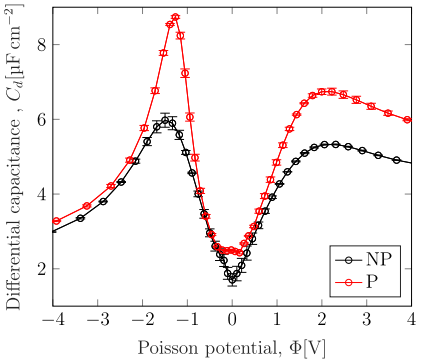

Figure 1. Differential capacitance for the atomistic simulations of the gold/[BMIM][BF_4] interface with the nonpolarizable gold model (black) and the polarizable gold model (red). According to the definition in eq 4, the potentials are referred to their corresponding values at PZC.

report the differential capacitance curves calculated for the polarizable (red) and nonpolarizable (black) models. Both curves present a minimum at 0 V (which, according to our definition, corresponds to the PZC) and increases for more positive or more negative values of the potential thus resulting into the double bell shape. Such a shape has been experimentally observed in imidazole-based n = 2, 4, 8 BF_4 ILs at the interface with platinum and polycrystalline gold electrodes,[9,18,38] as well as at glassy carbon.[39] Interestingly the values for C_d are very close to the experimental data. Only the potential range in our case appears to be stretched to larger values with respect to the experiments.[38] The double bell shape has also been predicted with models.[8,9,40−42]

The largest differences between the polarizable and nonpolarizable models are observed at moderate positive and negative potential values, in the area around the maxima. In particular, the polarizable model provides higher values for the capacitance, suggesting that for a given value of the electrode potential, the system is capable of storing more charge. In other words, the addition of the metal polarization permits to the system to store more charge in the double layer. It is also interesting to notice that at negative values of the potential there is an important difference in the capacitance between polarizable and nonpolarizable models around the maximum. For more negative values of the potential (below −2 V) however, the results of polarizable and nonpolarizable force fields agree. On the other hand, the situation is different for the positive potential branch. Indeed the difference between polarizable and nonpolarizable models, which develops around the maximum, also persists for more positive values of the potential (above 2 V).

The shape of the differential capacitance is not symmetric for positive and negative values of the potential. In particular, a higher capacitance is found for negative potentials. A similar behavior was also observed in the experiments[39] and simulations[43] of for [BMIM][PF_6] on graphite, where cations are the same as those investigated here and the electrode surface is flat, similarly to the (111) gold surface. The asymmetry between the two branches of the capacitance is related to the difference in the ions size and shapes and to the different mechanisms, which is observed for the double layer formation that we will discuss in detail here below.

When the electrode is charging, the charge can be balanced by two processes, namely the adsorption of counterions (ions with opposite charge with respect to that on the electrode) and the desorption of co-ions (ions with the same charge sign as that of the electrode). The competition between these two processes determines the local density at the interface in the process of charging. To describe the charging mechanism we use the same parameter X introduced by Merlet and co-workers in the case of the porous carbon electrodes,[44] with the difference that here we use it to characterize the first adsorbed layer on the electrode. The parameter X is defined as

$$X(\Phi, \Phi_0) = \frac{N(\Phi) - N(\Phi_0)}{(N_{counter}(\Phi) - N_{co}(\Phi) - (N_{counter}(\Phi_0) - N_{co}(\Phi_0))} \tag{5}$$

where $N(\Phi)$ is the total number of ions in the first adsorbed layer at a given charging potential Φ, $N(\Phi_0)$ is the total number of ions in the first adsorbed layer at PZC, Φ_0. $N_{counter}(\Phi)$ and $N_{co}(\Phi)$ are the number of counterions and co-ions, respectively, at the given potential Φ. The calculation of X parameters was performed in the region within 3.8 Å of the surface of the gold slabs. Such a cutoff was chosen to only include the first ions' layer at the interface, which is the one that is most affected by the polarization. X provides a measure of the relative balance between counterion adsorption and co-ion desorption in the charging mechanism. When the counterion adsorption prevails, X is positive, for ion exchange, X = 0, and finally, if the co-ion desorption prevails, X is negative. Such a definition also implies that X is confined to values between −1 and +1. In our case we find that at the anode (positive potential) X is close to +0.5, suggesting that counterion adsorption prevails during charging. On the other hand, at the cathode (negative potential), X is close to −0.5 suggesting that co-ions desorption prevails (Figure 2). It is worth noting that BF_4 (the anions) are the counterions and co-ions at the anode and the cathode, respectively, and therefore in the case of [BMIM][BF_4] the charging mechanism is largely driven by the anions.

Also, in Figure 2 we report how X varies as a function of absolute Poisson potential, |Φ| and we compare the results for the traditional (nonpolarizable) fixed charge approach and for our polarizable electrode. We find that the absolute values of X are smaller for the polarizable model (red lines), suggesting a larger weight of the ion exchange over the adsorption/desorption of ions in the case of the polarizable model. In

https://doi.org/10.1021/acs.jpcb.3c08042
J. Phys. Chem. B XXXX, XXX, XXX−XXX

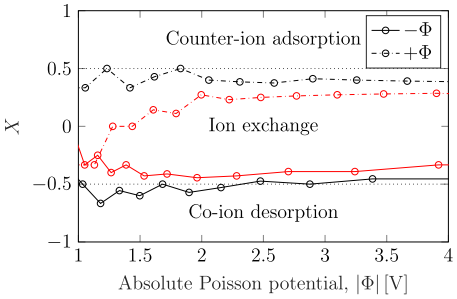

Figure 2. *X* parameter calculated within 3.8 Å from gold surface as a function of the interface potential. Black and red lines are for nonpolarizable and polarizable gold models, respectively, while solid and dashed lines are for negative and positive potentials (or surface charge densities). Horizontal dotted lines indicate boundaries separating the various charging mechanisms.

other words, especially around the maxima in the differential capacitance curves, ion exchange is enhanced in our polarizable gold. This well explains the enhancement seen in the differential capacitance curves since the ion exchange at the interface would result in higher ratios of counterions over co-ions stored at the interface (see Figure S7, showing how the ion ratios within 3.8 Å evolve with potential).

As the cations have a nonspherical symmetry, it is also interesting to investigate how their orientation changes as a function of the different charging states of the electrodes. In Figure 3 we show the distributions of the angles made by the relevant molecular axes on the cations and the normal to the electrodes surface, namely θ, the angle made by the axis across the imidazole ring, ϕ, the angle made by the axis along the butyl tail, and ψ, the angle made by the plane of the imidazole ring.

For the positive electrode, with increasing Φ the cations lose the mostly flat orientation which is observed at the PZC and are more disordered. This is shown, for example, by the angle distributions in Figure 3, where the peaks in panels A2, B2, and C2 are gradually lost as the potential increases.

As the cations move from the flat geometry on the surface, they leave space in exchange for the counterions, which indeed is suggested by the *X* parameter. On the other hand, on the negative electrode, the axis across the imidazole ring (panel A1 in Figure 3) remains parallel to the electrode surface. In addition to this, the stable peaks in panels B1 and C1 indicate a stable flat orientation for the cation (BMIM) especially at lower potentials. Similarly, sum frequency generation (SFG) spectra had suggested for [BMIM][DCA] that the imidazolium ring in the cation tends to lie flat at the surface of the electrode at negative potentials but is repelled at positive ones.[45] Flat-lying cations at the negative potential maximize the attractive interaction between the cations and the electrode, whereas, on the other hand, at the positive potential, cations tilt along the surface normal as they are repelled to maximize attractive interaction between anions and electrodes.[46] Similar reorientation of cations at the anode upon increasing electrode potential has also been shown by Motobayashi et al.[47] using surface-enhanced infrared absorption spectroscopy.

While the reorientation at the anode is very well established, it is interesting to note that there is also a reorientation of cations at the cathode upon increasing electrode potential. The stability of peaks in panels B1 and C1 of Figure 3 is not as maintained throughout the charging of surface as it is strongly maintained in panel A1. At the higher potentials, the tail orientation becomes randomized but within a range (panel B1). At the same time, the head shows, by the appearance of a plateau centered on $\pi/2$ (panel C1), a more upright configuration. At such high potentials, this picture of the cations mostly lying flat at the cathodic interface begins to change. With increasing Φ, the probability of an imidazolium cation having either a raised butyl tail or a tilted imidazole plane also increases (panel B1 and C1 in Figure 3). Kemna and Braunschweig[48] using in situ SFG experiments showed a more upright orientation of the imidazolium ring (of EMIM in their case) at a Pt/[EMIM][BF_4] interface (in the presence of 0.5 M H_2O) for both negative and positive potentials with respect to the PZC, for which the orientation was rather more flat. Ratschmeier and Braunschweig[49] further found that at very high negative potentials, the cation ([BMMIM]) showed a more upright orientation. This configuration allowed for creation of voids that were then occupied by water molecules present in their system. While comparing their results to previous studies under dry vacuum and in the absence of water, Ratschmeier and Braunschweig[49] showed that the presence of water could be an important determinant of the potential dependence of imidazolium orientation at an electrode interface. In our study, however, we find similar potential dependent orientation even in the absence of water. The molecular reorientation, in our case, also permits to increase in

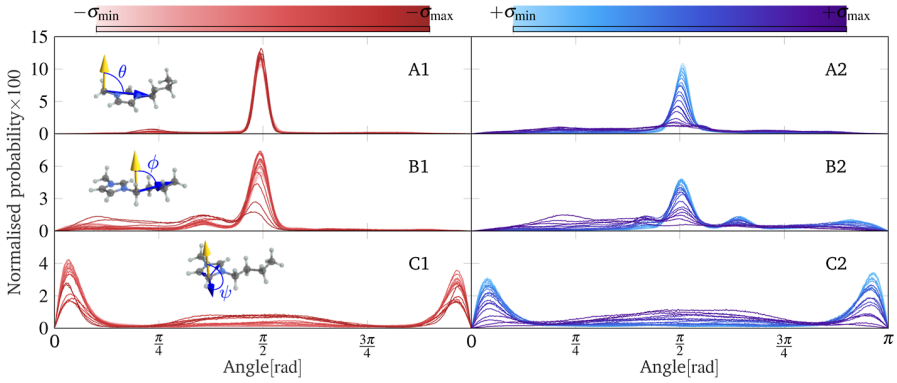

Figure 3. Orientation of the cations within 5 Å from polarizable gold surface. Panel labels (A−C) represent the distributions of the angles θ, ϕ, and ψ respectively. The left panel (red lines) and the right panel (blue lines) correspond to the negatively and positively charged surfaces, respectively.

https://doi.org/10.1021/acs.jpcb.3c08042
J. Phys. Chem. B XXXX, XXX, XXX−XXX

the density of the adsorbed cations on the surface as the applied negative potential increases.

In Figure 4 we present the changes in the molecular orientation in the first adsorbed layer on the cathode, at

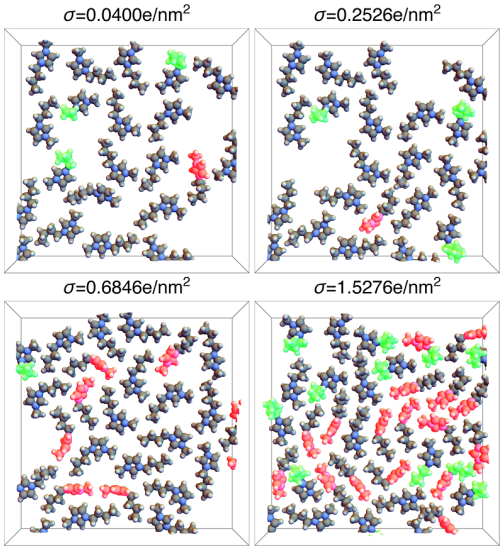

Figure 4. Orientation of cations at cathode. Upon charging, two main orientational adjustments to permit crowding are identified—raised tails, shown in green and perpendicularly tilted imidazole ring, shown in red.

different values of increasing surface charge (potential). In particular, the molecules whose butyl tails are colored in green show a change in the butyl tail orientation, which moves from laying on the surface to standing up ($\phi < \pi/4$) as the absolute electrode potential increases. The red-colored imidazolium rings indicates instead those molecules whose imidazole plane changes orientation from laying flat and parallel to the surface to standing orthogonal at the interface. Since the tail is neutral while the head/ring is charged, both types of change in the molecular orientation increase the ratio of imidazolium charge to the occupied interfacial area, allowing for a high counterion density in response to the very high negative potentials. It is well understood that the asymmetries in these ILs are the precursors for peculiar properties ILs exhibit. A direct consequence of the asymmetries in shape and size is the packing pattern that develops under certain conditions. The packing pattern that we find here is not only due to the asymmetries in shape but also to the flexibility of the ions. The consequences thereof throw a reasonable challenge to the modeling of ILs as charged spheres or rigid bodies especially at an interface, since this "softness" could not be captured in spherical and even nonspherical but highly coarse-grained rigid models.

Finally, we would like to briefly comment on the changes in the dynamical properties during the charging of the electrode. To this purpose, we have calculated the diffusion coefficient as a function of the distance from the gold surface. For each value of the charging potential, we calculate here the 2D translational self-diffusion in the plane of the gold surface within bins between the two gold surfaces, for the two ionic components. Figure 5 shows the diffusion coefficient across the interface for BMIM (blue tones) and for BF_4 (red tones). The values at the PZC are highlighted in black (dashed line for cations and solid

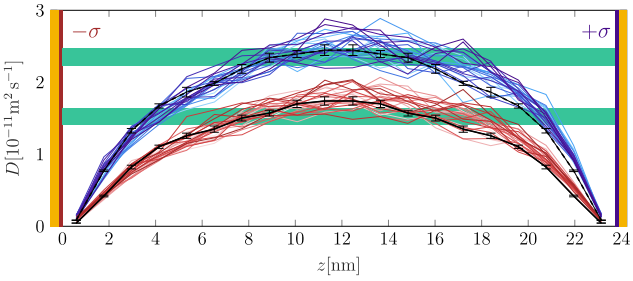

Figure 5. Diffusion coefficient of cations (in blue tones) and of anions (in red tones) across the interface. The black curves are for cations (dashed) and anions (solid) at PZC. Green strips are bulk diffusion coefficients of the ions with error bars.

line for the anions). The bulk diffusion coefficient of the ions, calculated from five independent trajectories of 800 ion pairs at 298 K and including the size correction[50] is also reported, including the statistical uncertainty as a green stripe. The cations diffuse much faster than the anions, with values monotonically increasing to the bulk value as we move away from the gold surface. We would like to stress that, as already pointed out in our previous work,[35] that although from the structural point of view, the EDL is only a couple of nm thick, from the dynamical point of view the perturbation to the diffusion coefficient persists on a much wider scale of the order of 10 nm. The main result here is that increasing the charge on the electrode does not significantly affect the diffusion coefficients, which remain very close to the values calculated and discussed at the PZC. Nonetheless, a slight asymmetry can be observed between the two interfaces (see Figure 5). In particular, at the cathode/liquid interface (negative potential side) the ions recover more slowly (at larger distances from the surface) the bulk behavior, while at the anode/liquid interface (positive potential side) recovery of bulk properties is faster (within shorter distance from the surface when compared to the cathode). The diffusion being significantly slower at the interface than in bulk is in direct agreement with works from several authors.[51−54] The asymmetry, however, may be an interplay of several factors. For example, there is already an asymmetry in the diffusion between cations and anions—cations being the more diffusive. Thus, as more cations are repelled at the anode (owing to ion ratios determined by the charging mechanism), the average diffusion near the anode tends to increase. However, we do not observe significant shift in the asymmetry for increasing potentials because the cations are also more resilient to repulsion at the interface for lower potentials as shown in their density profiles in Figure S6 and for higher potentials, the charging mechanism (X parameter) is fairly constant.

CONCLUSIONS

We have presented here a detailed analysis of the EDL at the gold electrode/[BMIM][BF_4] interface. In particular, we have investigated the shape of the differential capacitance comparing a polarizable model for the gold electrode, based on our recent work[31,32] and the standard fixed charge approach. The polarizable electrode provides higher values of the differential capacitance allowing to pack a higher density of ions in the double layer. Such a difference is particularly pronounced at the maxima of the double bell, and on the positive potential branch above 2 V. The charging mechanism is different for the positive and negative electrodes. In particular, at the anode

https://doi.org/10.1021/acs.jpcb.3c08042
J. Phys. Chem. B XXXX, XXX, XXX−XXX

(positive potential) counterion adsorption prevails during charging. On the other hand, at the cathode (negative potential), co-ions desorption prevails. In both cases, the charging mechanism is governed mostly by the BF_4 anions, which are the counterions, respectively co-ions at the anode and the cathode. We have also investigated the ions dynamics as a function of the applied potential and we have found that, within the considered range of potentials, there is no substantial change in the diffusion coefficients as a function of the distance from the interface, although it is interesting to notice that bulk properties are recovered at shorter distance from the gold surface in the case of the anode. As a future step, it will be interesting to test our polarizable model for the electrode on more complex geometries, to understand to what extent it is able to account for heterogeneity in the local electric fields.

■ ASSOCIATED CONTENT

Supporting Information

The Supporting Information is available free of charge at https://pubs.acs.org/doi/10.1021/acs.jpcb.3c08042.

Additional information on the gold model; comparison of differential capacitances for the charge on core versus charge on dummy gold setup; and counterpart figures for traditional gold model (PDF)

■ AUTHOR INFORMATION

Corresponding Author

Marialore Sulpizi − *Insitut für Physik, Ruhr Universität Bochum, Bochum 44801, Germany;* orcid.org/0000-0002-7810-3224; Email: Marialore.Sulpizi@rub.de

Author

Samuel Ntim − *Insitut für Physik, Johannes Gutenber Universität, Mainz 55128, Germany*

Complete contact information is available at: https://pubs.acs.org/10.1021/acs.jpcb.3c08042

Notes

The authors declare no competing financial interest.

■ ACKNOWLEDGMENTS

We are grateful to Benjamin Rotenberg and Mathieu Salanne for useful discussions. Parts of this research were conducted using the supercomputer Mogon and/or advisory services offered by Johannes Gutenberg University Mainz (hpc.uni-mainz.de). This project has received funding from the European Union's Horizon 2020 research and innovation program under grant agreement no 674979-NANOTRANS and from the Deutsche Forschungsgemeinschaft under the TRR146 project. This work was also funded by the Deutsche Forschungsgemeinschaft (DFG, German Research Foundation) under Germany's Excellence Strategy−EXC 2033-390677874−RESOLV.

■ REFERENCES

(1) Salanne, M. Ionic Liquids for Supercapacitor Applications. *Top. Curr. Chem.* **2017**, *375*, 63.

(2) Yu, L.; Chen, G. Z. Ionic Liquid-Based Electrolytes for Supercapacitor and Supercapattery. *Front. Chem.* **2019**, *7*, 272.

(3) Bacon, C.; Serva, A.; Merlet, C.; Simon, P.; Salanne, M. On the key role of electrolyte-electrode van der Waals interactions in the simulation of ionic liquids-based supercapacitors. *Electrochim. Acta* **2023**, *455*, 142380.

(4) Kim, H.-K.; Yu, A.; Titirici, M.; Merlet, C.; Gao, Y.; Wang, J. Materials challenges for supercapacitors. *APL Mater.* **2023**, *11*, 070401.

(5) Kondrat, S.; Feng, G.; Bresme, F.; Urbakh, M.; Kornyshev, A. A. Theory and Simulations of Ionic Liquids in Nanoconfinement. *Chem. Rev.* **2023**, *123*, 6668−6715.

(6) Zhang, C.; Cheng, J.; Chen, Y.; Chan, M. K. Y.; Cai, Q.; Carvalho, R. P.; Marchiori, C. F. N.; Brandell, D.; Araujo, C. M.; Chen, M.; et al. 2023 Roadmap on molecular modelling of electrochemical energy materials. *J. Phys.: Energy* **2023**, *5*, 041501.

(7) Su, Y.-Z.; Fu, Y.-C.; Wei, Y.-M.; Yan, J.-W.; Mao, B.-W. The Electrode/Ionic Liquid Interface: Electric Double Layer and Metal Electrodeposition. *ChemPhysChem* **2010**, *11*, 2764−2778.

(8) Kornyshev, A. A. Double-Layer in Ionic Liquids: Paradigm Change? *J. Phys. Chem. B* **2007**, *111*, 5545−5557.

(9) Vatamanu, J.; Borodin, O.; Smith, G. D. Molecular Insights into the Potential and Temperature Dependences of the Differential Capacitance of a Room-Temperature Ionic Liquid at Graphite Electrodes. *J. Am. Chem. Soc.* **2010**, *132*, 14825−14833.

(10) Fedorov, M. V.; Kornyshev, A. A. Ionic Liquids at Electrified Interfaces. *Chem. Rev.* **2014**, *114*, 2978−3036.

(11) de Souza, J. P.; Pivnic, K.; Bazant, M. Z.; Urbakh, M.; Kornyshev, A. A. Structural Forces in Ionic Liquids: The Role of Ionic Size Asymmetry. *J. Phys. Chem. B* **2022**, *126*, 1242−1253.

(12) Lauw, Y.; Horne, M. D.; Rodopoulos, T.; Nelson, A.; Leermakers, F. A. M. Electrical Double-Layer Capacitance in Room Temperature Ionic Liquids: Ion-Size and Specific Adsorption Effects. *J. Phys. Chem. B* **2010**, *114*, 11149−11154.

(13) Jiang, D.; Meng, D.; Wu, J. Density functional theory for differential capacitance of planar electric double layers in ionic liquids. *Chem. Phys. Lett.* **2011**, *504*, 153−158.

(14) Fedorov, M. V.; Kornyshev, A. A. Ionic Liquid Near a Charged Wall: Structure and Capacitance of Electrical Double Layer. *J. Phys. Chem. B* **2008**, *112*, 11868−11872.

(15) Fedorov, M. V.; Georgi, N.; Kornyshev, A. Double layer in ionic liquids: The nature of the camel shape of capacitance. *Electrochem. Commun.* **2010**, *12*, 296−299.

(16) Georgi, N.; Kornyshev, A.; Fedorov, M. The anatomy of the double layer and capacitance in ionic liquids with anisotropic ions: Electrostriction vs. lattice saturation. *J. Electroanal. Chem.* **2010**, *649*, 261−267 Special Issue Dedicated to Jacek Lipkowski.

(17) Katakura, S.; Nishi, N.; Kobayashi, K.; Amano, K.-i.; Sakka, T. Effect of Switching the Length of Alkyl Chains on Electric Double Layer Structure and Differential Capacitance at the Electrode Interface of Quaternary Ammonium-Based Ionic Liquids Studied Using Molecular Dynamics Simulation. *J. Phys. Chem. C* **2020**, *124*, 7873−7883.

(18) Alam, M. T.; Masud, J.; Islam, M. M.; Okajima, T.; Ohsaka, T. Differential Capacitance at Au(111) in 1-Alkyl-3-methylimidazolium Tetrafluoroborate Based Room-Temperature Ionic Liquids. *J. Phys. Chem. C* **2011**, *115*, 19797−19804.

(19) Feng, G.; Huang, J.; Sumpter, B. G.; Meunier, V.; Qiao, R. Structure and dynamics of electrical double layers in organic electrolytes. *Phys. Chem. Chem. Phys.* **2010**, *12*, 5468−5479.

(20) Feng, G.; Cummings, P. T. Supercapacitor Capacitance Exhibits Oscillatory Behavior as a Function of Nanopore Size. *J. Phys. Chem. Lett.* **2011**, *2*, 2859−2864.

(21) Siepmann, J. I.; Sprik, M. Influence of surface topology and electrostatic potential on water/electrode systems. *J. Chem. Phys.* **1995**, *102*, 511−524.

(22) Reed, S. K.; Lanning, O. J.; Madden, P. A. Electrochemical interface between an ionic liquid and a model metallic electrode. *J. Chem. Phys.* **2007**, *126*, 084704.

(23) Wang, Z.; Yang, Y.; Olmsted, D. L.; Asta, M.; Laird, B. B. Evaluation of the constant potential method in simulating electric double-layer capacitors. *J. Chem. Phys.* **2014**, *141*, 184102.

(24) Jeanmairet, G.; Rotenberg, B.; Salanne, M. Microscopic Simulations of Electrochemical Double-Layer Capacitors. *Chem. Rev.* **2022**, *122*, 10860−10898 PMID: 35389636.
(25) Scalfi, L.; Salanne, M.; Rotenberg, B. Molecular Simulation of Electrode-Solution Interfaces. *Annu. Rev. Phys. Chem.* **2021**, *72*, 189−212.
(26) Coretti, A.; Bacon, C.; Berthin, R.; Serva, A.; Scalfi, L.; Chubak, I.; Goloviznina, K.; Haefele, M.; Marin-Laflèche, A.; Rotenberg, B.; et al. MetalWalls: Simulating electrochemical interfaces between polarizable electrolytes and metallic electrodes. *J. Chem. Phys.* **2022**, *157*, 184801.
(27) Merlet, C.; Péan, C.; Rotenberg, B.; Madden, P. A.; Simon, P.; Salanne, M. Simulating Supercapacitors: Can We Model Electrodes As Constant Charge Surfaces? *J. Phys. Chem. Lett.* **2013**, *4*, 264−268.
(28) Merlet, C.; Rotenberg, B.; Madden, P. A.; Taberna, P.-L.; Simon, P.; Gogotsi, Y.; Salanne, M. On the molecular origin of supercapacitance in nanoporous carbon electrodes. *Nat. Mater.* **2012**, *11*, 306−310.
(29) Méndez-Morales, T.; Ganfoud, N.; Li, Z.; Haefele, M.; Rotenberg, B.; Salanne, M. Performance of microporous carbon electrodes for supercapacitors: Comparing graphene with disordered materials. *Energy Storage Mater.* **2019**, *17*, 88−92.
(30) Seebeck, J.; Merlet, C.; Meißner, R. H. Elucidating Curvature-Capacitance Relationships in Carbon-Based Supercapacitors. *Phys. Rev. Lett.* **2022**, *128*, 086001.
(31) Geada, I. L.; Ramezani-Dakhel, H.; Jamil, T.; Sulpizi, M.; Heinz, H. Insight into induced charges at metal surfaces and biointerfaces using a polarizable Lennard-Jones potential. *Nat. Commun.* **2018**, *9*, 716.
(32) Ntim, S.; Sulpizi, M. Molecular dynamics simulations of electrified interfaces including the metal polarisation. *Phys. Chem. Chem. Phys.* **2023**, *25*, 22619−22625 Publisher: The Royal Society of Chemistry.
(33) Yeh, I.-C.; Berkowitz, M. L. Ewald summation for systems with slab geometry. *J. Chem. Phys.* **1999**, *111*, 3155−3162.
(34) Chaban, V. V.; Voroshylova, I. V.; Kalugin, O. N. A new force field model for the simulation of transport properties of imidazolium-based ionic liquids. *Phys. Chem. Chem. Phys.* **2011**, *13*, 7910−7920.
(35) Ntim, S.; Sulpizi, M. Role of image charges in ionic liquid confined between metallic interfaces. *Phys. Chem. Chem. Phys.* **2020**, *22*, 10786−10791 Publisher: The Royal Society of Chemistry.
(36) Heinz, H.; Vaia, R.; Farmer, B.; Naik, R. Accurate simulation of surfaces and interfaces of face-centered cubic metals using 12-6 and 9-6 Lennard-Jones potentials. *J. Phys. Chem. C* **2008**, *112*, 17281−17290.
(37) Van Der Spoel, D.; Lindahl, E.; Hess, B.; Groenhof, G.; Mark, A. E.; Berendsen, H. J. C. GROMACS: Fast, flexible, and free. *J. Comput. Chem.* **2005**, *26*, 1701−1718.
(38) Oll, O.; Romann, T.; Siimenson, C.; Lust, E. Influence of chemical composition of electrode material on the differential capacitance characteristics of the ionic liquid| electrode interface. *Electrochem. Commun.* **2017**, *82*, 39−42.
(39) Zhang, Q.; Han, Y.; Wang, Y.; Ye, S.; Yan, T. Comparing the differential capacitance of two ionic liquid electrolytes: Effects of specific adsorption. *Electrochem. Commun.* **2014**, *38*, 44−46.
(40) Hu, Z.; Vatamanu, J.; Borodin, O.; Bedrov, D. A molecular dynamics simulation study of the electric double layer and capacitance of [BMIM] [PF6] and [BMIM] [BF4] room temperature ionic liquids near charged surfaces. *Phys. Chem. Chem. Phys.* **2013**, *15*, 14234−14247.
(41) Breitsprecher, K.; Košovan, P.; Holm, C. Coarse-grained simulations of an ionic liquid-based capacitor: I. Density, ion size, and valency effects. *J. Phys.: Condens. Matter* **2014**, *26*, 284108.
(42) Breitsprecher, K.; Košovan, P.; Holm, C. Coarse-grained simulations of an ionic liquid-based capacitor: II. Asymmetry in ion shape and charge localization. *J. Phys.: Condens. Matter* **2014**, *26*, 284114.
(43) Si, X.; Li, S.; Wang, Y.; Ye, S.; Yan, T. Effects of Specific Adsorption on the Differential Capacitance of Imidazolium-Based Ionic Liquid Electrolytes. *ChemPhysChem* **2012**, *13*, 1671−1676.
(44) Forse, A. C.; Merlet, C.; Griffin, J. M.; Grey, C. P. New Perspectives on the Charging Mechanisms of Supercapacitors. *J. Am. Chem. Soc.* **2016**, *138*, 5731−5744.
(45) Aliaga, C.; Baldelli, S. Sum Frequency Generation Spectroscopy and Double-Layer Capacitance Studies of the 1-Butyl-3-Methylimidazolium Dicyanamide-Platinum Interface. *J. Phys. Chem. B* **2006**, *110*, 18481−18491 PMID: 16970475.
(46) Baldelli, S. Surface Structure at the Ionic Liquid-Electrified Metal Interface. *Acc. Chem. Res.* **2008**, *41*, 421−431.
(47) Motobayashi, K.; Minami, K.; Nishi, N.; Sakka, T.; Osawa, M. Hysteresis of Potential-Dependent Changes in Ion Density and Structure of an Ionic Liquid on a Gold Electrode: In Situ Observation by Surface-Enhanced Infrared Absorption Spectroscopy. *J. Phys. Chem. Lett.* **2013**, *4*, 3110−3114 Publisher: American Chemical Society.
(48) Kemna, A.; Braunschweig, B. Potential-Induced Adsorption and Structuring of Water at the Pt(111) Electrode Surface in Contact with an Ionic Liquid. *J. Phys. Chem. Lett.* **2020**, *11*, 7116−7121 Publisher: American Chemical Society.
(49) Ratschmeier, B.; Braunschweig, B. Role of imidazolium cations on the interfacial structure of room-temperature ionic liquids in contact with Pt(111) electrodes. *Electrochem. Sci. Adv.* **2022**, *3*, No. e2100173.
(50) Yeh, I.-C.; Hummer, G. System-size dependence of diffusion coefficients and viscosities from molecular dynamics simulations with periodic boundary conditions. *J. Phys. Chem. B* **2004**, *108*, 15873−15879.
(51) Makino, S.; Kitazumi, Y.; Nishi, N.; Kakiuchi, T. Charging current probing of the slow relaxation of the ionic liquid double layer at the Pt electrode. *Electrochem. Commun.* **2011**, *13*, 1365−1368.
(52) Nishi, N.; Hirano, Y.; Motokawa, T.; Kakiuchi, T. Ultraslow relaxation of the structure at the ionic liquid|gold electrode interface to a potential step probed by electrochemical surface plasmon resonance measurements: asymmetry of the relaxation time to the potential-step direction. *Phys. Chem. Chem. Phys.* **2013**, *15*, 11615−11619 Publisher: The Royal Society of Chemistry.
(53) Sha, M.; Wu, G.; Dou, Q.; Tang, Z.; Fang, H. Double-Layer Formation of [Bmim] [PF6] Ionic Liquid Triggered by Surface Negative Charge. *Langmuir* **2010**, *26*, 12667−12672 Publisher: American Chemical Society.
(54) Dou, Q.; Sha, M.; Fu, H.; Wu, G. Mass Distribution and Diffusion of [1-Butyl-3-methylimidazolium] [Y] Ionic Liquids Adsorbed on the Graphite Surface at 300−800 K. *ChemPhysChem* **2010**, *11*, 2438−2443.

https://doi.org/10.1021/acs.jpcb.3c08042
J. Phys. Chem. B XXXX, XXX, XXX−XXX

6 CONCLUSIONS

This thesis provides a comprehensive, atomistic investigation into the behaviour of the Room-Temperature Ionic Liquid (RTIL), 1-butyl-3-methylimidazolium tetrafluoroborate ([BMIM][BF_4]), when confined between metallic interfaces under varying conditions: equilibrium, non-equilibrium shear flow, and electrified. The findings collectively advance the fundamental understanding required to optimise ILs for applications in energy storage, catalysis, and tribology.

SUMMARY OF KEY FINDINGS

Fundamental Interfacial Structure and the Role of Metallic Polarisation

Under equilibrium conditions at the PZC, the simulations confirmed the formation of a strong layered structure in the confined IL, extending approximately 2 nm from the Au(111) surface. Cations primarily adsorb with the imidazolium ring lying flat and parallel to the surface. This layering results in overscreening at the interface due to the asymmetry in ion size and shape, leading to a calculated PZC of 0.26 V for the polarisable gold model.

Contrary to initial hypotheses derived from certain experimental observations, the explicit inclusion of metal polarisation (image charges), modelled using a core–shell approach, was found to play a minor role in influencing the structural, thermodynamic (e.g., interfacial free energy or shift in freezing temperature), and dynamic properties of the [BMIM][BF_4] system at the PZC. This negligible effect is attributed to the strong electrostatic screening provided by the high concentration of counterions and the intrinsic dielectric response of the RTIL.

Despite the short range of the structural layering, the influence of the interface on the dynamical properties of the IL, specifically the translational self-diffusion coefficient, proved to be a long-range effect. Bulk diffusion coefficients were only recovered at approximately 10 nm away from the gold surface, suggesting an exponential dependence of viscosity as a function of distance from the confinement walls.

Non-Equilibrium Dynamics and Tribological Performance

The investigation into non-equilibrium conditions under applied shear flow demonstrated that the confined [BMIM][BF_4] system deviates significantly from ideal linear Couette flow. A key finding is the formation of a disordered, solid-like glassy layer close to the metallic surfaces, extending a few nanometres. The linear velocity regime is recovered only in the central region of the liquid slab. Crucially, analysis confirmed that the shear motion does not promote a crystalline structure; the interfacial layer maintains a glassy state, aligning with recent mechanical impedance measurements on nano-confined RTILs.

This solid-like layer, combined with strong surface adhesion, dictates the tribological behaviour. The lateral force showed a linear dependence on load across the studied range, fitted accurately by a modified Amontons' law. This suggests the RTIL remains in the same

frictional regime, resisting "squeeze out" at higher pressures. These characteristics confirm that the investigated RTIL can function as a good boundary lubricant.

Electrified Interfaces and Capacitance Mechanisms

A central contribution is the successful application and validation of a polarisable gold model—extended via the use of fixed additional charges—to investigate the electric double layer (EDL) structure under variable potential conditions. Methodological validation using a simpler NaCl electrolyte confirmed that the metal polarisation notably enhances interfacial capacitance, with a slightly larger impact observed at the cathode.

For the [BMIM][BF_4]/gold interface, the differential capacitance (C_d) curve exhibits the characteristic double bell (or camel) shape. The polarisable model yielded higher C_d values, particularly around the maxima, compared to the non-polarisable fixed-charge model, demonstrating that metal polarisation facilitates the packing of a higher density of ions in the double layer.

The charging mechanism is asymmetric and predominantly governed by the BF_4 anions. At the anode (positive potential), counterion adsorption prevails whereas at the cathode (negative potential), co-ion desorption prevails.

The polarisable model showed that ion exchange is enhanced around the capacitance maxima compared to pure adsorption/desorption processes. This asymmetry is accommodated by the non-spherical BMIM cations, which undergo molecular reorientation where they lose their flat orientation and become more disordered at the anode, while at the cathode, increasing negative potential promotes a more upright configuration (tilting the imidazole plane or raising the butyl tail) to maximise counterion density.

Finally, while increasing the electrode charge did not substantially affect the diffusion coefficients, a dynamic asymmetry was observed: bulk properties are recovered at shorter distance away from the anode compared to the cathode.

CONCLUDING REMARKS AND OUTLOOK

This thesis systematically characterised the complex molecular landscape of [BMIM][BF_4] at metallic interfaces. The research confirmed the importance of interfacial layering for structural properties and identified that the dynamic perturbation extends far into the bulk fluid. Furthermore, the work clarified that while image charges are minimally effective at the PZC due to screening, the inclusion of metal polarisation is essential for accurately calculating the differential capacitance and elucidating the asymmetric charging mechanisms required for supercapacitor design. The discovery of the robust, glassy interfacial layer under shear provides direct insights into the effective lubrication properties of RTIL.

Future work should focus on testing the validated polarisable model in more complex geometries to account for heterogeneity in local electric fields and incorporating out-of-equilibrium conditions (like charged tips or highly confined spaces) with metal polarisation effects to bridge the gap between simulation and complex nanorheological experiments. Further work is also required to understanding the underlying physics of the contrasting length scales of recovery of structural as opposed to dynamical bulk properties. Is there a dynamical EDL different from the structural EDL?

BIBLIOGRAPHY

[1] Guillaume Jeanmairet, Benjamin Rotenberg, and Mathieu Salanne. Microscopic simulations of electrochemical double-layer capacitors. *Chemical Reviews*, 122(12):10860–10898, 2022. doi: 10.1021/acs.chemrev.1c00925. URL https://doi.org/10.1021/acs.chemrev.1c00925. PMID: 35389636.

[2] Rafael Vicentini, Leonardo Morais Da Silva, Edson Pedro Cecilio Junior, Thayane Almeida Alves, Willian Gonçalves Nunes, and Hudson Zanin. How to measure and calculate equivalent series resistance of electric double-layer capacitors. *Molecules*, 24(8):1452, April 2019. ISSN 1420-3049. doi: 10.3390/molecules24081452. URL https://pmc.ncbi.nlm.nih.gov/articles/PMC6515551/.

[3] Robert F. Service. New 'supercapacitor' promises to pack more electrical punch. *Science*, 313(5789):902–902, August 2006. doi: 10.1126/science.313.5789.902. URL https://www.science.org/doi/full/10.1126/science.313.5789.902. Publisher: American Association for the Advancement of Science.

[4] B. E. Conway. *Electrochemical Supercapacitors*. Springer US, Boston, MA, 1999. ISBN 978-1-4757-3060-9 978-1-4757-3058-6. doi: 10.1007/978-1-4757-3058-6. URL http://link.springer.com/10.1007/978-1-4757-3058-6.

[5] H. Helmholtz. Ueber einige gesetze der vertheilung elektrischer ströme in körperlichen leitern mit anwendung auf die thierisch-elektrischen versuche. *Annalen der Physik*, 165(6):211–233, 1853. ISSN 1521-3889. doi: 10.1002/andp.18531650603. URL https://onlinelibrary.wiley.com/doi/abs/10.1002/andp.18531650603. _eprint: https://onlinelibrary.wiley.com/doi/pdf/10.1002/andp.18531650603.

[6] M. Gouy. Sur la constitution de la charge électrique à la surface d'un électrolyte. *Journal de Physique Théorique et Appliquée*, 9(1):457–468, 1910. ISSN 0368-3893. doi: 10.1051/jphystap:019100090045700. URL http://www.edpsciences.org/10.1051/jphystap:019100090045700.

[7] David Leonard Chapman. LI. *A contribution to the theory of electrocapillarity*. *The London, Edinburgh, and Dublin Philosophical Magazine and Journal of Science*, 25(148):475–481, April 1913. ISSN 1941-5982, 1941-5990. doi: 10.1080/14786440408634187. URL https://www.tandfonline.com/doi/full/10.1080/14786440408634187.

[8] S. Durand-Vidal, J.-P. Simonin, and P. Turq. *Electrolytes at Interfaces*. Number 1 in Progress in Theoretical Chemistry and Physics. Kluwer Academic Publishers, Dordrecht, 2002. ISBN 978-0-306-46940-4. doi: 10.1007/0-306-46940-5.

[9] John O'M Bockris, Amulya KN Reddy, and Maria Gamboa-Aldeco. Modern electrochemistry. 2a: Fundamentals of electrodics. In J. O'M Bockris, Amulya K. N. Reddy, and Maria Gamboa-Aldeco, editors, *Modern electrochemistry*. Plenum Pr, New York, NY, 2. ed edition, 2000. ISBN 978-0-306-46167-5. Num Pages: 771.

[10] David C. Grahame. The electrical double layer and the theory of electrocapillarity. *Chemical Reviews*, 41(3):441–501, December 1947. ISSN 0009-2665. doi:

10.1021/cr60130a002. URL https://doi.org/10.1021/cr60130a002. Publisher: American Chemical Society.

[11] Otto Stern. Zur Theorie der Elektrolytischen Doppelschicht. *Zeitschrift für Elektrochemie und angewandte physikalische Chemie*, 30(21):508–516, November 1924. ISSN 0372-8323. doi: 10.1002/bbpc.192400182. URL https://onlinelibrary.wiley.com/doi/10.1002/bbpc.192400182.

[12] M. A. V. Devanathan. A theory of the electrical double layer and the interpretation of differential capacity curves. *Transactions of the Faraday Society*, 50:373, 1954. ISSN 0014-7672. doi: 10.1039/tf9545000373. URL https://xlink.rsc.org/?DOI=tf9545000373.

[13] J. O'M. Bockris, M.A.V. Devanathan, and K. Müller. On the structure of charged interfaces. In *Electrochemistry*, pages 832–863. Elsevier, 1965. ISBN 978-1-4831-9831-6. doi: 10.1016/B978-1-4831-9831-6.50068-0. URL https://linkinghub.elsevier.com/retrieve/pii/B9781483198316500680.

[14] G. Valette. Double layer on silver single-crystal electrodes in contact with electrolytes having anions which present a slight specific adsorption. *Journal of Electroanalytical Chemistry and Interfacial Electrochemistry*, 122:285–297, May 1981. ISSN 00220728. doi: 10.1016/S0022-0728(81)80159-3. URL https://linkinghub.elsevier.com/retrieve/pii/S0022072881801593.

[15] J.J. Bikerman. XXXIX. structure and capacity of electrical double layer. *The London, Edinburgh, and Dublin Philosophical Magazine and Journal of Science*, 33(220):384–397, May 1942. ISSN 1941-5982. doi: 10.1080/14786444208520813. URL https://doi.org/10.1080/14786444208520813. Publisher: Taylor & Francis _eprint: https://doi.org/10.1080/14786444208520813.

[16] Norman F. Carnahan and Kenneth E. Starling. Equation of state for nonattracting rigid spheres. *The Journal of Chemical Physics*, 51(2):635–636, July 1969. ISSN 0021-9606, 1089-7690. doi: 10.1063/1.1672048. URL https://pubs.aip.org/jcp/article/51/2/635/456845/Equation-of-State-for-Nonattracting-Rigid-Spheres.

[17] Alexei A. Kornyshev. Double-layer in ionic liquids: paradigm change? *The Journal of Physical Chemistry B*, 111(20):5545–5557, may 2007. doi: 10.1021/jp0678570.

[18] J.J. López-García, J. Horno, and C. Grosse. Differential capacitance of the diffuse double layer at electrode-electrolyte interfaces considering ions as dielectric spheres: Part i. binary electrolyte solutions. *Journal of Colloid and Interface Science*, 496:531–539, June 2017. ISSN 00219797. doi: 10.1016/j.jcis.2017.02.043. URL https://linkinghub.elsevier.com/retrieve/pii/S0021979717302151.

[19] Martin Z. Bazant, Brian D. Storey, and Alexei A. Kornyshev. Double layer in ionic liquids: Overscreening versus crowding. *Physical Review Letters*, 106(4):046102, January 2011. doi: 10.1103/PhysRevLett.106.046102. URL https://link.aps.org/doi/10.1103/PhysRevLett.106.046102. Publisher: American Physical Society.

[20] Zachary A.H. Goodwin, Guang Feng, and Alexei A. Kornyshev. Mean-field theory of electrical double layer in ionic liquids with account of short-range correlations. *Electrochimica Acta*, 225:190–197, January 2017. ISSN 00134686. doi:

10.1016/j.electacta.2016.12.092. URL https://linkinghub.elsevier.com/retrieve/pii/S001346861632638X.

[21] M.V. Fedorov, N. Georgi, and A.A. Kornyshev. Double layer in ionic liquids: The nature of the camel shape of capacitance. *Electrochemistry Communications*, 12(2):296 – 299, 2010. ISSN 1388-2481. doi: https://doi.org/10.1016/j.elecom.2009.12.019. URL http://www.sciencedirect.com/science/article/pii/S1388248109006171.

[22] Manman Ma, Shuangliang Zhao, and Zhenli Xu. Investigation of dielectric decrement and correlation effects on electric double-layer capacitance by self-consistent field model. *Communications in Computational Physics*, 20(2):441–458, 2016.

[23] Martin Trulsson, Jenny Algotsson, Jan Forsman, and Clifford E. Woodward. Differential capacitance of room temperature ionic liquids: The role of dispersion forces. *The Journal of Physical Chemistry Letters*, 1(8):1191–1195, April 2010. doi: 10.1021/jz900412t. URL https://doi.org/10.1021/jz900412t. Publisher: American Chemical Society.

[24] Aleksey Khlyupin, Irina Nesterova, and Kirill Gerke. Molecular scale ion separation driven by surface roughness and ion size asymmetry: new analytical solutions for differential capacitance of EDL, 2022. URL https://arxiv.org/abs/2212.13566. Version Number: 2.

[25] Matthew A. Gebbie, Markus Valtiner, Xavier Banquy, Eric T. Fox, Wesley A. Henderson, and Jacob N. Israelachvili. Ionic liquids behave as dilute electrolyte solutions. *Proceedings of the National Academy of Sciences*, 110(24):9674–9679, 2013. ISSN 0027-8424. doi: 10.1073/pnas.1307871110. URL http://www.pnas.org/content/110/24/9674.

[26] Susan Perkin, Mathieu Salanne, Paul Madden, and Ruth Lynden-Bell. Is a stern and diffuse layer model appropriate to ionic liquids at surfaces? *Proceedings of the National Academy of Sciences*, 110(44):E4121–E4121, 2013. ISSN 0027-8424. doi: 10.1073/pnas.1314188110. URL https://www.pnas.org/content/110/44/E4121.

[27] Matthew A. Gebbie, Markus Valtiner, Xavier Banquy, Wesley A. Henderson, and Jacob N. Israelachvili. Reply to perkin et al.: Experimental observations demonstrate that ionic liquids form both bound (stern) and diffuse electric double layers. *Proceedings of the National Academy of Sciences*, 110(44):E4122–E4122, 2013. ISSN 0027-8424. doi: 10.1073/pnas.1315608110. URL https://www.pnas.org/content/110/44/E4122.

[28] Alexander M. Smith, Alpha A. Lee, and Susan Perkin. The electrostatic screening length in concentrated electrolytes increases with concentration. *The Journal of Physical Chemistry Letters*, 7(12):2157–2163, June 2016. doi: 10.1021/acs.jpclett.6b00867. URL https://doi.org/10.1021/acs.jpclett.6b00867. Publisher: American Chemical Society.

[29] Zahid Ali Zafar, Radim Weisser, Ghulam Abbas, Martin Silhavik, Prabhat Kumar, and Jiří Červenka. Aqueous supercapacitor with wide-temperature operability and over 100,000 cycles enabled by water-in-salt electrolyte. *ChemSusChem*, 18(6):e202401681, 2025. ISSN 1864-564X. doi: 10.1002/cssc.202401681. URL https://onlinelibrary.

wiley.com/doi/abs/10.1002/cssc.202401681. _eprint: https://chemistry-europe.onlinelibrary.wiley.com/doi/pdf/10.1002/cssc.202401681.

[30] Xining Zang, Caiwei Shen, Mohan Sanghadasa, and Liwei Lin. High-voltage supercapacitors based on aqueous electrolytes. *ChemElectroChem*, 6(4):976–988, 2019. ISSN 2196-0216. doi: 10.1002/celc.201801225. URL https://onlinelibrary.wiley.com/doi/abs/10.1002/celc.201801225. _eprint: https://chemistry-europe.onlinelibrary.wiley.com/doi/pdf/10.1002/celc.201801225.

[31] Xue Tian, Qizhen Zhu, and Bin Xu. "water-in-salt" electrolytes for supercapacitors: A review. *ChemSusChem*, 14(12):2501–2515, 2021. ISSN 1864-564X. doi: 10.1002/cssc.202100230. URL https://onlinelibrary.wiley.com/doi/abs/10.1002/cssc.202100230. _eprint: https://chemistry-europe.onlinelibrary.wiley.com/doi/pdf/10.1002/cssc.202100230.

[32] Shan Huang, Zhuo Li, Peng Li, Xianfeng Du, Mingbo Ma, Zhongshuai Liang, Yaqiong Su, and Lilong Xiong. Ultrahigh-voltage aqueous electrolyte for wide-temperature supercapacitors. *Journal of Materials Chemistry A*, 11(28):15532–15539, July 2023. ISSN 2050-7496. doi: 10.1039/D3TA01639K. URL https://pubs.rsc.org/en/content/articlelanding/2023/ta/d3ta01639k. Publisher: The Royal Society of Chemistry.

[33] Arpit Mendhe and H. S. Panda. A review on electrolytes for supercapacitor device. *Discover Materials*, 3(1):29, October 2023. ISSN 2730-7727. doi: 10.1007/s43939-023-00065-3. URL https://doi.org/10.1007/s43939-023-00065-3.

[34] Gowdhaman Arumugam, Balaji Chettiannan, Stanleydhinakar Mathan, Manickam Selvaraj, Mohammed A. Assiri, and Ramesh Rajendran. Better understanding of redox additives in aqueous electrolyte for electrochemical supercapacitors. *Journal of Energy Storage*, 121:116595, June 2025. ISSN 2352152X. doi: 10.1016/j.est.2025.116595. URL https://linkinghub.elsevier.com/retrieve/pii/S2352152X25013088.

[35] Lu Guan, Liangliang Guo, Haiyuan Yao, Jun Cai, Xuewei Dong, Ruonan Wang, Zhihua Zhai, Xuan Chen, Xiuzhi Wei, Dajin Li, Xingtong Liu, Shanshan Ji, and Fanxiao Meng. Redox additive electrolytes for supercapacitors: A mini-review on recent developments and future directions. *Molecules*, 30(8):1764, April 2025. ISSN 1420-3049. doi: 10.3390/molecules30081764. URL https://www.mdpi.com/1420-3049/30/8/1764.

[36] Abubakar Dahiru Shuaibu, Syed Shaheen Shah, Atif Saeed Alzahrani, and Md. Abdul Aziz. Advancing gel polymer electrolytes for next-generation high-performance solid-state supercapacitors: A comprehensive review. *Journal of Energy Storage*, 107:114851, January 2025. ISSN 2352152X. doi: 10.1016/j.est.2024.114851. URL https://linkinghub.elsevier.com/retrieve/pii/S2352152X24044372.

[37] Ghobad Behzadi Pour, Hamed Nazarpour Fard, and Leila Fekri Aval. A comparison of the electrical properties of gel polymer electrolyte-based supercapacitors: A review of advances in electrolyte materials. *Gels*, 10(12):803, December 2024. ISSN 2310-2861. doi: 10.3390/gels10120803. URL https://www.mdpi.com/2310-2861/10/12/803.

[38] Jiansen Ding, Yang Yang, Jade Poisson, Yuan He, Hua Zhang, Ying Zhang, Yulan Bao, Shuiliang Chen, Yong Mei Chen, and Kai Zhang. Recent advances in biopolymer-based hydrogel electrolytes for flexible supercapacitors. *ACS Energy Letters*, 9(4):1803–1825, April 2024. doi: 10.1021/acsenergylett.3c02567. URL https://doi.org/10.1021/acsenergylett.3c02567. Publisher: American Chemical Society.

[39] Weidong Liu, Zhiyun Li, Fang Pan, Qingyi He, and Qiushi Zhang. Solid polymer electrolytes reinforced with porous polypropylene separators for all-solid-state supercapacitors. *RSC Advances*, 13(49):34652–34659, 2023. doi: 10.1039/D3RA05899A. URL https://pubs.rsc.org/en/content/articlelanding/2023/ra/d3ra05899a. Publisher: Royal Society of Chemistry.

[40] Zheng Bo, Xu Zhang, Zhesong Huang, Yuhui Huang, Jianhua Yan, Kefa Cen, and Huachao Yang. Binary ionic liquids hybrid electrolyte based supercapacitors with high energy & power density. *RSC Advances*, 13(23):15762–15771, May 2023. ISSN 2046-2069. doi: 10.1039/D3RA01634J. URL https://pubs.rsc.org/en/content/articlelanding/2023/ra/d3ra01634j. Publisher: The Royal Society of Chemistry.

[41] Ahmed Bahaa, Ayoob Alhammadi, Kallidanthiyil Chellappan Lethesh, Rahmat Agung Susantyoko, and Musbaudeen O. Bamgbopa. Ionic liquid electrolyte selection for high voltage supercapacitors in high-temperature applications. *Frontiers in Chemistry*, 12:1349864, March 2024. ISSN 2296-2646. doi: 10.3389/fchem.2024.1349864. URL https://www.frontiersin.org/articles/10.3389/fchem.2024.1349864/full.

[42] Tribeni Roy, Saurav Goel, Luciano T. Costa, Maria-Magdalena Titirici, Gregory J. Offer, Monica Marinescu, and Huizhi Wang. Strain induced electrochemical behaviors of ionic liquid electrolytes in an electrochemical double layer capacitor: Insights from molecular dynamics simulations. *The Journal of Chemical Physics*, 159(24):244308, December 2023. ISSN 0021-9606. doi: 10.1063/5.0166976. URL https://doi.org/10.1063/5.0166976.

[43] Zairan Cheng, Yuto Ohnishi, Tsubasa Okamura, and Kiyoharu Nakagawa. High-energy-density electric double-layer capacitors (EDLCs) using tunable mesoporous carbon gel and ionic liquid electrolyte. *Journal of Materials Science*, 60(38):17757–17768, October 2025. ISSN 1573-4803. doi: 10.1007/s10853-025-11471-8. URL https://doi.org/10.1007/s10853-025-11471-8.

[44] Yan Wang, Kaiyuan Xue, Changzeng Yan, Yuehui Li, Xingyun Zhang, Kailimai Su, Pengjun Ma, Shanhong Wan, and Junwei Lang. Tuning of ionic liquid–solvent electrolytes for high-voltage electrochemical double layer capacitors: A review. *Batteries*, 10(2):54, February 2024. ISSN 2313-0105. doi: 10.3390/batteries10020054. URL https://www.mdpi.com/2313-0105/10/2/54.

[45] Thomas Welton. Room-temperature ionic liquids. solvents for synthesis and catalysis. *Chemical Reviews*, 99(8):2071–2084, August 1999. ISSN 0009-2665. doi: 10.1021/cr980032t. URL https://doi.org/10.1021/cr980032t. Publisher: American Chemical Society.

[46] Peter Wasserscheid, Thomas Welton, et al. *Ionic Liquids in Synthesis*. Wiley-VCH Verlag GmbH & Co. KGaA, 2002.

[47] Natalia V. Plechkova and Kenneth R. Seddon. Applications of ionic liquids in the chemical industry. *Chemical Society Reviews*, 37(1):123–150, December 2007. ISSN 1460-4744. doi: 10.1039/B006677J. URL https://pubs.rsc.org/en/content/articlelanding/2008/cs/b006677j. Publisher: The Royal Society of Chemistry.

[48] Jason P. Hallett and Tom Welton. Room-temperature ionic liquids: Solvents for synthesis and catalysis. 2. *Chemical Reviews*, 111(5):3508–3576, May 2011. ISSN 0009-2665. doi: 10.1021/cr1003248. URL https://doi.org/10.1021/cr1003248. Publisher: American Chemical Society.

[49] Maxim V. Fedorov and Alexei A. Kornyshev. Ionic liquids at electrified interfaces. *Chemical Reviews*, 114(5):2978–3036, 2014. doi: 10.1021/cr400374x. URL https://doi.org/10.1021/cr400374x. PMID: 24588221.

[50] John S. Wilkes. A short history of ionic liquids—from molten salts to neoteric solvents. *Green Chemistry*, 4(2):73–80, May 2002. ISSN 1463-9270. doi: 10.1039/B110838G. URL https://pubs.rsc.org/en/content/articlelanding/2002/gc/b110838g. Publisher: The Royal Society of Chemistry.

[51] John S. Wilkes, Joseph A. Levisky, Robert A. Wilson, and Charles L. Hussey. Dialkylimidazolium chloroaluminate melts: a new class of room-temperature ionic liquids for electrochemistry, spectroscopy and synthesis. *Inorganic Chemistry*, 21(3):1263–1264, March 1982. ISSN 0020-1669. doi: 10.1021/ic00133a078. URL https://doi.org/10.1021/ic00133a078. Publisher: American Chemical Society.

[52] Armand A. Jr. Fannin, Danilo A. Floreani, Lowell A. King, John S. Landers, Bernard J. Piersma, Daniel J. Stech, Robert L. Vaughn, John S. Wilkes, and John L. Williams. Properties of 1,3-dialkylimidazolium chloride-aluminum chloride ionic liquids. 2. phase transitions, densities, electrical conductivities, and viscosities. *The Journal of Physical Chemistry*, 88(12):2614–2621, June 1984. ISSN 0022-3654. doi: 10.1021/j150656a038. URL https://doi.org/10.1021/j150656a038. Publisher: American Chemical Society.

[53] C. L. Hussey, T. B. Scheffler, J. S. Wilkes, and A. A. Fannin. Chloroaluminate equilibria in the aluminum chloride-1-methyl-3-ethylimidazolium chloride ionic liquid. *Journal of The Electrochemical Society*, 133(7):1389, July 1986. ISSN 1945-7111. doi: 10.1149/1.2108893. URL https://iopscience.iop.org/article/10.1149/1.2108893/meta. Publisher: IOP Publishing.

[54] John S. Wilkes, James S. Frye, and G. Fredric Reynolds. Aluminum-27 and carbon-13 NMR studies of aluminum chloride-dialkylimidazolium chloride molten salts. *Inorganic Chemistry*, 22(26):3870–3872, December 1983. ISSN 0020-1669. doi: 10.1021/ic00168a011. URL https://doi.org/10.1021/ic00168a011. Publisher: American Chemical Society.

[55] Ingo Krossing, John M. Slattery, Corinne Daguenet, Paul J. Dyson, Alla Oleinikova, and Hermann Weingärtner. Why are ionic liquids liquid? a simple explanation based on lattice and solvation energies. *Journal of the American Chemical Society*, 128(41):13427–13434, October 2006. ISSN 0002-7863. doi: 10.1021/ja0619612. URL https://doi.org/10.1021/ja0619612. Publisher: American Chemical Society.

[56] H.-P. Steinrück, J. Libuda, P. Wasserscheid, T. Cremer, C. Kolbeck, M. Laurin, F. Maier, M. Sobota, P. S. Schulz, and M. Stark. Surface science and model catalysis with ionic liquid-modified materials. *Advanced Materials*, 23(22):2571–2587, June 2011. ISSN 0935-9648, 1521-4095. doi: 10.1002/adma.201100211. URL https://advanced.onlinelibrary.wiley.com/doi/10.1002/adma.201100211.

[57] Susan Perkin, Tim Albrecht, and Jacob Klein. Layering and shear properties of an ionic liquid, 1-ethyl-3-methylimidazolium ethylsulfate , confined to nano-films between mica surfaces. *Physical Chemistry Chemical Physics*, 12(6):1243–1247, 2010. doi: 10.1039/B920571C. URL https://pubs.rsc.org/en/content/articlelanding/2010/cp/b920571c.

[58] Susan Perkin. Ionic liquids in confined geometries. *Phys. Chem. Chem. Phys.*, 14: 5052–5062, 2012. doi: 10.1039/C2CP23814D. URL http://dx.doi.org/10.1039/C2CP23814D.

[59] Manuel Palacio and Bharat Bhushan. A review of ionic liquids for green molecular lubrication in nanotechnology. *Tribology Letters*, 40(2):247–268, November 2010. ISSN 1573-2711. doi: 10.1007/s11249-010-9671-8. URL https://doi.org/10.1007/s11249-010-9671-8.

[60] Maciej Galiński, Andrzej Lewandowski, and Izabela Stępniak. Ionic liquids as electrolytes. *Electrochimica Acta*, 51(26):5567–5580, August 2006. ISSN 00134686. doi: 10.1016/j.electacta.2006.03.016. URL https://linkinghub.elsevier.com/retrieve/pii/S0013468606002362.

[61] Rongying Lin, Pierre-Louis Taberna, Sébastien Fantini, Volker Presser, Carlos R. Pérez, François Malbosc, Nalin L. Rupesinghe, Kenneth B. K. Teo, Yury Gogotsi, and Patrice Simon. Capacitive energy storage from −50 °C to 100 °C using an ionic liquid electrolyte. *The Journal of Physical Chemistry Letters*, 2(19):2396–2401, October 2011. doi: 10.1021/jz201065t. URL https://doi.org/10.1021/jz201065t. Publisher: American Chemical Society.

[62] R. Palm, H. Kurig, K. Tõnurist, A. Jänes, and E. Lust. Is the mixture of 1-ethyl-3-methylimidazolium tetrafluoroborate and 1-butyl-3-methylimidazolium tetrafluoroborate applicable as electrolyte in electrical double layer capacitors? *Electrochemistry Communications*, 22:203–206, August 2012. ISSN 13882481. doi: 10.1016/j.elecom.2012.06.029. URL https://linkinghub.elsevier.com/retrieve/pii/S1388248112002810.

[63] Marina Mastragostino and Francesca Soavi. Strategies for high-performance supercapacitors for HEV. *Journal of Power Sources*, 174(1):89–93, November 2007. ISSN 03787753. doi: 10.1016/j.jpowsour.2007.06.009. URL https://linkinghub.elsevier.com/retrieve/pii/S0378775307012177.

[64] V. Borgel, E. Markevich, D. Aurbach, G. Semrau, and M. Schmidt. On the application of ionic liquids for rechargeable li batteries: High voltage systems. *Journal of Power Sources*, 189(1):331–336, April 2009. ISSN 03787753. doi: 10.1016/j.jpowsour.2008.08.099. URL https://linkinghub.elsevier.com/retrieve/pii/S0378775308017576.

[65] Eliana Quartarone and Piercarlo Mustarelli. Electrolytes for solid-state lithium rechargeable batteries: recent advances and perspectives. *Chemical Society Reviews*, 40

(5):2525–2540, April 2011. ISSN 1460-4744. doi: 10.1039/C0CS00081G. URL https://pubs.rsc.org/en/content/articlelanding/2011/cs/c0cs00081g. Publisher: The Royal Society of Chemistry.

[66] Jin Xiang, Feng Wu, Renjie Chen, Li Li, and Huigen Yu. High voltage and safe electrolytes based on ionic liquid and sulfone for lithium-ion batteries. *Journal of Power Sources*, 233:115–120, July 2013. ISSN 03787753. doi: 10.1016/j.jpowsour.2013.01.123. URL https://linkinghub.elsevier.com/retrieve/pii/S0378775313001808.

[67] Hikari Sakaebe, Hajime Matsumoto, and Kuniaki Tatsumi. Application of room temperature ionic liquids to li batteries. *Electrochimica Acta*, 53(3):1048–1054, December 2007. ISSN 00134686. doi: 10.1016/j.electacta.2007.02.054. URL https://linkinghub.elsevier.com/retrieve/pii/S001346860700299X.

[68] Peng Wang, Shaik M. Zakeeruddin, Jacques-E. Moser, and Michael Grätzel. A new ionic liquid electrolyte enhances the conversion efficiency of dye-sensitized solar cells. *The Journal of Physical Chemistry B*, 107(48):13280–13285, December 2003. ISSN 1520-6106. doi: 10.1021/jp0355399. URL https://doi.org/10.1021/jp0355399. Publisher: American Chemical Society.

[69] Bin Li, Liduo Wang, Bonan Kang, Peng Wang, and Yong Qiu. Review of recent progress in solid-state dye-sensitized solar cells. *Solar Energy Materials and Solar Cells*, 90(5):549–573, March 2006. ISSN 0927-0248. doi: 10.1016/j.solmat.2005.04.039. URL http://www.sciencedirect.com/science/article/pii/S0927024805001479.

[70] Erik Van De Ven, Anisa Chairuna, Géraldine Merle, Sergio Pacheco Benito, Zandrie Borneman, and Kitty Nijmeijer. Ionic liquid doped polybenzimidazole membranes for high temperature proton exchange membrane fuel cell applications. *Journal of Power Sources*, 222:202–209, January 2013. ISSN 03787753. doi: 10.1016/j.jpowsour.2012.07.112. URL https://linkinghub.elsevier.com/retrieve/pii/S0378775312012475.

[71] Martyn J. Earle, José M. S. S. Esperança, Manuela A. Gilea, José N. Canongia Lopes, Luís P. N. Rebelo, Joseph W. Magee, Kenneth R. Seddon, and Jason A. Widegren. The distillation and volatility of ionic liquids. *Nature*, 439(7078):831–834, February 2006. ISSN 1476-4687. doi: 10.1038/nature04451. URL https://www.nature.com/articles/nature04451. Publisher: Nature Publishing Group.

[72] James P. Armstrong, Christopher Hurst, Robert G. Jones, Peter Licence, Kevin R. J. Lovelock, Christopher J. Satterley, and Ignacio J. Villar-Garcia. Vapourisation of ionic liquids. *Physical Chemistry Chemical Physics*, 9(8):982–990, February 2007. ISSN 1463-9084. doi: 10.1039/B615137J. URL https://pubs.rsc.org/en/content/articlelanding/2007/cp/b615137j. Publisher: The Royal Society of Chemistry.

[73] Alasdair W. Taylor, Kevin R. J. Lovelock, Alexey Deyko, Peter Licence, and Robert G. Jones. High vacuum distillation of ionic liquids and separation of ionic liquid mixtures. *Physical Chemistry Chemical Physics*, 12(8):1772–1783, February 2010. ISSN 1463-9084. doi: 10.1039/B920931J. URL https://pubs.rsc.org/en/content/articlelanding/2010/cp/b920931j. Publisher: The Royal Society of Chemistry.

[74] Feng Zhou, Yongmin Liang, and Weimin Liu. Ionic liquid lubricants: designed chemistry for engineering applications. *Chemical Society Reviews*, 38(9):2590–2599,

August 2009. ISSN 1460-4744. doi: 10.1039/B817899M. URL https://pubs.rsc.org/en/content/articlelanding/2009/cs/b817899m. Publisher: The Royal Society of Chemistry.

[75] Oliver Werzer, Emily D. Cranston, Gregory G. Warr, Rob Atkin, and Mark W. Rutland. Ionic liquid nanotribology: mica–silica interactions in ethylammonium nitrate. *Physical Chemistry Chemical Physics*, 14(15):5147–5152, March 2012. ISSN 1463-9084. doi: 10.1039/C1CP23134K. URL https://pubs.rsc.org/en/content/articlelanding/2012/cp/c1cp23134k. Publisher: The Royal Society of Chemistry.

[76] Stefano Millefiorini, Alan H. Tkaczyk, Rossen Sedev, Jim Efthimiadis, and John Ralston. Electrowetting of ionic liquids. *Journal of the American Chemical Society*, 128(9):3098–3101, March 2006. ISSN 0002-7863. doi: 10.1021/ja057606d. URL https://doi.org/10.1021/ja057606d. Publisher: American Chemical Society.

[77] Yasith S. Nanayakkara, Hyejin Moon, Tharanga Payagala, Aruna B. Wijeratne, Jeffrey A. Crank, Pritesh S. Sharma, and Daniel W. Armstrong. A fundamental study on electrowetting by traditional and multifunctional ionic liquids: Possible use in electrowetting on dielectric-based microfluidic applications. *Analytical Chemistry*, 80(20):7690–7698, October 2008. ISSN 0003-2700. doi: 10.1021/ac8009802. URL https://doi.org/10.1021/ac8009802. Publisher: American Chemical Society.

[78] Frank Endres. Ionic liquids: Solvents for the electrodeposition of metals and semiconductors. *ChemPhysChem*, 3(2):144–154, February 2002. ISSN 1439-4235, 1439-7641. doi: 10.1002/1439-7641(20020215)3:2<144::AID-CPHC144>3.0.CO;2-#. URL https://onlinelibrary.wiley.com/doi/10.1002/1439-7641%2820020215%293%3A2%3C144%3A%3AAID-CPHC144%3E3.0.CO%3B2-%23.

[79] W. Freyland, C.A. Zell, S.Zein El Abedin, and F. Endres. Nanoscale electrodeposition of metals and semiconductors from ionic liquids. *Electrochimica Acta*, 48(20):3053–3061, September 2003. ISSN 00134686. doi: 10.1016/S0013-4686(03)00378-5. URL https://linkinghub.elsevier.com/retrieve/pii/S0013468603003785.

[80] Mingming Zhang, Venkat Kamavarum, and Ramana G. Reddy. New electrolytes for aluminum production: Ionic liquids. *JOM*, 55(11):54–57, November 2003. ISSN 1543-1851. doi: 10.1007/s11837-003-0211-y. URL https://doi.org/10.1007/s11837-003-0211-y.

[81] Jun-ichi Yoshida, Kazuhide Kataoka, Roberto Horcajada, and Aiichiro Nagaki. Modern strategies in electroorganic synthesis. *Chemical Reviews*, 108(7):2265–2299, July 2008. ISSN 0009-2665, 1520-6890. doi: 10.1021/cr0680843. URL https://pubs.acs.org/doi/10.1021/cr0680843.

[82] Philippe Hapiot and Corinne Lagrost. Electrochemical reactivity in room-temperature ionic liquids. *Chemical Reviews*, 108(7):2238–2264, July 2008. ISSN 0009-2665. doi: 10.1021/cr0680686. URL https://doi.org/10.1021/cr0680686. Publisher: American Chemical Society.

[83] Tim Albrecht, Kasper Moth-Poulsen, Jørn B. Christensen, Johan Hjelm, Thomas Bjørnholm, and Jens Ulstrup. Scanning tunneling spectroscopy in an ionic liquid. *Journal of the American Chemical Society*, 128(20):6574–6575, May 2006. ISSN 0002-7863. doi: 10.1021/ja061993p. URL https://doi.org/10.1021/ja061993p. Publisher: American Chemical Society.

[84] J. T. Ye, S. Inoue, K. Kobayashi, Y. Kasahara, H. T. Yuan, H. Shimotani, and Y. Iwasa. Liquid-gated interface superconductivity on an atomically flat film. *Nature Materials*, 9(2):125–128, February 2010. ISSN 1476-1122, 1476-4660. doi: 10.1038/nmat2587. URL https://www.nature.com/articles/nmat2587.

[85] Bryan D. Paulsen and C. Daniel Frisbie. Dependence of conductivity on charge density and electrochemical potential in polymer semiconductors gated with ionic liquids. *The Journal of Physical Chemistry C*, 116(4):3132–3141, February 2012. ISSN 1932-7447. doi: 10.1021/jp2093934. URL https://doi.org/10.1021/jp2093934. Publisher: American Chemical Society.

[86] S. Thiemann, S. Sachnov, S. Porscha, P. Wasserscheid, and J. Zaumseil. Ionic liquids for electrolyte-gating of ZnO field-effect transistors. *The Journal of Physical Chemistry C*, 116(25):13536–13544, June 2012. ISSN 1932-7447. doi: 10.1021/jp3024233. URL https://doi.org/10.1021/jp3024233. Publisher: American Chemical Society.

[87] Fang Chen, Quan Qing, Jilin Xia, Jinghong Li, and Nongjian Tao. Electrochemical gate-controlled charge transport in graphene in ionic liquid and aqueous solution. *Journal of the American Chemical Society*, 131(29):9908–9909, July 2009. ISSN 0002-7863. doi: 10.1021/ja9041862. URL https://doi.org/10.1021/ja9041862. Publisher: American Chemical Society.

[88] Abdul Rehman and Xiangqun Zeng. Ionic liquids as green solvents and electrolytes for robust chemical sensor development. *Accounts of Chemical Research*, 45(10):1667–1677, October 2012. ISSN 0001-4842. doi: 10.1021/ar200330v. URL https://doi.org/10.1021/ar200330v. Publisher: American Chemical Society.

[89] Debbie S. Silvester. Recent advances in the use of ionic liquids for electrochemical sensing. *Analyst*, 136(23):4871–4882, November 2011. ISSN 1364-5528. doi: 10.1039/C1AN15699C. URL https://pubs.rsc.org/en/content/articlelanding/2011/an/c1an15699c. Publisher: The Royal Society of Chemistry.

[90] Andrzej Lewandowski and Maciej Galinski. Practical and theoretical limits for electrochemical double-layer capacitors. *Journal of Power Sources*, 173(2):822–828, November 2007. ISSN 0378-7753. doi: 10.1016/j.jpowsour.2007.05.062. URL http://www.sciencedirect.com/science/article/pii/S037877530701066X.

[91] H. Kurig, M. Vestli, K. TÃµnurist, A. JÃ€nes, and E. Lust. Influence of Room Temperature Ionic Liquid Anion Chemical Composition and Electrical Charge Delocalization on the Supercapacitor Properties. *Journal of The Electrochemical Society*, 159 (7):A944–A951, January 2012. ISSN 0013-4651, 1945-7111. doi: 10.1149/2.022207jes. URL http://jes.ecsdl.org/content/159/7/A944.

[92] Mathieu Salanne. Ionic liquids for supercapacitor applications. *Topics in Current Chemistry*, 375(3):63, May 2017. ISSN 2364-8961. doi: 10.1007/s41061-017-0150-7. URL https://doi.org/10.1007/s41061-017-0150-7.

[93] Linpo Yu and George Z. Chen. Ionic liquid-based electrolytes for supercapacitor and supercapattery. *Frontiers in Chemistry*, 7:272, 2019. ISSN 2296-2646. doi: 10.3389/fchem.2019.00272. URL https://www.frontiersin.org/article/10.3389/fchem.2019.00272.

[94] Camille Bacon, Alessandra Serva, Céline Merlet, Patrice Simon, and Mathieu Salanne. On the key role of electrolyte-electrode van der waals interactions in the simulation of ionic liquids-based supercapacitors. *Electrochimica Acta*, 455:142380, 2023. ISSN 0013-4686. doi: https://doi.org/10.1016/j.electacta.2023.142380. URL https://www.sciencedirect.com/science/article/pii/S0013468623005583.

[95] Hyun-Kyung Kim, Aiping Yu, Magda Titirici, Céline Merlet, Yihua Gao, and John Wang. Materials challenges for supercapacitors. *APL Materials*, 11(7):070401, 07 2023. ISSN 2166-532X. doi: 10.1063/5.0162575. URL https://doi.org/10.1063/5.0162575.

[96] Daniela Molina Piper, Tyler Evans, Kevin Leung, Tylan Watkins, Jarred Olson, Seul Cham Kim, Sang Sub Han, Vinay Bhat, Kyu Hwan Oh, Daniel Buttry, and Se Hee Lee. Stable silicon-ionic liquid interface for next-generation lithium-ion batteries. *Nature Communications*, 6, 2 2015. ISSN 2041-1723. doi: 10.1038/ncomms7230.

[97] Douglas R. MacFarlane, Naoki Tachikawa, Maria Forsyth, Jennifer M. Pringle, Patrick C. Howlett, Gloria D. Elliott, James H. Davis, Masayoshi Watanabe, Patrice Simon, and C. Austen Angell. Energy applications of ionic liquids. *Energy & Environmental Science*, 7(1):232–250, December 2013. ISSN 1754-5706. doi: 10.1039/C3EE42099J. URL https://pubs.rsc.org/en/content/articlelanding/2014/ee/c3ee42099j.

[98] Jennifer L. Schaefer, Yingying Lu, Surya S. Moganty, Praveen Agarwal, N. Jayaprakash, and Lynden A. Archer. Electrolytes for high-energy lithium batteries. *Applied Nanoscience*, 2(2):91–109, June 2012. ISSN 2190-5517. doi: 10.1007/s13204-011-0044-x. URL https://doi.org/10.1007/s13204-011-0044-x.

[99] Masayoshi Watanabe, Morgan L. Thomas, Shiguo Zhang, Kazuhide Ueno, Tomohiro Yasuda, and Kaoru Dokko. Application of ionic liquids to energy storage and conversion materials and devices. *Chemical Reviews*, 117(10):7190–7239, 2017. doi: 10.1021/acs.chemrev.6b00504. URL https://doi.org/10.1021/acs.chemrev.6b00504. PMID: 28084733.

[100] Tsukasa Torimoto, Tetsuya Tsuda, Ken-ichi Okazaki, and Susumu Kuwabata. New Frontiers in Materials Science Opened by Ionic Liquids. *Advanced Materials*, 22(11):1196–1221, 2010. ISSN 1521-4095. doi: 10.1002/adma.200902184. URL https://onlinelibrary.wiley.com/doi/abs/10.1002/adma.200902184.

[101] Janno Torop, Mati Arulepp, Takushi Sugino, Kinji Asaka, Alar Jänes, Enn Lust, and Alvo Aabloo. Microporous and mesoporous carbide-derived carbons for strain modification of electromechanical actuators. *Langmuir*, 30(10):2583–2587, 2014.

[102] Meirong Cai, Qiangliang Yu, Weimin Liu, and Feng Zhou. Ionic liquid lubricants: when chemistry meets tribology. *Chem. Soc. Rev.*, pages –, 2020. doi: 10.1039/D0CS00126K. URL http://dx.doi.org/10.1039/D0CS00126K.

[103] Robert Hayes, Gregory G. Warr, and Rob Atkin. Structure and nanostructure in ionic liquids. *Chemical Reviews*, 115(13):6357–6426, 2015. doi: 10.1021/cr500411q. URL https://doi.org/10.1021/cr500411q. PMID: 26028184.

[104] Markus Mezger, Heiko Schröder, Harald Reichert, Sebastian Schramm, John S. Okasinski, Sebastian Schöder, Veijo Honkimäki, Moshe Deutsch, Benjamin M. Ocko, John Ralston, Michael Rohwerder, Martin Stratmann, and Helmut Dosch. Molecular layering of fluorinated ionic liquids at a charged sapphire (0001) surface. *Science*, 322(5900):424–428, 2008. ISSN 0036-8075. doi: 10.1126/science.1164502. URL https://science.sciencemag.org/content/322/5900/424.

[105] Robert Hayes, Gregory G. Warr, and Rob Atkin. At the interface: solvation and designing ionic liquids. *Phys. Chem. Chem. Phys.*, 12:1709–1723, 2010. doi: 10.1039/B920393A. URL http://dx.doi.org/10.1039/B920393A.

[106] Xiao Zhang, Yun-Xin Zhong, Jia-Wei Yan, Yu-Zhuan Su, Meng Zhang, and Bing-Wei Mao. Probing double layer structures of au (111)–bmipf6 ionic liquid interfaces from potential-dependent afm force curves. *Chem. Commun.*, 48:582–584, 2012. doi: 10.1039/C1CC15463J. URL http://dx.doi.org/10.1039/C1CC15463J.

[107] Bruno Zappone, Weichao Zheng, and Susan Perkin. Multiple-beam optical interferometry of anisotropic soft materials nanoconfined with the surface force apparatus. *REVIEW OF SCIENTIFIC INSTRUMENTS*, 89(8), AUG 2018. ISSN 0034-6748. doi: {10.1063/1.5038951}.

[108] Robert Hayes, Natalia Borisenko, Matthew K. Tam, Patrick C. Howlett, Frank Endres, and Rob Atkin. Double layer structure of ionic liquids at the au(111) electrode interface: An atomic force microscopy investigation. *The Journal of Physical Chemistry C*, 115(14):6855–6863, 2011. doi: 10.1021/jp200544b. URL https://doi.org/10.1021/jp200544b.

[109] Stefano Mossa. Re-entrant Phase Transitions and Dynamics of a Nanoconfined Ionic Liquid. *Physical Review X*, 8(3):031062, September 2018. ISSN 2160-3308. doi: 10.1103/PhysRevX.8.031062. URL https://link.aps.org/doi/10.1103/PhysRevX.8.031062.

[110] Jean Comtet, Antoine Niguès, Vojtech Kaiser, Benoit Coasne, Lydéric Bocquet, and Alessandro Siria. Nanoscale capillary freezing of ionic liquids confined between metallic interfaces and the role of electronic screening. *Nature Materials*, 16(6):634–639, mar 2017. doi: 10.1038/nmat4880.

[111] V. Kaiser, J. Comtet, A. Niguès, A. Siria, B. Coasne, and L. Bocquet. Electrostatic interactions between ions near thomas–fermi substrates and the surface energy of ionic crystals at imperfect metals. *Faraday Discuss.*, 199:129–158, 2017. doi: 10.1039/C6FD00256K. URL http://dx.doi.org/10.1039/C6FD00256K.

[112] Antoine Lainé, Antoine Niguès, Lydéric Bocquet, and Alessandro Siria. Nanotribology of Ionic Liquids: Transition to Yielding Response in Nanometric Confinement with Metallic Surfaces. *Physical Review X*, 10(1):011068, March 2020. ISSN 2160-3308. doi: 10.1103/PhysRevX.10.011068. URL https://link.aps.org/doi/10.1103/PhysRevX.10.011068.

[113] Chengfeng Ye, Weimin Liu, Yunxia Chen, and Laigui Yu. Room-temperature ionic liquids: a novel versatile lubricant. *Chem. Commun.*, pages 2244–2245, 2001. doi: 10.1039/B106935G. URL http://dx.doi.org/10.1039/B106935G.

[114] Weimin Liu, Chengfeng Ye, Qingye Gong, Haizhong Wang, and Peng Wang. Tribological performance of room-temperature ionic liquids as lubricant. *Tribology Letters*, 13:81–85, 2002. doi: https://doi.org/10.1023/A:1020148514878a.

[115] Qiming Lu, Haizhong Wang, Chengfeng Ye, Weimin Liu, and Qunji Xue. Room temperature ionic liquid 1-ethyl-3-hexylimidazolium-bis(trifluoromethylsulfonyl)-imide as lubricant for steel–steel contact. *Tribology International*, 37(7):547 – 552, 2004. ISSN 0301-679X. doi: https://doi.org/10.1016/j.triboint.2003.12.003. URL http://www.sciencedirect.com/science/article/pii/S0301679X03002330. The New Trends and Frontiers in Tribology.

[116] B. Phillips and J. Zabinski. Ionic liquid lubrication effects on ceramics in a water environment. *Tribology Letters*, 17:533–541, 2004. doi: https://doi.org/10.1023/B:TRIL.0000044501.64351.68.

[117] R. Gonzalez, A. Hernandez Battez, D. Blanco, J. Viesca, and A. Fernandez-Gonzalez. Lubrication of tin, crn and dlc pvd coatings with 1-butyl-1-methylpyrrolidinium tris(pentafluoroethyl)trifluorophosphate. *Tribology Letters*, 40:269–277, 2010.

[118] Romain Lhermerout and Susan Perkin. Nanoconfined ionic liquids: Disentangling electrostatic and viscous forces. *Phys. Rev. Fluids*, 3:014201, Jan 2018. doi: 10.1103/PhysRevFluids.3.014201. URL https://link.aps.org/doi/10.1103/PhysRevFluids.3.014201.

[119] Alexander M. Smith, Kevin R. J. Lovelock, Nitya Nand Gosvami, Tom Welton, and Susan Perkin. Quantized friction across ionic liquid thin films. *Physical Chemistry Chemical Physics*, 15(37):15317–15320, August 2013. ISSN 1463-9084. doi: 10.1039/C3CP52779D. URL https://pubs.rsc.org/en/content/articlelanding/2013/cp/c3cp52779d. Publisher: The Royal Society of Chemistry.

[120] Alexander M. Smith, Michael A. Parkes, and Susan Perkin. Molecular friction mechanisms across nanofilms of a bilayer-forming ionic liquid. *The Journal of Physical Chemistry Letters*, 5(22):4032–4037, 2014. doi: 10.1021/jz502188g. URL https://doi.org/10.1021/jz502188g. PMID: 26276489.

[121] Romain Lhermerout and Susan Perkin. A new methodology for a detailed investigation of quantized friction in ionic liquids. *Phys. Chem. Chem. Phys.*, 22:455–466, 2020. doi: 10.1039/C9CP05422G. URL http://dx.doi.org/10.1039/C9CP05422G.

[122] C Alba-Simionesco, Benoit Coasne, G Dosseh, G Dudziak, KE Gubbins, R Radhakrishnan, and MJPCM Sliwinska-Bartkowiak. Effects of confinement on freezing and melting. *Journal of Physics: Condensed Matter*, 18(6):R15, 2006.

[123] Svyatoslav Kondrat, Guang Feng, Fernando Bresme, Michael Urbakh, and Alexei A. Kornyshev. Theory and simulations of ionic liquids in nanoconfinement. *Chemical Reviews*, 123(10):6668–6715, 2023. doi: 10.1021/acs.chemrev.2c00728. URL https://doi.org/10.1021/acs.chemrev.2c00728. PMID: 37163447.

[124] Chao Zhang, Jun Cheng, Yiming Chen, Maria K Y Chan, Qiong Cai, Rodrigo P Carvalho, Cleber F N Marchiori, Daniel Brandell, C Moyses Araujo, Ming Chen, Xiangyu Ji, Guang Feng, Kateryna Goloviznina, Alessandra Serva, Mathieu Salanne, Toshihiko Mandai, Tomooki Hosaka, Mirna Alhanash, Patrik Johansson, Yun-Ze

Qiu, Hai Xiao, Michael Eikerling, Ryosuke Jinnouchi, Marko M Melander, Georg Kastlunger, Assil Bouzid, Alfredo Pasquarello, Seung-Jae Shin, Minho M Kim, Hyungjun Kim, Kathleen Schwarz, and Ravishankar Sundararaman. 2023 roadmap on molecular modelling of electrochemical energy materials. *Journal of Physics: Energy*, 5(4):041501, oct 2023. doi: 10.1088/2515-7655/acfe9b. URL https://dx.doi.org/10.1088/2515-7655/acfe9b.

[125] Yu-Zhuan Su, Yong-Chun Fu, Yi-Min Wei, Jia-Wei Yan, and Bing-Wei Mao. The electrode/ionic liquid interface: Electric double layer and metal electrodeposition. *ChemPhysChem*, 11(13):2764–2778, 2010. doi: 10.1002/cphc.201000278. URL https://onlinelibrary.wiley.com/doi/abs/10.1002/cphc.201000278.

[126] Roger Parsons. The electrical double layer: recent experimental and theoretical developments. *Chemical Reviews*, 90(5):813–826, July 1990. ISSN 0009-2665. doi: 10.1021/cr00103a008. URL https://doi.org/10.1021/cr00103a008. Publisher: American Chemical Society.

[127] Jenel Vatamanu, Oleg Borodin, and Grant D. Smith. Molecular insights into the potential and temperature dependences of the differential capacitance of a room-temperature ionic liquid at graphite electrodes. *Journal of the American Chemical Society*, 132(42):14825–14833, 2010. doi: 10.1021/ja104273r. URL https://doi.org/10.1021/ja104273r. PMID: 20925318.

[128] Y. Lauw, M. D. Horne, T. Rodopoulos, A. Nelson, and F. A. M. Leermakers. Electrical double-layer capacitance in room temperature ionic liquids: Ion-size and specific adsorption effects. *The Journal of Physical Chemistry B*, 114(34):11149–11154, 2010. doi: 10.1021/jp105317e. URL https://doi.org/10.1021/jp105317e. PMID: 20695502.

[129] De-en Jiang, Dong Meng, and Jianzhong Wu. Density functional theory for differential capacitance of planar electric double layers in ionic liquids. *Chemical Physics Letters*, 504(4):153 – 158, 2011. ISSN 0009-2614. doi: https://doi.org/10.1016/j.cplett.2011.01.072. URL http://www.sciencedirect.com/science/article/pii/S000926141100114X.

[130] Maxim V. Fedorov and Alexei A. Kornyshev. Ionic liquid near a charged wall: Structure and capacitance of electrical double layer. *The Journal of Physical Chemistry B*, 112(38):11868–11872, 2008. doi: 10.1021/jp803440q. URL https://doi.org/10.1021/jp803440q. PMID: 18729396.

[131] Seiji Katakura, Naoya Nishi, Kazuya Kobayashi, Ken-ichi Amano, and Tetsuo Sakka. Effect of switching the length of alkyl chains on electric double layer structure and differential capacitance at the electrode interface of quaternary ammonium-based ionic liquids studied using molecular dynamics simulation. *The Journal of Physical Chemistry C*, 124(14):7873–7883, 2020. doi: 10.1021/acs.jpcc.0c00795. URL https://doi.org/10.1021/acs.jpcc.0c00795.

[132] N. Georgi, A.A. Kornyshev, and M.V. Fedorov. The anatomy of the double layer and capacitance in ionic liquids with anisotropic ions: Electrostriction vs. lattice saturation. *Journal of Electroanalytical Chemistry*, 649(1):261 – 267, 2010. ISSN 1572-6657. doi: https://doi.org/10.1016/j.jelechem.2010.07.004. URL http://www.sciencedirect.com/science/article/pii/S1572665710003036. Special Issue Dedicated to Jacek Lipkowski.

[133] Konrad Breitsprecher, Peter Košovan, and Christian Holm. Coarse-grained simulations of an ionic liquid-based capacitor: I. Density, ion size, and valency effects. *Journal of Physics: Condensed Matter*, 26(28):284108, June 2014. ISSN 0953-8984. doi: 10.1088/0953-8984/26/28/284108. URL https://doi.org/10.1088%2F0953-8984%2F26%2F28%2F284108.

[134] Cesar Aliaga and Steven Baldelli. Sum frequency generation spectroscopy and double-layer capacitance studies of the 1-butyl-3-methylimidazolium dicyanamide-platinum interface. *The Journal of Physical Chemistry B*, 110(37):18481–18491, 2006. doi: 10.1021/jp063476z. URL https://doi.org/10.1021/jp063476z. PMID: 16970475.

[135] Steven Baldelli. Surface structure at the ionic liquid-electrified metal interface. *Accounts of Chemical Research*, 41(3):421–431, 2008. doi: 10.1021/ar700185h. URL https://doi.org/10.1021/ar700185h. PMID: 18232666.

[136] Kenta Motobayashi, Kazuya Minami, Naoya Nishi, Tetsuo Sakka, and Masatoshi Osawa. Hysteresis of Potential-Dependent Changes in Ion Density and Structure of an Ionic Liquid on a Gold Electrode: In Situ Observation by Surface-Enhanced Infrared Absorption Spectroscopy. *The Journal of Physical Chemistry Letters*, 4(18):3110–3114, September 2013. doi: 10.1021/jz401645c. URL https://doi.org/10.1021/jz401645c. Publisher: American Chemical Society.

[137] Björn Ratschmeier and Björn Braunschweig. Role of imidazolium cations on the interfacial structure of room-temperature ionic liquids in contact with pt(111) electrodes. *Electrochemical Science Advances*, page e2100173, 2022. doi: https://doi.org/10.1002/elsa.202100173. URL https://chemistry-europe.onlinelibrary.wiley.com/doi/abs/10.1002/elsa.202100173.

[138] O. Y. Fajardo, F. Bresme, A. A. Kornyshev, and M. Urbakh. Electrotunable lubricity with ionic liquid nanoscale films. *Scientific Reports*, 5(1):7698, 2015. ISSN 2045-2322. doi: 10.1038/srep07698. URL https://www.nature.com/articles/srep07698. Publisher: Nature Publishing Group.

[139] Karina Pivnic, Fernando Bresme, Alexei A. Kornyshev, and Michael Urbakh. Electrotunable friction in diluted room temperature ionic liquids: Implications for nanotribology. *ACS Applied Nano Materials*, 3(11):10708–10719, 2020. doi: 10.1021/acsanm.0c01946. URL https://doi.org/10.1021/acsanm.0c01946.

[140] Jacob N Israelachvili. Measurement of the viscosity of liquids in very thin films. *Journal of Colloid and Interface Science*, 110(1):263 – 271, 1986. ISSN 0021-9797. doi: https://doi.org/10.1016/0021-9797(86)90376-0. URL http://www.sciencedirect.com/science/article/pii/0021979786903760.

[141] Peter A. Thompson and Mark O. Robbins. Shear flow near solids: Epitaxial order and flow boundary conditions. *Phys. Rev. A*, 41:6830–6837, Jun 1990. doi: 10.1103/PhysRevA.41.6830. URL https://link.aps.org/doi/10.1103/PhysRevA.41.6830.

[142] D. M. Heyes, E. R. Smith, D. Dini, H. A. Spikes, and T. A. Zaki. Pressure dependence of confined liquid behavior subjected to boundary-driven shear. *The Journal of Chemical Physics*, 136(13):134705, April 2012. ISSN 0021-9606. doi: 10.1063/1.3698601. URL https://aip.scitation.org/doi/full/10.1063/1.3698601. Publisher: American Institute of Physics.

[143] Sz. Maćkowiak, D. M. Heyes, D. Dini, and A. C. Brańka. Non-equilibrium phase behavior and friction of confined molecular films under shear: A non-equilibrium molecular dynamics study. *The Journal of Chemical Physics*, 145(16):164704, 2016. doi: 10.1063/1.4965829. URL https://doi.org/10.1063/1.4965829.

[144] Alejandro Porras-Vazquez, Laetitia Martinie, Philippe Vergne, and Nicolas Fillot. Independence between friction and velocity distribution in fluids subjected to severe shearing and confinement. *Phys. Chem. Chem. Phys.*, 20:27280–27293, 2018. doi: 10.1039/C8CP04620D. URL http://dx.doi.org/10.1039/C8CP04620D.

[145] Anatolii V. Mokshin and Jean-Louis Barrat. Shear-induced crystallization of an amorphous system. *Phys. Rev. E*, 77:021505, Feb 2008. doi: 10.1103/PhysRevE.77.021505. URL https://link.aps.org/doi/10.1103/PhysRevE.77.021505.

[146] Zhen Shao, Jonathan P. Singer, Yanhui Liu, Ze Liu, Huiping Li, Manesh Gopinadhan, Corey S. O'Hern, Jan Schroers, and Chinedum O. Osuji. Shear-accelerated crystallization in a supercooled atomic liquid. *Phys. Rev. E*, 91:020301, Feb 2015. doi: 10.1103/PhysRevE.91.020301. URL https://link.aps.org/doi/10.1103/PhysRevE.91.020301.

[147] Vitaly V Chaban, Iuliia V Voroshylova, and Oleg N Kalugin. A new force field model for the simulation of transport properties of imidazolium-based ionic liquids. *Physical Chemistry Chemical Physics*, 13(17):7910–7920, 2011.

[148] In-Chul Yeh and Max L. Berkowitz. Ewald summation for systems with slab geometry. *The Journal of Chemical Physics*, 111(7):3155–3162, aug 1999. doi: 10.1063/1.479595.

[149] Isidro Lorenzo Geada, Hadi Ramezani-Dakhel, Tariq Jamil, Marialore Sulpizi, and Hendrik Heinz. Insight into induced charges at metal surfaces and biointerfaces using a polarizable Lennard-Jones potential. *Nature Communications*, 9(1):716, February 2018. ISSN 2041-1723. doi: 10.1038/s41467-018-03137-8. URL https://doi.org/10.1038/s41467-018-03137-8.

[150] Alpha A. Lee, Dominic Vella, Susan Perkin, and Alain Goriely. Are room-temperature ionic liquids dilute electrolytes? *The Journal of Physical Chemistry Letters*, 6(1):159–163, 2015. doi: 10.1021/jz502250z. URL https://doi.org/10.1021/jz502250z. PMID: 26263105.

[151] Matthew A. Gebbie, Howard A. Dobbs, Markus Valtiner, and Jacob N. Israelachvili. Long-range electrostatic screening in ionic liquids. *Proceedings of the National Academy of Sciences*, 112(24):7432–7437, 2015. ISSN 0027-8424. doi: 10.1073/pnas.1508366112. URL https://www.pnas.org/content/112/24/7432.

[152] N. Hjalmarsson, R. Atkin, and M. W. Rutland. Switchable long-range double layer force observed in a protic ionic liquid. *Chem. Commun.*, 53:647–650, 2017. doi: 10.1039/C6CC07396D. URL http://dx.doi.org/10.1039/C6CC07396D.

[153] Matthew A. Gebbie, Alexander M. Smith, Howard A. Dobbs, Alpha A. Lee, Gregory G. Warr, Xavier Banquy, Markus Valtiner, Mark W. Rutland, Jacob N. Israelachvili, Susan Perkin, and Rob Atkin. Long range electrostatic forces in ionic liquids. *Chem. Commun.*, 53:1214–1224, 2017. doi: 10.1039/C6CC08820A. URL http://dx.doi.org/10.1039/C6CC08820A.

[154] Alpha A. Lee, Carla S. Perez-Martinez, Alexander M. Smith, and Susan Perkin. Underscreening in concentrated electrolytes. *Faraday Discuss.*, 199:239–259, 2017. doi: 10.1039/C6FD00250A. URL http://dx.doi.org/10.1039/C6FD00250A.

[155] Guang Feng, Ming Chen, Sheng Bi, Zachary A. H. Goodwin, Eugene B. Postnikov, Michael Urbakh, and Alexei A. Kornyshev. Kinetics of Ion Transport in Ionic Liquids: Two Dynamical Diffusion States. *arXiv e-prints*, art. arXiv:1805.00697, May 2018.

[156] Frédéric Leroy and Florian Müller-Plathe. Dry-surface simulation method for the determination of the work of adhesion of solid–liquid interfaces. *Langmuir*, 31(30): 8335–8345, 2015.

[157] David Van Der Spoel, Erik Lindahl, Berk Hess, Gerrit Groenhof, Alan E. Mark, and Herman J. C. Berendsen. GROMACS: Fast, flexible, and free. *Journal of Computational Chemistry*, 26(16):1701–1718, 2005. doi: 10.1002/jcc.20291.

[158] Elisabete S. C. Ferreira, Carlos M. Pereira, M. Natália D. S. Cordeiro, and Daniel J. V. A. dos Santos. Molecular Dynamics Study of the Gold/Ionic Liquids Interface. *The Journal of Physical Chemistry B*, 119(30):9883–9892, jul 2015. doi: 10.1021/acs.jpcb.5b04505.

[159] Konrad Breitsprecher, Peter Košovan, and Christian Holm. Coarse-grained simulations of an ionic liquid-based capacitor: II. Asymmetry in ion shape and charge localization. *Journal of Physics: Condensed Matter*, 26(28):284114, June 2014. ISSN 0953-8984. doi: 10.1088/0953-8984/26/28/284114. URL https://doi.org/10.1088%2F0953-8984%2F26%2F28%2F284114.

[160] Alexandru Botan, Virginie Marry, and Benjamin Rotenberg. Diffusion in bulk liquids: finite-size effects in anisotropic systems. *Molecular Physics*, 113(17-18):2674–2679, September 2015. ISSN 0026-8976. doi: 10.1080/00268976.2015.1021730. URL https://doi.org/10.1080/00268976.2015.1021730.

[161] In-Chul Yeh and Gerhard Hummer. System-size dependence of diffusion coefficients and viscosities from molecular dynamics simulations with periodic boundary conditions. *The Journal of Physical Chemistry B*, 108(40):15873–15879, 2004.

[162] Sergey A. Kislenko, Igor S. Samoylov, and Ravil H. Amirov. Molecular dynamics simulation of the electrochemical interface between a graphite surface and the ionic liquid [BMIM][PF6]. *Physical Chemistry Chemical Physics*, 11(27):5584, 2009. doi: 10.1039/b823189c.

[163] Paul J. Steinhardt, David R. Nelson, and Marco Ronchetti. Bond-orientational order in liquids and glasses. *Physical Review B*, 28(2):784–805, July 1983. doi: 10.1103/PhysRevB.28.784. URL https://link.aps.org/doi/10.1103/PhysRevB.28.784. Publisher: American Physical Society.

[164] Liumin Suo, Yong-Sheng Hu, Hong Li, Michel Armand, and Liquan Chen. A new class of Solvent-in-Salt electrolyte for high-energy rechargeable metallic lithium batteries. *Nature Communications*, 4(1):1481, February 2013. ISSN 2041-1723. doi: 10.1038/ncomms2513. URL https://www.nature.com/articles/ncomms2513. Number: 1 Publisher: Nature Publishing Group.

[165] A. A. Kornyshev, N. B. Luque, and W. Schmickler. Differential capacitance of ionic liquid interface with graphite: the story of two double layers. *Journal of Solid State Electrochemistry*, 18(5):1345–1349, May 2014. ISSN 1433-0768. doi: 10.1007/s10008-013-2316-8. URL https://doi.org/10.1007/s10008-013-2316-8.

[166] Céline Merlet, Benjamin Rotenberg, Paul A. Madden, Pierre-Louis Taberna, Patrice Simon, Yury Gogotsi, and Mathieu Salanne. On the molecular origin of supercapacitance in nanoporous carbon electrodes. *Nature Materials*, 11(4):306–310, April 2012. ISSN 1476-4660. doi: 10.1038/nmat3260. URL https://www.nature.com/articles/nmat3260.

CURRICULUM VITÆ